TESIS DEFENDIDA POR

Olga Sarychikhina

Y APROBADA POR EL SIGUIENTE COMITÉ

Dra. Ewa Glowacka

Director del Comité

Dr. Robert J. Mellors

Miembro del Comité

Dr. Fidencio Alejandro Nava Pichardo

Miembro del Comité

Dr. Juan Contreras Pérez

Miembro del Comité

Dr. Rogelio Vázquez González

Miembro del Comité

Dr. Thomas Kretzschmar

Coordinador del programa de posgrado en Ciencias de la Tierra

Dr. David Hilario Covarrubias Rosales

Director de Estudios de Posgrado

07 de *abril* de 2010

CENTRO DE INVESTIGACIÓN CIENTÍFICA Y DE EDUCACIÓN SUPERIOR DE ENSENADA

PROGRAMA DE POSGRADO EN CIENCIAS EN CIENCIAS DE LA TIERRA

THE SPATIAL AND TEMPORAL DISTRIBUTION OF THE GROUND DEFORMATIONS IN THE MEXICALI VALLEY IN THE CONTEXT OF TECTONIC, ANTHROPOGENIC AND SEISMIC PROCESSES

DISTRIBUCIÓN ESPACIAL Y TEMPORAL DE DEFORMACIONES DEL TERRENO EN EL VALLE DE MEXICALI, EN EL CONTEXTO DE PROCESOS TECTÓNICOS, ANTROPOGÉNICOS Y SÍSMICO

TESIS

que para cubrir parcialmente los requisitos necesarios para obtener el grado de
DOCTOR EN CIENCIAS

Presenta:

OLGA SARYCHIKHINA

Ensenada, Baja California, México, Abril del 2010.

ABSTRACT of the thesis presented by **Olga Sarychikhina** as a partial requirement to obtain the DOCTOR OF SCIENCE degree in EARTH SCIENCES, with orientation in Seismology. Ensenada, Baja California, México. April 2010.

THE SPATIAL AND TEMPORAL DISTRIBUTION OF THE GROUND DEFORMATIONS IN THE MEXICALI VALLEY IN THE CONTEXT OF TECTONIC, ANTHROPOGENIC AND SEISMIC PROCESSES

Abstract approved by:

Dr. Ewa Glowacka
Supervisor

The Mexicali Valley, located in northeastern Baja California, is an example of an unstable region where ground deformation has become increasingly evident. The ground deformation in this area is caused by a variety of natural processes, such as earthquakes, continuous tectonic deformation, volcanic activity, but also by human activity, primarily geothermal exploitation. Since the type, spatial extent, and temporal pattern of the ground deformation largely depend on the type and magnitude of the driving process, the ground deformation measurements are essential to understand processes occurring below the surface.

In this thesis, the Differential Interferometric Synthetic Aperture Radar (DInSAR) technique was exploited to detect and measure variations of the ground surface in the Mexicali Valley. The DInSAR data were used to: (1) study anthropogenic surface deformation related to extraction of geothermal fluids in the Cerro Prieto Geothermal Field (CPGF), and (2) detect the tectonic surface deformation associated with the moderate magnitude (Mw=5.4) Morelia Fault Earthquake which occurred in the Mexicali Valley on May 24, 2006. In both cases the integrated analysis of DInSAR data and data from ground based geological, geodetic, and geotechnical measurements was also performed in order to improve the understanding of temporal and spatial distributions of ground deformation and modeling of its source mechanisms.

Firstly, 22 Envisat ASAR images from descending and ascending tracks, spanning October 2003 and February 2006 were used to evaluate the feasibility and capability of using conventional two-pass DInSAR for monitoring the induced by geothermal fluids extraction subsidence. The analysis of DInSAR data showed that, despite several limitations associated with the application of this method, the C-Band radar data can provide a detailed mapping of both the amplitude and spatial extent of anthropogenic ground deformation in Mexicali Valley. The processed data revealed that the studied area is continuously subsiding. The observed by DInSAR ground subsidence shows a northeast-southwest aligned elliptical pattern, largely coincident with the known shape of the Cerro Prieto pull-apart basin as it was noticed in Glowacka *et al.* (1999, 2005). The highest deformation rate area has two subsidence basins: a first centre of subsidence is located in the CPGF production zone, and the second is located in the area between the eastern limits of the

CPGF and the Saltillo fault, which was proposed as recharge zone in previous studies (Glowacka *et al*., 1999; Sarychikhina, 2003). The integration of the observed by DInSAR subsidence pattern with mapped geological data allowed to identify the tectonic faults which control the spatial extent of the observed subsidence. Based on the differential interferograms stacking technique, an annual deformation rate-map was generated for the period December 2004 – December 2005. DInSAR stacking data are well explained by model which consists of 7 rectangular tensional fractures: 4 corresponding to two geothermal reservoirs and 3 representing two recharge aquifers. The comparison of DInSAR stacking data with leveling data from 1994-1997 and 1997-2006 surveys reveals the increase of subsidence rate in the recharge zone and migration to the northeast of maximum deformation in the CPGF production zone. The variable deformation pattern and subsidence rate can be linked with the changes in the geothermal fluid extraction.

Secondly, 11 Envisat ASAR images, from descending and ascending tracks, spanning December 2005 and December 2006, were used for the study of coseismic deformation caused by moderate size (Mw=5.4) Morelia Fault Earthquake. Despite the decorrelation, a clear deformation signal roughly parallel to the known surface fault and consistent with normal faulting was observed in the wrapped phase image. Beside satellite coseismic observations, clear deformation signals caused by the May 24, 2006 earthquake were detected by leveling surveys, field observations and geotechnical instruments (crackmeters, tiltmeters and piezometers). Source parameters for the earthquake were estimated using forward modeling of both surface deformation data and static volume strain changes inferred from co-seismic changes in groundwater level. The modeling results confirm the shallow depth of the earthquake and explain in part why the earthquake was so strongly felt in the area. The value of static volumetric strain efficiency was obtained and could be used in the future studies of groundwater level changes due to crustal deformation in the study area not only caused by seismic events but also by aseismic creep or anthropogenic activity. Based on results of the theoretical postseismic fluid-flow modeling the hydraulic diffusivity was estimated. The range of estimated values is in good agreement with values obtained in the other studies for the same area (Glowacka and Nava, 1996; Glowacka *et al.*, 2010), and is within diffusivity range for seismogenic faults specified by Talwani and Acree (1984/1985).

Keywords: Differential Interferometric Synthetic Aperture Radar, ground deformation, anthropogenic, tectonic, coseismic, Mexicali Valley, Cerro Prieto Geothermal Field, Morelia Fault Earthquake.

RESUMEN de la tesis de **Olga Sarychikhina,** presentada como requisito parcial para la obtención del grado de DOCTOR EN CIENCIAS en Ciencias de la Tierra con orientación en Sismología. Ensenada, Baja California. Abril 2010.

DISTRIBUCIÓN ESPACIAL Y TEMPORAL DE DEFORMACIONES DEL TERRENO EN EL VALLE DE MEXICALI, EN EL CONTEXTO DE PROCESOS TECTÓNICOS, ANTROPOGÉNICOS Y SÍSMICO

Resumen aprobado por:

Dra. Ewa Glowacka
Director de Tesis

El Valle de Mexicali, que se localiza en noreste de Baja California, es un ejemplo de una región inestable donde la deformación del terreno se ha puesto cada vez más evidentes. La deformación del terreno en esta área es causada por una variedad de procesos naturales, tales como sismos, deformación tectónica continua, actividad volcánica, pero también por actividad humana, sobre todo explotación geotérmica. Debido a que el tipo, la extensión espacial, y el patrón temporal de la deformación del terreno dependen en gran parte del tipo y la magnitud del proceso que conduce a esta, las mediciones de la deformación del terreno son esenciales para entender los procesos que ocurren debajo de la superficie terrestre.

En esta tesis, la técnica de la Interferometría Diferencial de imágenes de Radar de Apertura Sintética (DInSAR) fue explotada para detectar y medir variaciones de la superficie del terreno en el Valle de Mexicali. Los datos de DInSAR fueron utilizados para: (1) estudiar la deformación antropogénica de la superficie del terreno relacionada con la extracción de fluidos geotérmicos en el campo geotérmico de Cerro Prieto (CPGF), y (2) detectar la deformación de la superficie terrestre tectónica asociada al sismo de la Falla Morelia de magnitud moderada (Mw=5.4) que ocurrió en el Valle de Mexicali el 24 de mayo de 2006. En ambos casos, el análisis integrado de los datos de DInSAR y los datos de mediciones geológicas, geodésicas, y geotécnicas también fue realizado para mejorar la comprensión de distribuciones temporales y espaciales de la deformación del terreno y el modelado de sus mecanismos.

Primeramente, 22 imágenes de Envisat ASAR de los pasos descendentes y ascendentes, que cubren el periodo de octubre de 2003 a febrero de 2006, fueron utilizadas para evaluar la viabilidad y la capacidad de la técnica convencional de dos-pasos de DInSAR para el monitoreo de la deformación del terreno inducida por la extracción de fluidos geotérmicos. El análisis de los datos de DInSAR demostró que, a pesar de varias limitaciones asociadas al uso de este método, los datos del radar de banda-C pueden proporcionar un mapeo detallado de la amplitud y de la extensión espacial de la deformación del terreno antropogénica en el Valle de Mexicali. Los datos procesados revelaron que el área de estudio se está hundiendo continuamente. La subsidencia del terreno observada por DInSAR muestra un patrón elíptico alineado noreste-sudoeste, en gran parte coincidente

con la forma conocida de la cuenca de extensión de Cerro Prieto, como fue notado en Glowacka *et al.* (1999, 2005). El área con alta tasa de deformación tiene dos centros del hundimiento: el primer centro del hundimiento está localizado en la zona de la producción del CPGF, y el segundo está localizado en el área entre el límite este del CPGF y la falla Saltillo, que fue propuesta como zona de recarga en los estudios anteriores (Glowacka *et al.*, 1999; Sarychikhina, 2003).

La integración del patrón de subsidencia observado por DInSAR con datos de mapeo geológico permitió identificar las fallas tectónicas que controlan la extensión espacial de la subsidencia observada. Basando en la técnica de apilamiento de interferogramas diferenciales, un mapa de la tasa de deformación anual fue generado para el período del diciembre de 2004 a diciembre de 2005. Los datos de apilamiento de DInSAR son bien explicados por el modelo que consiste de 7 fracturas tensionales rectangulares: 4 de ellas corresponden a dos reservorios geotérmicos y 3 representan dos acuíferos de la recarga. La comparación de los datos de apilamiento de DInSAR con los datos de nivelación de 1994-1997 y 1997-2006 revela el aumento de la tasa de subsidencia en la zona de la recarga y la migración al noreste de la deformación máxima en la zona de la producción de CPGF. Los cambios en el patrón de deformación y la tasa de subsidencia pueden ser vinculados con los cambios en la extracción de fluidos geotérmicos.

En segundo lugar, 11 imágenes de Envisat ASAR, de los pasos descendentes y ascendentes, que cubren el periodo de diciembre de 2005 y diciembre de 2006, fueron utilizadas para el estudio de la deformación cosísmica causada por el sismo de la Falla Morelia de magnitud moderada (Mw=5.4). A pesar de la decorrelación, una señal clara de la deformación paralela a la traza de falla superficial conocida y consistente con el fallamiento normal fue observada en las interferogramas de fase empacada. A parte de las observaciones satelitales de la deformación cosísmica, las señales claras de la deformación causada por el sismo del 24 de mayo de 2006 fueron detectadas por la nivelación, las observaciones del campo y los instrumentos geotécnicos (grietómetros, inclinómetros y piezómetros). Los parámetros de la fuente del sismo fueron estimados usando el modelado directo de los datos de la deformación de la superficie y de los cambios de la deformación volumétrica estática deducidos de cambios cosísmicos de nivel de agua subterránea. Los resultados de modelado confirman la poca profundidad del sismo y explican en parte porque este sismo se sintió con tanta fuerza en el área. El valor de la eficiencia de la deformación volumétrica estática fue obtenido y puede ser usado en los futuros estudios de los cambios del nivel de agua subterránea en el área de estudio debido a la deformación del terreno causada no solo por acontecimientos sísmicos pero también por deslizamiento asísmico o por actividad antropogénica. Basando en los resultados de la modelación teórica del flujo postsísmico la difusividad hidráulica fue estimada. El rango de valores estimados está en el buen acuerdo con los valores obtenidos en los otros estudios para la misma área (Glowacka y Nava, 1996; Glowacka *et al.*, 2010), y está dentro de rango de la difusividad para las fallas sismogénicas especificadas por Talwani y Acree (1984/1985).

Palabras Clave: Interferometría Diferencial de imágenes de Radar de Apertura Sintética, deformación del terreno, antropogénica, tectónica, cosísmica, Valle de Mexicali, Campo Geotérmico de Cerro Prieto, Sismo de Falla Morelia.

DEDICATION

This thesis is dedicated to…

the members of my family, who have always supported and encouraged me to do my best in all matters of life.

all that are dear to me.

ACKNOWLEDGEMENTS

The work presented in this thesis is the results of a Ph.D. study following the Ph.D. program at CICESE (Centro de Investigación Científica y Educación Superior de Ensenada), Center for Scientific Research and Higher Education of Ensenada. I simply could not have been able to finish this without the help of a lot of people. They all have my sincere gratitude.

In the first place, I would like to express my sincere appreciation and gratitude to my supervisor Dr. Ewa Glowacka for her constant help, encouragement, stimulating and invaluable advice and patient guidance throughout the entire course of this thesis.

I would like to thank Dr. Robert Mellors from the San Diego State University for taking time out from his busy schedule to serve as my external committee member. His support, suggestions and advices helped me to understand and concrete my knowledge on DInSAR basic principles, processing and applications.

I am very grateful to the remaining members of my thesis committee, Dr. Fidencio Alejandro Nava Pichardo, Dr. Rogélio Vazquez Gonzalez and Dr. Juan Contreras Pérez, for the assistance they provided at all levels of the research project. Their academic support and input and personal cheering are greatly appreciated.

I am thankful to administrative and technical staff members of the CICESE who have been kind enough to advise and help in their respective roles. Francisco Farfan, Guillermo Diaz de Cossio, María de la Cruz González, Martha Barrera, Enid Moran, Dolores Sarracino, Citlalli Romero, Ivonne Best, deserve special mention.

I am thankful to CICESE for hosting my research and providing me with the necessary facilities.

This research was, at various times, supported by SRE (Secretaría de Relaciones Exteriores), the Mexican Secretary of Foreign Affairs, CICESE, CONACYT (Consejo Nacional de Ciencia y Tecnología), the Mexican National Council of Science and Technology (project 45997-F), CONAGUA (Comisión Nacional del Agua), the Mexican Water Commission (project COE003). I would like to express my gratitude to all my fellowship sponsors.

The Envisat ASAR images were provided by European Space Agency (ESA) as a part of ESA Cat-1 Project (ID - C1P3508).

I also would like to thanks to all my friends, thank you for your company and encouragement.

I am eternally grateful to my beloved parents, parents in law, brothers, and step-daughter for their moral support and patience during my studies. Very special thanks, of course, to my husband Jose, for his constant love and strength throughout all those years.

Finally, I would like to thank everybody who was important to the successful realization of thesis, as well as expressing my apology that I could not mention personally one by one.

SYNOPSIS (SPANISH)

Las deformaciones de terreno son problemas de gran importancia sobretodo en las zonas de rápido crecimiento urbano y son la expresión superficial de varios procesos físicos. Estos incluyen eventos sísmicos, erupciones volcánicas, derrumbamientos y subsidencia del terreno. La ocurrencia de dichos procesos puede ser debido a los factores naturales o antropogénicos, o combinación de ambos. El monitoreo, análisis, interpretación y predicción de las deformaciones del terreno requieren de estudios multidisciplinarios que, al final, permiten un mejor entendimiento de sus factores causantes y mecanismos. Estos estudios son también un elemento crítico en valuación y mitigación de peligros naturales y antropogénicos.

El Valle de Mexicali, situado en noreste de Baja California, México, es un ejemplo de una región inestable, donde las deformaciones del terreno se han puesto cada vez más evidentes en zonas urbanas y rurales. Varios mecanismos, incluyendo la tectónica activa, actividad volcánica y antropogénica, producen cambios rápidos en la topografía de esta área. Por esta razón, el Valle de Mexicali es un laboratorio natural para el estudio del fenómeno de las deformaciones de la superficie terrestre.

Las deformaciones del terreno en el Valle de Mexicali han sido monitoreadas por una serie de nivelaciones de precisión y GPS (Global Positioning System), Sistemas de Posicionamiento Global, conducidos principalmente por la Comisión Federal de Electricidad (CFE), y actualmente se monitorean con una red de instrumentos geotécnicos (inclinómetros, extensómetros y piezómetros) de medición semi-continua, instalada y mantenida por Centro de Investigación Científica y Educación Superior de Ensenada (CICESE) con el suporte financiero de Consejo Nacional de Ciencia y Tecnología (CONACYT).

Estas técnicas terrestres proporcionan la información precisa de las velocidades de desplazamiento de una serie de puntos discretos en una superficie que se está deformando. Sin embargo, la colección de datos usando estas técnicas es costosa, y consumidora de tiempo. Por otra parte, requieren una gran cantidad de observaciones, que no son siempre posibles.

Los recientes desarrollos en la percepción remota y la tecnología satelital han permitido obtener las imágenes de radar de la superficie terrestre de alta resolución. Usando la técnica conocida como DInSAR (Differential Interferometric Synthetic Aperture Radar), Interferometría Diferencial de Radar de Apertura Sintética, pares de imágenes se pueden ser procesados para obtener mapas de alta resolución de la deformación superficial con una cobertura espacial grande (~100×100 km^2), con precisión en orden de centímetros (Gabriel *et al.*, 1989; Bürgmann *et al.*, 2000; Hanssen, 2001).

Los trabajos previos, usando un número de imágenes del radar limitado, habían demostrado que la técnica DInSAR puede ser usada para el estudio de deformaciones del terreno en el Valle de Mexicali (Carnec y Fabriol, 1999; Hanssen, 2001). En esta tesis se utiliza una serie de imágenes de radar más grande conjuntamente con los datos de otros métodos disponibles.

El principal objetivo de este trabajo es mejorar el entendimiento y modelación de la distribución especial y temporal de las deformaciones de la superficie terrestre en el Valle de Mexicali, combinando las observaciones del satélite con los datos geológicas, geodésicos y de medicines geotécnicos. Y el trabajo está enfocado en examinar:

1. La deformación antropogénica relacionada con la extracción de fluidos geotérmicos en el campo Geotérmico Cerro Prieto.
2. La deformación tectónica relacionada con el sismo de Falla Morelia de magnitud moderada (Mw=5.4) ocurrido en el Valle de Mexicali el 24 de Mayo de 2006.

En esta tesis también ha sido posible evaluar las capacidades y limitaciones de la técnica de DInSAR para el estudio de las deformaciones en el Valle de Mexicali.

Para los propósitos de este trabajo se usaron los datos de:

- Nivelación de precisión de segundo orden, primera clase (precisión 6 mm/km$^{1/2}$) de periodos: 1994-1997 (Lira y Arellano, 1997; Glowacka *et al.*, 1999), 1997-2006 (Glowacka *et al.*, 2006), y Febrero 2006 - Junio 2006 (perfil corto, que consistió de 7 bases de medición).
- Estudios geotectónicos que fueron realizados por González *et al.* (1998), Glowacka *et al.* (2006; 2010), y Suárez-Vidal *et al.* (2007; 2008) con el propósito de documentar rasgos de rompimiento, fracturas y desplazamientos.

- Instrumentos geotécnicos grietómetros e inclinómetros de la red de Instrumentos geotécnicos de Mexicali (Glowacka, 1996; Glowacka *et al.*, 2007; 2008).
- Piezómetros de la red piezométrica de Mexicali (Vázquez González, 1999; Vázquez González *et al.*, 2005).
- DInSAR. Para procesamiento interferométrico se usaron 28 imágenes complejos ASAR (Advanced Synthetic Aperture Radar), Radar de Apertura Sintética Avanzado, del satélite Envisat (Environmental satellite), Satélite Ambiental, adquiridos en el periodo entre Octubre 2003 y Diciembre 2006. Estas imágenes fueron proporcionadas por ESA (European Space Agency), Agencia Espacial Europea, como parte de proyecto científico (C1P3508).

Esta tesis está dividida en seis capítulos. A continuación se describe brevemente el contenido de cada capítulo.

En el capítulo II se presenta la información general acerca localización, tectónica y sismicidad del área de estudio. También se presenta un análisis de trabajos previos acerca la deformación en el área de estudio.

El Valle de Mexicali se localiza en el noreste de la península de Baja California, al sur de la frontera internacional. Es un llano aluvial, relativamente plano con la única característica topográfica prominente que es el volcán Cerro Prieto que se localiza en su límite oeste.

El Valle de Mexicali se localiza dentro de una zona tectónicamente muy activa, en la parte sur de la cuenca Saltón, en el límite entre las placas Pacifico y Norteamérica. Existen dos fallas principales en el área del estudio, Imperial y Cerro Prieto, de la orientación NO-SE, del movimiento lateral derecho, que afectan el basamento y delimitan la cuenca tectónica Cerro Prieto. La formación de esta cuenca se debe al régimen tectónico extensional impuesto por el movimiento de estas fallas.

La cuenca tectónica Cerro Prieto tiene una profundidad máxima de más de 6000 metros, esta rellena de sedimentos aluviales y deltaicos, que abarcan edades desde el Terciario hasta el Reciente (de la Peña y Puente, 1979), que ha experimentado la deformación continua, al alto flujo de calor, la actividad sísmica, volcánica y hidrotermal. Dentro de la cuenca existen varias fallas normales con dirección predominante oblicua a las trazas de fallas principales, por ejemplo, Falla Morelia, Falla Saltillo, Falla H y etc. (Elders *et al.*, 1984; Lippmann *et al.*, 1984; González, 1999; Suárez-Vidal *et al.*, 2008).

Debido a la complicada situación tectónica el área de estudio se encuentra en una zona sísmicamente muy activa. Los sismos de magnitudes grandes mayores a 6 ocurren a lo largo de las fallas principales. El mecanismo de fallamiento dominante a lo largo de las fallas principales es de rumbo lateral derecho (Albores *et al.*, 1980; Frez y González, 1991). El área, situada entre la terminación norte de la falla Cerro Prieto y la terminación sur de la falla Imperial, se conoce como Zona Sísmica de Mexicali (MSZ) y está dominada por enjambres sísmicos. La mayor parte de esta actividad sísmica está relacionada con las fallas normales. Por esa razón el mecanismo de fallamiento dominante dentro de la cuenca Cerro Prieto es normal (Fabriol y Munguía, 1997; Gonzalez *et al.*, 2001).

La presencia de gruesa secuencia sedimentaria, tectónica extensional, el alto flujo del calor, las fallas activas, y las infiltraciones de aguas del rio de Colorado crearon las condiciones para la formación de los reservorios geotérmicos que forman parte del campo geotérmico de Cerro Prieto.

La extracción de fluido en el Campo Geotérmico Cerro Prieto (Cerro Prieto Geothermal Field, CPGF) inició en el 1973 y en 1989 inició la inyección de salmuera, influyendo estado de esfuerzos, deformaciones y sismicidad de la zona. El modelo hidrológico del CPGF establecido por Lippmann *et al*. (1991) sugiere que la salmuera caliente recarga dos reservorios profundos (γ y β) subiendo por la Falla H. Después este fluido caliente fluye atreves de reservorios hacia oeste y, atreves de una zona permeable, entra al reservorio mas somero (α). Este reservorio está conectado con la falla L, por la cual los fluidos suben hacia acuíferos someros y se descargan a la superficie al oeste-suroeste del campo, formando fuentes calientes y fumarolas. Es generalmente aceptado, que bajo el régimen de extracción de fluidos, los reservorios geotérmicos también se recargan con agua fría proveniente de los acuíferos, localizados en este, oeste y sur por las zonas de fallas.

En el Valle de Mexicali, hasta los años 90 las deformaciones observadas se atribuían solamente al tectonismo natural. Sin embargo, tras casi 40 años de extracción de fluidos, estudios geodésicos, monitoreo geotécnico y estudios geotectónicos, fue posible de determinar que la tasa de deformaciones del terreno, principalmente subsidencia, actuales están relacionadas, principalmente con la extracción de fluidos. Esto fue sugerido por el análisis de datos de nivelación y datos de la producción históricos realizado por Glowacka *et al.*, 1999 y la modelación de la componente tectónica y antropogénica de la subsidencia observada realizada por Sarychikhina, 2003 y Glowacka *et al.*, 2005. En el primer trabajo se encontró que en el período analizado la tasa de subsidencia aumentó después de cada aumento grande, sostenido, de extracción. La tasa de subsidencia observada de 12 cm/año es demasiado grande por ser causada solo por tectónica. El máximo de subsidencia se localizo en la zona de pozos de extracción. En la modelación se encontró que la subsidencia antropogénica es responsable del 94% al 96% de la subsidencia observada.

Sin embargo, las observaciones geotectónicos en el campo de Glowacka *et al.*, 2006, Suarez *et al.*, 2008 y las mediciones de instrumentos geotécnicos, Glowacka *et al.*, 1999, 2007, 2008, sugieren que la geometría de la subsidencia observada está controlada por fallas tectónicas.

La tasa de subsidencia alta y correlación espacial entre la localización del máximo de deformación y zona de pozos de extracción fueron confirmados por la técnica de DInSAR en trabajos de Carnec y Fabriol (1999) y Hannsen (2001). Las imágenes de satélites europeos ERS1/2 adquiridas en el periodo de 1993-1997 y 1995-1997, respectivamente, fueron usadas. No les fue posible, definir la extensión de la zona de hundimiento debido a la baja calidad (baja coherencia) de los datos de DInSAR en las zonas alrededor del campo, causada por la presencia de vegetación en los campos agrícolas. Los datos confiables de la deformación fueron obtenidos solo en zona desértica del CPGF. Estos autores también realizaron la modelación de la deformación observada usando los cuerpos de Mogi. La localización y profundidad de los cuerpos del modelo de mejor ajuste coincidió con la localización y profundidad de los reservorios geotérmicos.

En el capítulo III se presenta una breve introducción a la teoría básica requerida para entender la técnica de DInSAR y los principales pasos del procesamiento interferométrico basando en los trabajos de Massonnet y Rabaute (1993), Gens y Vangenderen (1996), Bamler y Hartl (1998), Henderson y Lewis (1998), Massonnet y Feigl (1998), Price y

Sandwell (1998), Bamler (2000), Bürgmann *et al.* (2000), Rosen *et al.* (2000) and Hanssen (2001). Los posibles errores y limitaciones de la técnica también se discuten.

Los sistemas de SAR (Synthetic Aperture Radar), Radar de Apertura Sintética, son sistemas de radares coherentes que generan imágenes de alta resolución. Una apertura sintética o antena virtual, consiste en un extenso arreglo de sucesivas y coherentes señales de radar que son transmitidas y recibidas por una pequeña antena que se mueve a lo largo de un determinado recorrido de vuelo u órbita. El procesamiento de la señal usa las amplitudes y fases de la señal recibida sobre sucesivos pulsos para crear una imagen. Las imágenes SAR expresan la distribución espacial de la amplitud y la fase de la señal retornada por el terreno u los objetos presentes en la escena o área barrida por el satélite. La amplitud está directamente relacionada con las propiedades dieléctricas (reflectividad) del terreno. Por otra parte, la fase de la señal está vinculada con la distancia entre el sensor (satélite) y el suelo para cada pixel. Además la señal reflejada puede sufrir un posible desfase debido a reflectividad del terreno, a la propagación de la señal a través de la atmósfera, y al ruido.

La interferometría SAR (Synthetic Aperture Radar), InSAR, es una técnica geodésica establecida, basada en la combinación de dos imágenes SAR de la misma escena, adquiridas desde puntos ligeramente diferentes. Esta combinación da como resultado una nueva imagen conocida como interferograma. La toma de imágenes puede ser simultánea, tomándose las imágenes mediante dos antenas ligeramente separadas o de forma secuencial. En este último caso, la primera imagen es la imagen de referencia llamada *master*, mientras que la segunda (adquirida con fecha posterior a la primera) es llamada imagen *slave*. Suponiendo que las fases de reflectividad del terreno y de retraso atmosférico son las mismas en ambas imágenes, y que el ruido en ambas imágenes puede ser omitido, la fase del interferograma (fase interferométrica) será calculada restando las fases de las dos imágenes SAR. En condiciones previamente mencionadas, la fase interferométrica es proporcional a la diferencia de caminos recorridos por la señal durante dos adquisiciones.

Debido a la diferencia en la geometría de las adquisiciones, la diferencia en caminos recorridos por la señal es la suma de varias contribuciones producidas por una superficie de referencia sin relieve, topografía, y la deformación.

La técnica de InSAR diferencial (DInSAR) clásica trata de eliminar las componentes relacionadas con la superficie de referencia y topografía para obtener la fase relacionada con las deformaciones del terreno. La contribución de una superficie de referencia (también conocida como contribución orbital) puede ser estimada usando órbitas precisas. La contribución topográfica puede ser simulada a partir de un modelo digital de elevación externo o estimada de un interferograma independiente y después restada del interferograma original.

Debido al carácter cíclico de la fase, la fase interferométrica se obtiene con valores comprendidos entre 0 y 2π (o entre $-\pi$ y π), es decir, la fase interferométrica tiene modulo 2π, y se le conoce como fase enrollada. El procedimiento que se utiliza para recuperar la fase original de la señal se llama desenrollo de fase (phase unwrapping), y es un paso importante en el procesamiento interferométrico. La sensibilidad de la fase interferométrica para detectar deformación es muy alta. Cada franja equivale aproximadamente a una diferencia de distancia (deformación) de en la línea de la observación del radar (Line Of Sight), LOS.

La calidad de los datos de deformación del terreno obtenidos usando la técnica de DInSAR depende de la calidad de la fase interferométrica diferencial. El parámetro usado para evaluar la calidad de fase es denominada coherencia interferométrica, que puede ser interpretada como una herramienta útil para medir la semejanza entre las dos imágenes SAR.

La coherencia se encuentra definida entre los valores 0 y 1. Si la coherencia es igual a cero, significa que la escena está completamente decorrelacionada y así el interferograma es ruido y no está relacionado con la deformación. En el otro extremo, una coherencia cercana a uno corresponde a un interferograma libre de ruido a partir de cual un mapa de deformación de alta calidad puede ser generado.

Las fuentes de decorrelación (o degradación de coherencia) son la decorrelación temporal y decorrelación espacial.

La decorrelación temporal se debe a las variaciones de reflectividad de los puntos de la imagen que pueden ser causadas por: lluvia, viento sobre la vegetación, crecimiento de la misma, arado de campos, etc.

La decorrelación espacial se debe a cambios en la geometría de adquisición de las imágenes. La degradación de correlación aumenta mientras aumenta la distancia que hay entre los satélites en el momento de realizar las adquisiciones, también conocida como línea de base. La componente de la línea de base perpendicular a la dirección de observación tiene mayor influencia en el grado de decorrelación espacial.

Los errores orbitales y topográficos son los otros factores que afectan la fase interferométrica diferencial y pueden crear confusión en su interpretación.

La componente atmosférica representa otra importante fuente de error. Las imágenes al no ser adquiridas al mismo tiempo pueden haber sido tomadas en condiciones atmosféricas diferentes, por lo que varía el camino eléctrico recorrido por la señal. Los mapas de coherencia no pueden medir este ruido. Teniendo en disposición solo un par de imágenes SAR la identificación de artefactos atmosféricos y su cuantificación es una tarea imposible sin usar la información externa (GPS, MERIS, MeteoSat). En algunos casos los artefactos atmosféricos pueden ser ignorados (alta tasa de deformación o patrón espacial especifico). En casos donde varias imágenes están disponibles, la comparación de múltiples interferogramas puede ayudar a identificar las imágenes que son afectadas gravemente por perturbaciones atmosféricas. La suposición principal es que la fase de la deformación es altamente correlacionada entre los pares independientes de imágenes y los términos del error no lo son. La combinación de múltiples interferogramas, por lo tanto, también puede ayudar a reducir la influencia de los artefactos atmosféricos.

El procesamiento interferométrico, realizado usando el software DORIS versión 3.16 (Kampes, 2005; Kampes *et al.*, 2003; Kampes y Usai, 1999), incluyó los siguientes pasos:

• Coregistro de las imágenes, que consiste en hacer corresponder los pixeles de una y otra imagen.

• Generación de interferograma (diferencia de fase). La fase del interferograma aparece enrollada en modulo de 2π. El factor de multi-look (o promediado de pixeles) usado es de 4×20 pixeles, lo que permite generar los productos interferométricos con tamaño de pixel de $\sim100\times100$ m^2.

• Generación de imagen de coherencia.

• Corrección de interferograma por la geometría de adquisición de los datos: corrección por superficie de referencia y corrección por topografía, se realiza usando los datos de orbitas precisas de DEOS (Delft institute for Earth-Oriented Space research) y el modelo digital de elevación de SRTM3 (Shuttle Radar Topography Mission) con una resolución de 3 segundos de arco.
• Filtración de la fase interferométrica usando el filtro de Goldstein (Goldstein y Werner, 1998) y desenrollo de la fase interferométrica usando el software SNAPHU (Chen y Zebker, 2000, 2001)) integrado como módulo a DORIS.
• Conversión de la fase desenrollada al desplazamiento LOS y geocodificación de la información obteniendo como resultado el mapa de desplazamiento LOS en coordenadas geográficas y datum NAD27.

En el capítulo IV se presenta el análisis de cambios espaciales y temporales en el patrón de la subsidencia antropogénica en el Valle de Mexicali. Para el análisis fueron usados 17 imágenes SAR de paso descendente # 84, escena 2961, y 5 imágenes de paso ascendente # 306, escena 639 adquiridos en el periodo de Octubre 2003 a Mayo 2006 por el satélite Envisat. Las imágenes adquiridos después de Mayo 2006 no han sido incluimos en el análisis para no contaminarlo con la deformación causada por el sismo de Mayo 24 de 2006.

Durante el procesamiento interferométrico de pares de imágenes SAR individuales se observo una decorrelación espacial muy fuerte para los pares cuya línea de base perpendicular era mayor que 400 m, dichos pares han sido excluidos del análisis. Limitando la línea de base, los pares interferométricos mas incoherentes han sido eliminados, sin embargo, también se redujo considerablemente el número de pares para el análisis.

Posteriormente, mediante un análisis visual, los interferogramas individuales han sido comparadas ente sí, con el fin de identificar franjas con la localización geográfica común en diversos interferogramas. El análisis visual de interferogramas también ayuda a identificar los pares interferométricos con ruido fuerte de la fase. Así se encontró que, a pesar de línea de base corta, varias interferogramas diferenciales presentan alto nivel de ruido de fase que se debe a la decorrelación temporal de la señal, inducido por variaciones en las características dieléctricas de las blancos, entre las dos adquisiciones. Las zonas alrededor del CPGF, con intensa vegetación debido a su uso agrícola, presentan importantes decorrelaciones de fase para los pares interferométricos que cubren el período mayor a tres meses (105 días), mientras que para el área de CPGF y la zona principalmente desértica al oeste del campo mantiene buena coherencia (no presentan decorrelación de fase) durante los períodos cubiertos por pares interferométricos más largos.

En todos los interferogramas diferenciados que cubren los periodos cortos se observa que la zona de alta tasa de subsidencia se encuentra al este de la laguna de evaporación y tiene la extensión en dirección de Noreste, perpendicular a las fallas principales. Esta zona tiene dos centros aisladas de alta tasa de subsidencia: el primer centro del hundimiento está situado en la zona de la producción de CPGF, cerca de su límite este, y el segundo está situado en el área entre el límite este del CPGF y la falla Saltillo, que fue propuesto como la zona de la recarga en los estudios previos (Glowacka *et al*., 1999; Sarychikhina, 2003). A pesar de alto nivel del decorrelación de la fase en los pares interferométricos que cubren los intervalos de tiempo más largos, el mismo patrón de las franjas se puede ser visualmente trazado en la zona de la producción de CPGF, en donde los contornos de las franjas muestran un centro de subsidencia de forma elíptica.

El análisis de interferogramas diferenciales confirma que la extensión de área afectada por subsidencia está controlada por las fallas tectónicas. La forma de área afectada por subsidencia coincide con la forma de la cuenca tectónica Cerro Prieto (Suárez –Vidal *et al.*, 2008).

Para calcular la tasa de hundimiento anual el método de apilamiento (stacking) de interferogramas diferenciales ha sido aplicado. El apilamiento de interferogramas diferenciales implica sumar las interferogramas diferenciales individuales para recibir un solo interferograma. Esto es útil para superar los dos defectos de DInSAR convencional: la coherencia baja sobre separaciones temporales largas y la influencia atmosférica. Cuatro interferogramas consecutivas con separaciones temporales entre 70 y 105 días, fueron seleccionados para el apilamiento.

Antes de apilamiento las interferogramas individuales han sido desempacadas, convertidas a desplazamiento LOS y referenciadas a un punto fijo que es el punto fijo para la nivelación de 1997-2006.

El resultado de apilamiento es un mapa de desplazamiento LOS que cubre 350 días. Normalizamos este resultado por 365 días para obtener la tasa de desplazamiento LOS anual. El patrón espacial de la zona de subsidencia obtenido usando el método de apilamiento de interferogramas diferenciales es similar al patrón de subsidencia en interferogramas individuales. Usando este método encontramos la tasa de desplazamiento LOS de 16 cm/año en la zona recarga y 10 cm/año para la zona de pozos de extracción.

El modelo matemático de fractura tensional rectangular ha sido usado para modelar el desplazamiento LOS observado por DInSAR. El modelo fue basado en modelo hidrológico del campo e incluyó la información acerca las zonas de rupturas y fisuras del mapeo geotectónico y datos de pozos. El modelo final consiste de siete fracturas rectangulares: cuatro corresponden a reservorios geotérmicos y tres representan los acuíferos de recarga. La comparación del desplazamiento observado y estimado muestra un razonable acuerdo entre ambos con discrepancias entre 0 y 6 cm.

Basando en la estructura del modelo, información geotectónica y patrón de subsidencia observada ha sido posible definir tres áreas donde se puede esperar la presencia de fallas desconocidas hasta este momento.

Para evaluar los cambios en el patrón espacial y la tasa de deformación, los datos de desplazamiento LOS obtenidos usando el método de apilamiento de interferogramas diferenciales ha sido comparados con los resultados de nivelación de 1994-1997 y 1997-2006 (Glowacka *et al.*, 1999, 2006). Esta comparación reveló que la tasa de deformación promedia aumentó desde 1997. El máximo incremento en la tasa de deformación se observa en la zona de recarga. El centro de deformación en la zona de producción del CPGF ha migrado en la dirección noreste. Los cambios en el patrón de deformación del terreno pueden ser causados por el aumento de la producción en la CPGF debido a la nueva planta eléctrica (CPIV) que comenzó a operar en 2000 en la parte oriental de campo, como ha sido sugerido por Sarychikhina *et al.,* 2007 y Glowacka *et al.*, 2010.

En el capítulo V se analiza la deformación del terreno y cambios de nivel de agua subterránea causados por el sismo de magnitud moderada Mw=5.4 que ocurrió en el Valle de Mexicali el 24 de mayo de 2006. También fueron modelados los parámetros de fractura cosísmica usando los datos mencionados.

El evento se relaciona con la falla Morelia que es una falla normal activa oblicua a las falla principales de la zona y con el echado hacia sureste. Las rupturas de la superficie generados por el evento fueron reportadas por varias compañas del campo y tienen la extensión de más de 5 km con el máximo desplazamiento vertical hasta 30 cm y desplazamiento horizontal menor a 2-4 cm (Lira, 2006; Suárez-Vidal *et al.*, 2007). No se encontraron evidencias de la ruptura al lado oeste de la laguna de evaporación. Los rastros visibles de la ruptura superficial sugieren que el fallamiento se produjo en dos segmentos subparalelos en vez de uno solo (Munguía *et al.,* 2009).

Las deformaciones del terreno causados por el sismo fueron medidos por un perfil de nivelación cuasi perpendicular a la falla Morelia y que consiste de siete puntos de medición. La nivelación reporta 20 cm del desplazamiento vertical.

El grietómetro vertical instalado en la falla Morelia también reporta el desplazamiento vertical del orden de 20-25 cm. Adicionalmente, el grietómetro vertical instalado en la falla Saltillo reporta el desplazamiento vertical en esta falla disparado por el sismo. Los inclinómetros reportan cambios de inclinación del terreno de magnitud variable causados por el sismo.

En un intento por complementar las observaciones superficiales y ganar una comprensión mejorada de la distribución espacial de la deformación cosísmica del terreno, fue utilizado el método de DInSAR. 5 interferogramas diferenciales que cubren el periodo cuando ocurrió el sismo han sido obtenidos a partir de imágenes SAR adquiridas por satélite Envisat. Desafortunadamente, el área afectada por el sismo demostró considerable decorrelación en todos los interferogramas diferenciales. Esto es debido en parte a la actividad agrícola en la zona; el mismo problema se observaba también en otros interferogramas que no cubrían el tiempo de ocurrencia del sismo. Es probable que la decorrelación en el campo cercano a la ruptura superficial se deba a los gradientes altos de la deformación. A pesar de la decorrelación, una señal clara se puede detectarse en los interferogramas diferenciales. Esta señal aparece como una serie de franjas paralelas a la ruptura superficial. Debido a que las franjas ocurren en interferogramas independientes, se puede afirmar que no son debido a los efectos atmosféricos. En el interferograma de mejor calidad se puede distinguir al menos 5 franjas al sureste de la ruptura superficial observada, lo que corresponde a por lo menos 14 cm de desplazamiento LOS o 15 cm desplazamiento vertical. Las franjas no se observan al oeste-suroeste de la laguna de evaporación (y del epicentro) que, junto con las observaciones del campo, sugiere que el hipocentro se localizó en la terminación suroeste de la ruptura que se propagó hacia noreste. Debido a la coherencia baja de los interferogramas diferenciales, es difícil desempaquetar los sin graves errores de desempaque. Por lo tanto el análisis se centro en los interferogramas diferenciales de fase empacada.

El área entre la terminación norte de la falla Cerro Prieto y terminación sur de la falla Imperial es afectada por la deformación antropogénica continua. Por lo tanto los datos de nivelación y de DINSAR deben de contener una componente antropogénica. Para estimarla usamos un interferograma diferencias que cubre previo al sismo.

Durante el sismo de 24 de Mayo de 2006 6 piezómetros de los 8 que tiene la red piezométrica del Valle de Mexicali estaban en funcionamiento y registraron el cambio del nivel de agua subterránea a la hora del sismo. El cambio, que ocurrió en forma de repentina tuvo de hasta 6.7 m de amplitud (PZ-1) que es el pozo más profundo y más cercano al epicentro. Los otros pozos demostraron cambios en nivel de agua en la orden de 1 a 55 cm. II-9 no tenia equipo pero presentó el flujo artesial. Después del sismo del 24 de mayo de 2006 el nivel de agua subterránea elevado o disminuido comenzó a recuperarse gradualmente (excepto el nivel de agua subterránea en el PZ-7) como resultado de la difusión de la presión causada por un gradiente de presión en el acuífero de el cual causa la recarga o la descarga a las formaciones que lo rodean. En PZ-7 el nivel de agua subterránea continuo decaer gradualmente después del terremoto del 24 de mayo de 2006 que produjo baja en nivel de agua. Este fenómeno se relaciona posiblemente con la salida del agua subterránea por las fracturas inducidas por el terremoto según lo propuesto King *et al.*

(1999). El nivel de agua subterráneo en pozos PZ-1 PZ-3 y C-3 tuvo algunos cambios relacionados con las replicas de magnitud mayor que 4.

Los cambios en niveles de agua subterránea y tasas de la descarga de los ríos asociados con los sismos han sido ampliamente reportados (Roeloffs, 1996, King *et al.*, 2006). Las descripciones comprensivas de estos fenómenos se dan en Roeloffs (1988, 1996, 1998), Quilty y Roeloffs (1997) y Shibata *et al.* (2003). Se espera que la deformación impuesta por un sismo produzca un cambio en nivel de agua subterránea. En un simple modelo lineal, los niveles de agua subterránea bajan o suben dependiendo de si el acuífero conectado se dilata o se contrae debido a la redistribución sismogénica del campo de deformación inducido. Las amplitudes del cambio del nivel de agua subterránea producido por la deformación cosísmica son proporcionales al campo de deformación volumétrica estática. La constante de proporcionalidad se denomina la eficiencia de la deformación volumétrica estática.

Los parámetros de la fuente del sismo fueron estimados usando el modelado directo de los datos de la deformación de la superficie (DINSAR, nivelación, grietómetro vertical, observaciones de campo) y de los cambios estáticos de la deformación volumétrica deducidos de cambios cosísmicos de nivel de agua subterránea. Los resultados de modelado confirman la poca profundidad del sismo y explican en parte porque este sismo se sintió con tanta fuerza en el área. El valor de la eficiencia de la deformación volumétrica estática fue obtenido y puede ser usado en los futuros estudios de los cambios del nivel de agua subterránea en el área de estudio debido a la deformación del terreno causada no solo por acontecimientos sísmicos pero también por deslizamiento asísmico o por actividad antropogénica.

Basando en los resultados de la modelación teórica del flujo postsísmico la difusividad hidráulica fue estimada. El rango de valores estimados está en el buen acuerdo con los valores obtenidos en los otros estudios para la misma área (Glowacka y Nava, 1996; Glowacka *et al.*, 2010), y está dentro de rango de la difusividad para las fallas sismogénicas especificadas por Talwani y Acree (1984/1985).

En el capítulo VI se presentan las conclusiones de esta tesis y recomendaciones para los futuros trabajos de investigación.

CONTENTS

Page

CONTENTS (continue)

Page

LIST OF FIGURES

LIST OF FIGURES (continue)

Figure **Page**

LIST OF FIGURES (continue)

Figure **Page**

LIST OF FIGURES (continue)

Figure **Page**

LIST OF FIGURES (continue)

LIST OF FIGURES (continue)

LIST OF FIGURES (continue)

Figure **Page**

LIST OF FIGURES (continue)

Figure **Page**

LIST OF FIGURES (continue)

Figure **Page**

LIST OF FIGURES (continue)

LIST OF TABLES

LIST OF TABLES (continue)

Table **Page**

LIST OF ACRONYMS

ASAR: Advanced Synthetic Aperture Radar

BSSA: Bulletin of the Seismological Society of America

CICESE : Centro de Investigación Científica y Educación Superior de Ensenada, Center for Scientific Research and Higher Education of Ensenada

CFE: Comisión Federal de Electricidad, Mexican Power Company

CMT: Centroid Moment Tensor

CONACYT: Consejo Nacional de Ciencia y Tecnología, Mexican National Council of Science and Technology

CONAGUA: Comisión Nacional del Agua, Mexican Water Commission

CPGF: Cerro Prieto Geothermal Field

DEM: Digital Elevation Model

DEOS: Delft Institute for Earth-oriented Space Research

DInSAR: Differential Interferometric Synthetic Aperture Radar

DORIS: Delft Object-oriented Interferometric Software

EM spectrum: Electromagnetic spectrum

Envisat: Environmental satellite

ERS1/2: European Remote Sensing Satellites 1 and 2

ESA: European Space Agency

Getorb: Envistat and ERS1/2 orbit interpolation program developed at DEOS

GMT: Generic Mapping Tool

GPS: Global Positioning System

InSAR: Interferometric Synthetic Aperture Radar

LOS: Line Of Sight

MERIS: Medium Resolution Imaging Spectrometer

MSZ: Mexicali Seismic Zone

LIST OF ACRONYMS (continue)

NAD27: North American Datum 1927

NASA: National Aeronautics and Space Administration

ODR: Orbital Data Records

PRF: Pulse Repletion Frequency

RADAR: Radio Detection And Ranging

RAR: Real Aperture Radar

RMS: Root Mean Square

SAR: Synthetic Aperture Radar

SLAR: Side Looking Airborne Radar

SLC: Single Look Complex

SNAPHU: Statistical-cost, Network-flow Algorithm for Phase Unwrapping

SNR: Signal-to-Noise Ratio

SRTM: Shuttle Radar Topography Mission

WGS84: World Geodetic System 1984

CHAPTER I

INTRODUCTION

I.1 Problem definition

Ground deformation is the surface expression of various physical processes. These include earthquakes, volcanic eruptions, landslides and subsidence. Moreover their occurrence could be due to natural or anthropogenic factors, or to combination of both. Such changes of the Earth's surface pose serious threats to communities. Precise mapping, monitoring, analysis, and modeling of ground-surface deformation are required to provide a better understanding of its causes, triggering factors, and mechanisms. These studies are also a critical element in the assessment and mitigation of natural and anthropogenic hazards.

The Mexicali Valley, located in northeastern Baja California, Mexico (Figure 1), is an example of an unstable region where ground deformation has become increasingly evident in many urban and rural areas. Several mechanisms, including active tectonics, volcanic, and human activity, produce rapid changes in the topography of this area. For this reason the Mexicali Valley is a natural laboratory for the study of ground deformation.

Ground deformation in the Mexicali Valley has been monitored by repeated ground surveys with precise leveling and GPS (*Global Positioning System*), done mainly by the CFE (*Comisión Federal de Electricidad*), the Mexican Power Company; and is currently being monitored quasi-continuously by a network of geotechnical instruments (tiltmeters, crackmeters and piezometers) maintained by CICESE (*Centro de Investigación Científica y Educación Superior de Ensenada*), the Center for Scientific Research and Higher Education of Ensenada, with financial support from CONACYT (*Consejo Nacional de Ciencia y Tecnología*), the Mexican National Council of Science and Technology. These terrestrial techniques provide accurate and precise information on the velocities of a series of discrete points on a deforming surface. However, data collection using these techniques is cumbersome, costly, and time consuming. Moreover they require a large number of observations, which are not always possible to collect. This in turn may lead to strong aliasing effects in the analysis of the data.

Recent developments in remote sensing and satellite technology have made possible high-resolution radar images of the Earth's surface. Using the method known as DInSAR, *Differential Interferometric Synthetic Aperture Radar*, pairs of images can be processed to obtain high resolution maps of surface deformation with large spatial coverage (~100×100 km^2) and accuracy on the order of centimeters (Gabriel *et al.*, 1989; Bürgmann *et al.*, 2000; Hanssen, 2001).

Previous works using limited data had shown that DInSAR was feasible in the Mexicali Valley (Carnec and Fabriol, 1999; Hanssen, 2001). This study will use a larger dataset of radar images, in combination with other available methods, to evaluate spatial and temporal distributions of crustal deformations in the Mexicali Valley, in order to explain the observed deformation pattern in the context of the tectonic and anthropogenic situation.

I.2 Objective of study

The main objective of this thesis is to improve the understanding and modeling of temporal and spatial distributions of surface deformation in the Mexicali Valley by combining satellite observations with ground based geological, geodetic, and geotechnical measurements. The purpose is to understand the causes of the surface deformation. This work is focused on examining:

1. The anthropogenic surface deformation related to extraction of geothermal fluids in the *Cerro Prieto Geothermal Field* (CPGF).
2. The tectonic surface deformation associated with the moderate magnitude (Mw=5.4) Morelia Fault Earthquake which occurred in the Mexicali Valley on May 24, 2006.

During the work, it was possible to compare DInSAR results to other geophysical and geodetic techniques in the Mexicali Valley. The procedures, strengths, and limitations of the technique are discussed.

I.3 Datasets

As mentioned in section I.1, the Mexicali Valley area is monitored by a network of continuously-recording geotechnical instruments, and well-piezometers, as well as by periodical leveling surveys. In addition, geological reports from private companies that have surveyed the area are available. In an attempt to supplement the surface observations and to gain an improved understanding of the temporal and spatial distribution of surface deformation, the data from ground-based techniques was combined with DInSAR data. In the following I provide a detailed description of the available datasets.

I.3.1 Geodetic leveling

Geodetic leveling measures elevation differences between benchmarks. By repeating surveys, highly accurate (mm scale) measurements of elevation changes (vertical displacements) over time can be obtained (Gobierno Federal, 1985, 1998). Leveling measurements in the Mexicali Valley began in the 1960's, as part of the Cerro Prieto geothermal field preparations (Velasco, 1963). These measurements have been repeatedly carried out up to the present, with varying frequency, precision, coverage, and density, mainly by CFE for monitoring of land elevation in the CPGF and surrounding area (García, 1978; Grannell *et al.*, 1979; de la Peña, 1981; Wyman, 1983; Lira and Arellano, 1997; Glowacka *et al.*, 1999; Lira, 1999), and as surveys for tectonics or earthquake studies (Darby *et al.*, 1981; de la Peña, 1981; Darby *et al.*, 1984; Lira, 1996; González *et al.*, 1998; Lira, 1998).

Three datasets of second-order, first class leveling surveys (6 $mm/km^{1/2}$ accuracy) were used in this thesis. The first, and most complete, set of precise leveling data was recorded during the 1994-1997 period (Lira and Arellano, 1997; Glowacka *et al.*, 1999). After filtering (discarding the data from benchmarks with evidently erroneous measures), this leveling dataset comprises 95 benchmarks. The reference point, assumed to be stable, is located to the SE of the study area, in the Cucapah ranges (benchmark "10004").

The second leveling dataset consists of data collected during two campaigns in 1997 and 2006 (Glowacka *et al.*, 2006) using the same benchmarks network as for the first leveling dataset. After filtering, this dataset comprises data from 67 benchmarks reporting the vertical displacement relative to the reference fixed point (benchmark "10037"). The different reference points for these datasets is due to the loss, probably by destruction, of benchmark "10004" sometime between the 1997 and 2006. Benchmark "10037" is also located to the SE of the study area, ~3 km northeast from the benchmark "10004". To compare both datasets we referenced the first 1994-1997 dataset to the benchmark "10037".

The third dataset corresponds to the precise leveling performed in the February 2006 and June 2006. This leveling dataset consist of 7 benchmarks along a profile crossing the Morelia fault (Figure 2). The length of this leveling profile is 4.75 km from which ~1.70 km is on the northwest side of the fault and 3.05 on the southeast side.

The first two precise leveling datasets were used to establish the spatial and temporal evolution of the anthropogenic deformation (see chapter IV), whereas the third dataset was used in the analysis and modeling of the coseismic deformation caused by the 24 May, 2006, Mw=5.4, Morelia Fault earthquake (see chapter V).

I.3.2 Geotechnical instruments network

Geotechnical instruments have operated in the Mexicali Valley since 1996 for continuous recording of deformation phenomena. To date, the network consists of three crackmeters and eight tiltmeters (Glowacka, 1996; Glowacka *et al.*, 2007; 2008).

Crackmeters (extensometers) measure fault slip (vertical or horizontal) by recording the displacement between 2 piers or monuments located on opposite sides of a fault. In this study we used data from two vertical crackmeters installed in the Saltillo and Morelia faults. These 3 m long crackmeters (Geokon Vibrating Wire, model 4420) span the fault in a plane perpendicular to it and angled with respect to the horizontal. The crackmeters have 70 cm range and 0.1 mm precision, and operate with a 5- 20 minutes sampling interval (Glowacka, 1996; Nava and Glowacka, 1999).

Tiltmeters are highly sensitive instruments used to measure changes in the inclination of the ground (rotation). These instruments are usually installed in boreholes to avoid spurious ground tilts produced by differential thermal expansion in near-surface materials and rainfall effects (Agnew, 1986). The data from two borehole tiltmeters and one surface tiltmeter (Applied Geomechanics, models 722 and 711) was analyzed in this thesis. These instruments are biaxial tiltmeters, which means that they measure two components (NS and EW in this case) of earth surface tilt. The tiltmeters have a measuring range of ±2000 μradian, resolution of 1μradian, and sampling interval of 1 - 4 minutes (Glowacka *et al.*, 2007; 2008). The geotechnical instruments records were used in chapter V for analysis of coseismic and postseismic ground level change and of coseismic displacement.

I.3.3 Piezometric network

Continuous monitoring of groundwater level has been performed since 2003, and consists of 8 wells equipped with Solinist Levelogger piezometers and 2 barometers. These instruments constitute the Mexicali Valley Piezometric Network whose purpose is to monitor water level in the shallow groundwater aquifer (Vázquez González, 1999; Vázquez González *et al.*, 2005). The instruments' sampling interval is 5 minutes and can determine the groundwater level depth with an accuracy of around 1 cm for piezometers (including 0.15 cm of barometric correction accuracy). Most wells are around 150m deep, except PZ-1 and II-9 which are 500m and 15m deep, respectively. The wells are drilled in unconsolidated delta deposits interbedded with alluvial sediments. The wells measure the groundwater level in the shallow, unconfined or partially confined, Mexicali Valley aquifer (Vázquez González *et al.*, 1998).

We used the information from 7 piezometers to evaluate coseismic and postseismic changes of groundwater level caused by May 24, 2006, earthquake (see chapter V). The barometer data was used to eliminate the atmospheric influence from the groundwater level data.

I.3.4 Geological field observation

Data from detailed field mapping of fractures, fissures, and collapse features related to tectonics and anthropogenic subsidence was used in the chapter IV. The data from coseismic surface rupture mapping was used in the chapter V of this thesis for constraining the May 24, 2006, earthquake source fault model. The data are from González *et al.* (1998), Glowacka *et al.* (2006; 2010), and Suárez-Vidal *et al.* (2007; 2008).

I.3.5 SAR images

Radar differential interferometry technique is based on the comparison of the phases of two *Synthetic Aperture Radar* (SAR) images acquired at different times (Massonnet and Rabaute, 1993; Gens and Van Genderen, 1996). In this study, 28 *Single Look Complex* (SLC) Envisat (*Environmental satellite*) ASAR (*Advanced Synthetic Aperture Radar*) images acquired over the study area between October 2003 and December 2006 were obtained from the *European Space Agency* (ESA), as part of ESA CAT-1 project (ID - C1P3508). The Envisat ASAR is a C-band (5.66 cm) radar and the look angle of the images is 23° degrees. The *Synthetic Aperture Radar* (SAR) images are from descending and ascending tracks. The detailed description of interferometric pairs selection criteria and processing steps are given in chapter III. The list of the SAR images acquired for this study is given in the Appendix 1.

I.3.6 Other data and software

Additionally we used the published and/or public data and software which are described within the thesis.

I. 4 Outline of this thesis

The thesis is organized in six chapters. Chapter I provides a general introduction to the research topic and thesis objectives. It also gives a description of used datasets. Chapter II describes the study area and an overview of previous ground deformation studies. Chapter III reviews SAR and InSAR theory and processing. Chapter IV presents an analysis of the spatial and temporal evolution of the anthropogenic deformation. Chapter V examines the coseismic ground deformation caused by the 24 May, 2006, Mw=5.4, Morelia Fault earthquake. Coseismic and postseismic groundwater level changes are also analyzed and modeled. Chapter VI contains the conclusions and recommendations derived from this study. A bibliography containing combined references for all the chapters is included at the end of the thesis.

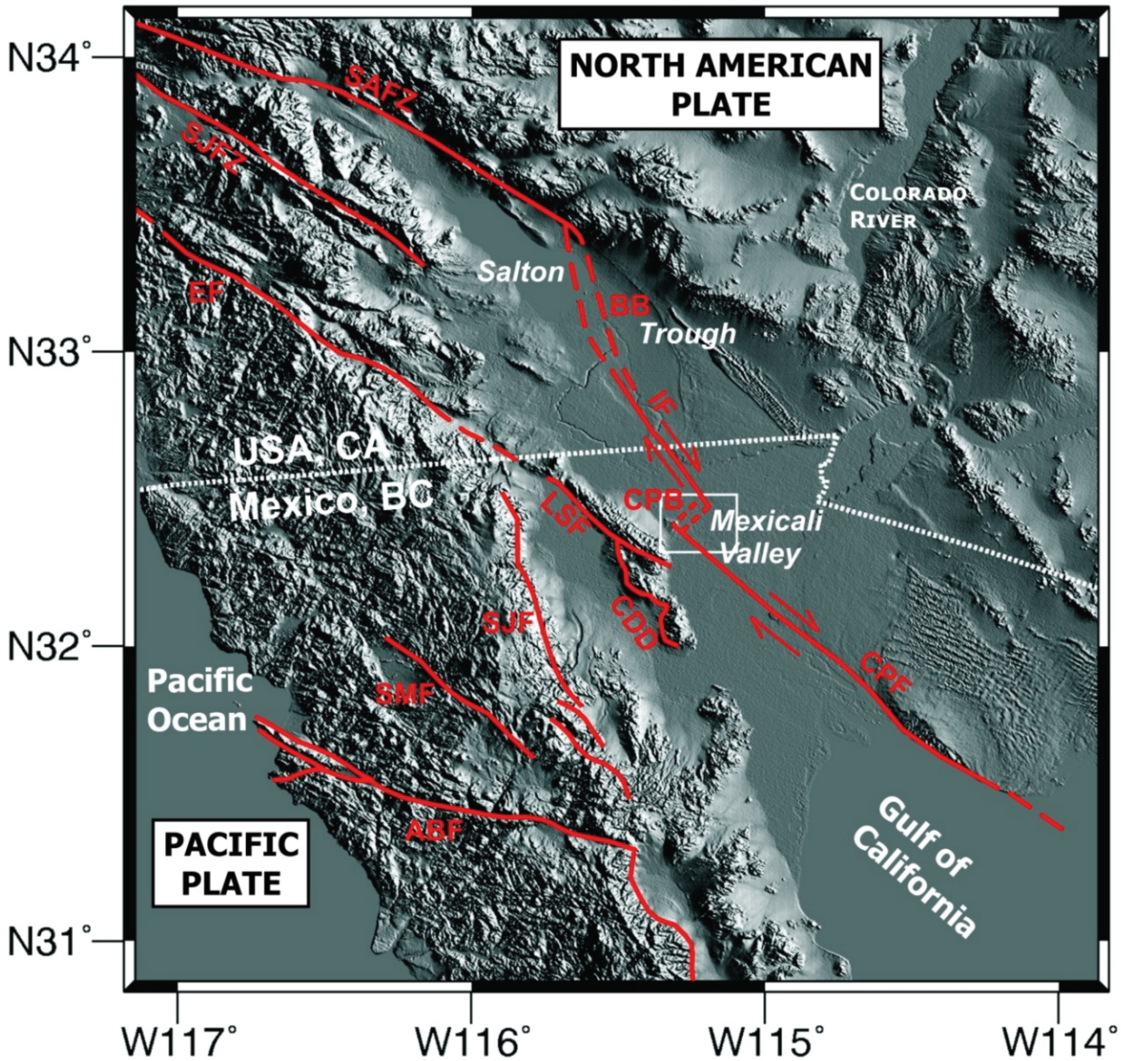

Figure 1: Map of northern Baja California, México and southern California, USA showing major active faults in red. White rectangle is the study region. Shuttle Radar Topography Mission Digital Elevation Model is used as background. Abbreviations: SAFZ=San Andreas fault zone; SJFZ=San Jacinto fault zone; EF=Elsinore fault; ABF=Agua Blanca fault zone; SMF=San Miguel fault; SJF=Sierra Juárez fault; LSF=Laguna Salada fault; CPF=Cerro Prieto fault; CPB=Cerro Prieto basin; IF=Imperial fault; BB=Brawley basin; CDD=Cañada David detachment. Modified from Suárez-Vidal et al. (2008).

Figura 1: Mapa de la parte Norte de Baja California, México, y sur del estado de California, EEUU, que muestra en rojo las fallas principales activas de la zona. El rectángulo blanco delimita el área de estudio. Modelo Digital de Elevación de la Misión Topográfica por Radar del Transbordador Espacial es usado como el fondo. Abreviaciones: SAFZ=zona de falla San Andrés; SJFZ=zona de falla San Jacinto; EF=falla Elsinore; ABF=zona de falla Agua Blanca; SMF=falla San Miguel; SJF=falla Sierra Juárez; LSF=falla Laguna Salada; CPF=falla Cerro Prieto; CPB=cuenca Cerro Prieto; IF=falla Imperial; BB=cuenca Brawley; CDD= detachment Cañada David. Modificado de Suárez-Vidal et al. (2008).

CHAPTER II

STUDY AREA

II.1 General information, tectonic and geologic setting

The Mexicali Valley is located in the northernmost part of the state of Baja California, Mexico, just south of the international border (Figure 1). It extends westward to the Cucapah Mountains and southward to the Colorado River delta and the northern tip of the Gulf of California. It is a relatively flat alluvial plain with altitude of ~10 m above the mean sea level. The only prominent topographic feature of the Mexicali Valley is the Cerro Prieto volcano, located near its western edge. This volcano is about 0.11 Ma old and was active intermittently until about 10,000 years ago (de Boer, 1980).

The Mexicali Valley is part of the Salton Trough tectonic province, which lies on the Pacific-North American plate boundary. The Salton Trough is a depression over 300 km long that extends northwest from the Gulf of California (Figure 1). The Salton Trough is a trans-tensional environment (Herzig and Jacobs, 1994) where a system of en-echelon dextral transform faults and pull-apart basins exists. Traditionally, the group of basins that connect the right-stepping dextral strike-slip transform faults located in the Salton Through have been interpreted as a series of incipient spreading centers (Nilsen and Sylvester, 1995), similar to the system of ocean ridges in the Gulf of California.

Transform faults in the Mexicali Valley include the right-lateral Cerro Prieto and Imperial faults, which run just east of Cerro Prieto volcano. The relative plate velocity along the Cerro Prieto and Imperial faults, determined by Bennett *et al.* (1996) using GPS measurements, is 4.2 and 3.5 cm/year of right-lateral motion, respectively. The sedimentary tensional zone that connects these faults is known as the Cerro Prieto pull-apart basin (Elders *et al.*, 1984; Lippmann *et al.*, 1984). Several normal faults, oblique to the major faults have been formed within the basin as consequence of the tensional stress regime imposed by the Cerro Prieto-Imperial fault system (Elders *et al.*, 1984; Lippmann *et al.*, 1984; González, 1999; Suárez-Vidal *et al.*, 2008). The Morelia fault defines the northern limit of Cerro Prieto basin, and the Saltillo fault defines its southern limit (Suárez-Vidal *et al.*, 2008). A schematic structural model of the Cerro Prieto basin is shown in Figure 2.

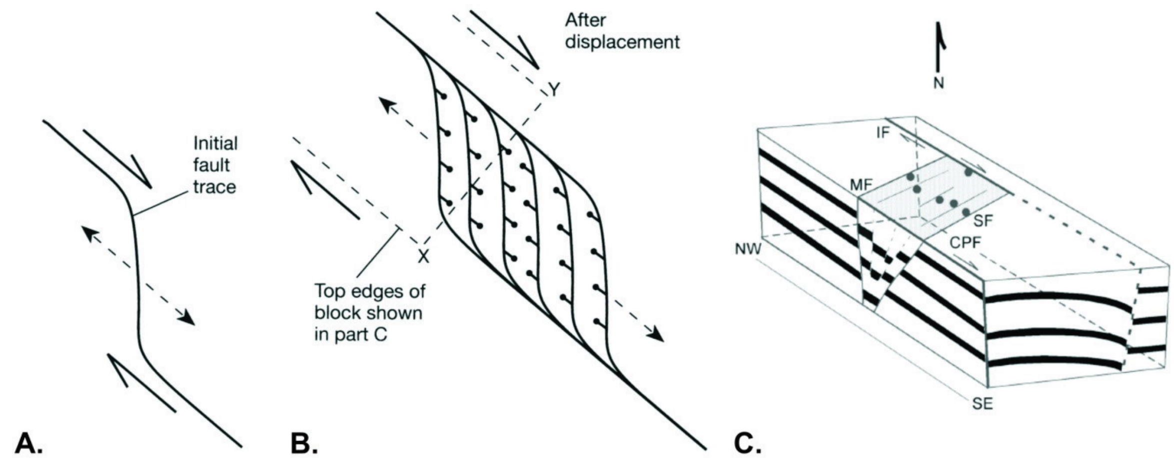

Figure 2: (A & B) Formation of a transtensional strike-slip duplex at an extensional (releasing) bend (from Twiss and Moores, 1992). C. Schematic structural model of the Cerro Prieto pull-apart basin based on ground observations and other data from Lira (2005). CPF=Cerro Prieto fault, IF=Imperial fault, MF=Morelia fault, SF=Saltillo fault (from Suárez-Vidal et al., 2008).

Figura 2: (A & B) Formación de un dúplex transtensional en un sistema de fallas transcurrentes (de Twiss y Moores, 1992). C. Modelo estructural esquemático de la Cuenca Cerro Prieto, basado en las observaciones de estructuras superficiales y datos de Lira (2005). CPF=falla Cerro Prieto, IF=falla Imperial, MF=falla Morelia, SF=falla Saltillo (de Suárez-Vidal et al., 2008).

The stratigraphy of the Salton Trough is characterized by vertical and lateral variations in lithofacies. The lithologic column at the Mexicali Valley, particularly at the Cerro Prieto basin, can be grossly divided into three main lithostratigraphic units A, B, and C (de la Peña and Puente, 1979) (Figure 3). Unit A is composed of unconsolidated and semiconsolidated continental deltaic and clastic sediments of undifferentiated Quaternary age, derived from the Colorado River and by westerly alluvial fans from the Cucapah Range. These sediments show repeated sequences of clays, silts, sands, and gravels. The bottom of this unit is formed of coffee-colored shale layers. The thickness of unit A is between 600m and 2300m. Unit B consists of consolidated continental deltaic sediments of Tertiary age. These sediments are composed of alternating shales, siltstones, and sandstones presenting lenticular bedding. The shales and siltstones are partially metamorphosed. The sandstone is fine grained, usually well-sorted, varying between graywackes and arkoses (de la Peña and Puente, 1979). Unit B is discordant with the granitic and metasedimentary Upper Cretaceous basement forming unit C. The Upper Cretaceous granite constitutes the Cucapah ranges. The basement has experienced tectonic uplift and subsidence. The depth of the basement at the Cerro Prieto basin varies from 3000m to 6000m, with basement depth increasing in the eastern direction (Figure 3).

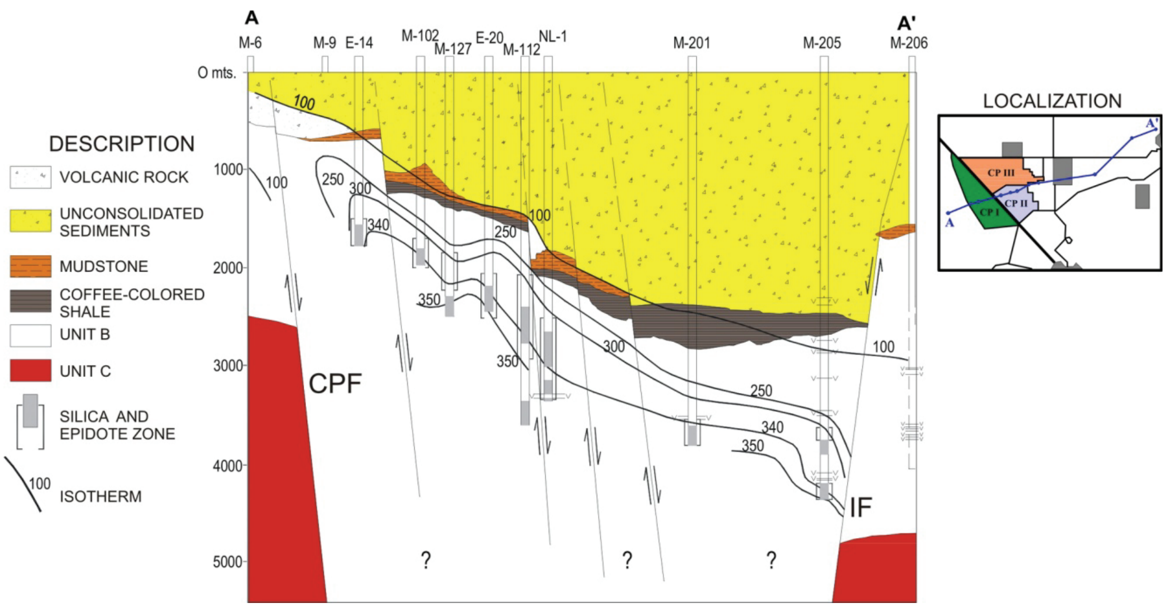

Figure 3: Lithological section in the study area (CFE, 1995). CPF=Cerro Prieto fault, IF=Imperial fault.

Figura 3: Sección litológica del área de estudio (CFE, 1995). CPF=falla Cerro Prieto, IF=falla Imperial.

II.2 Cerro Prieto Geothermal Field

Thick sedimentary sequences, extensional tectonics, high heat flow, active faults, and underground water flow from the Colorado River created the conditions for the formation of the geothermal reservoirs which forms the *Cerro Prieto Geothermal Field* (CPGF).

The CPGF is one of several high-temperature water-dominant geothermal fields within the Salton Trough. The CPGF went into power generation in March, 1973. The Cerro Prieto Geothermal plant is the first producing geothermal field in Latin America and the second largest in the world. The CPGF generates around 720 MW of electric power from reservoirs up to 3000 m deep.

The CPGF is a complex geological and hydrological system. The natural flow through this system is controlled by (1) deltaic layered sedimentary units of sands and shales, (Figure 3) (2) major faults, and (3) the regional hydrological pressure gradient (Lippmann and Bodvarsson, 1983). The geothermal fluid, with temperatures of 250-350 °C, is extracted from the gray shales of unit B and is isolated from the unconsolidated rock by layers of mudstone and brown shale which constitute the cap-rock (CFE, 2006). The geothermal reservoirs of the CPGF are bounded by the faults (Glowacka *et al.*, 1999).

The heat source for the hydrothermal system is probably located to the East, near Well NL-1 and Ejido Nuevo Leon, in an area where wells have drilled mafic and silicic dikes or sills. Such rocks are absent in the central and western parts of the field (Elders *et al.*, 1984). Elders *et al.* (1984) concluded that the heat source could be a funnel-shaped basalt intrusion, 4 km wide at the top, emplaced at a depth of 5 to 6 km, about 40,000 to 50,000 years ago, in the tensional zone of the pull-apart basin. Deep, hot hydrothermal brines recharge two deep reservoirs (labeled γ and β in Figure 4) through a high-angle normal fault (Fault H in Figure 4) (Lippmann *et al.*, 1991). The hot fluids flow through these reservoirs, and a thermal plume of hot brines, close to the boiling point, ascends through a gap in the shale layers into the shallowest reservoir (α). Then, fluids flow westward through the upper two reservoirs α and β. The uppermost reservoir α and the shallow aquifer are connected by another fault (L in Figure 4), and fluid discharges occur from the shallow aquifer located west and southwest of the field, forming hot springs and fumaroles at the surface. It is generally accepted that the geothermal reservoirs are also recharged by cold fresh water from shallow aquifers, located to the east, west, and south. This requires rapid downward flow (likely through faults) of cold, low salinity water that recharges the geothermal reservoirs (Halfman *et al.*, 1984; Lippmann *et al.*, 1991; Truesdell *et al.*, 1998). A schematic hydrological model of the CPGF is shown in Figure 4.

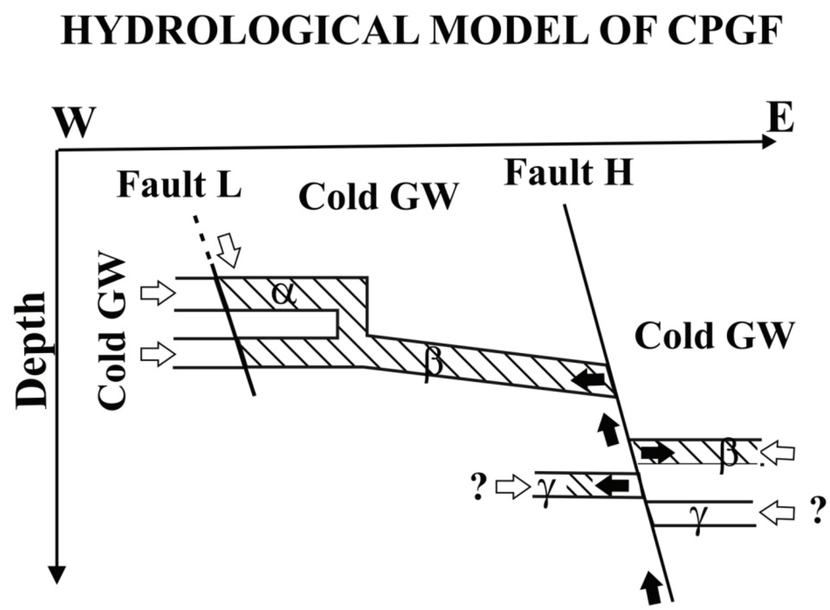

Figure 4: Hydrological model of the Cerro Prieto Geothermal Field (Lippmann et al., 1991). Black and white arrows indicate direction of hot and cold groundwater (GW) flow, respectively.

Figura 4: Modelo hidrológico del Campo Geotérmico Cerro Prieto (Lippmann et al., 1991). Las flechas negras y blancas indican la dirección del flujo de agua subterránea caliente y fría, respectivamente.

Ground subsidence is an expected consequence of the production of geothermal fluids. Fluid removal from subsurface reservoirs, in the form of geothermal water and brine, produces a compaction of the depleted formations, thus inducing anthropogenic land subsidence. Surface deformation has been observed even in deep reservoirs isolated from shallow groundwater (Massonnet *et al.*, 1997; Mossop and Segall, 1997; Fialko and Simons, 2000). Surface subsidence rates up to tens of centimeters per year have been measured across several major geothermal fields (e.g., Wairakei, New Zealand (Allis *et al.*, 1998), Geysers, USA (Mossop and Segall, 1997)). Ground subsidence also occurs in the CPGF and is likely due to fluid extraction combined with tectonic effects (Sarychikhina, 2003; Glowacka *et al.*, 1999, 2005). A detailed description of previous ground deformation studies in the CPGF and surrounding areas is given in the section II.4.

II.3 Seismicity of the area

The Mexicali Valley is a seismically active area because of its complex tectonic situation. Large-magnitude earthquakes ($M_L \geq 6$) occur along the main faults, at some distance from the zone of extensional deformation (Frez and González, 1991). Since the installation of the Southern California Seismic Network in 1932, six moderately-strong earthquakes have ruptured the Imperial and Cerro Prieto faults. Earthquakes with magnitude 6 or greater, associated with the Imperial fault, have occurred in May 1940 (El Centro earthquake, M_L 7.1), October 1979 (Imperial or Mexicali Valley earthquake, M_L 6.6), and December 2009 (M_L 6.0). As to the Cerro Prieto fault, two earthquakes occurred in December 1934 (M_L 6.5 and M_L 7.1) near the head of the Gulf of California (Fig. 4). Another M_L 6.1 occurred on June 1980, (Victoria earthquake). Albores *et al.* (1980) and Frez and González (1991) analyzed recorded seismicity in 1973-1987 period and found that the fault-plane solutions of earthquakes which occur along the NW-SE trending main faults generally show right-lateral, strike-slip faulting.

The area located near the northern end of the Cerro Prieto fault and the southern end of the Imperial Fault is known as the *Mexicali Seismic Zone* (MSZ), and is dominated by seismic swarms. However the earthquakes sequences of mainshock/aftershocks also occur. The magnitude of 5.5 can be considerate as upper limit of magnitude for earthquakes in the MSZ. In the Chapter V of this thesis the analysis of the surface displacement and groundwater level changes associated with the May 2006 earthquakes sequence and its main shock (Mw=5.4) source fault parameters modeling are presented.

The earthquakes of MSZ occur at depths that range mostly from 2 to 6 km (Majer *et al.*, 1980; Fabriol and Munguía, 1997) and their fault plane solutions generally show normal faulting (Fabriol and Munguía, 1997; Gonzalez *et al.*, 2001).

In addition to the natural occurring seismicity due to tectonic motion, it is possible that geothermal fluid exploitation in the CPGF could trigger seismicity. In theory, minor perturbations caused by human activity can have a destabilizing influence and trigger seismicity, as has been shown elsewhere (e.g. Segall, 1989; Nicholson and Wesson, 1992). Previous studies suggest that both extraction and injection could be responsible for triggering seismicity. Majer and McEvilly (1982) reported a significant increase of microseismic activity in the Cerro Prieto area, which they attributed to exploitation activities. A three month survey carried out at the beginning of 1993 detected important microseismic activity beneath the production/reinjection area (Dominguez *et al.*, 1997). Glowacka and Nava (1996) investigated the correlation between seismicity and fluid extraction, using data from USGS-Caltech catalogues for the years 1973-1991. According to a probabilistic analysis performed by these authors, the hypothesis that strong earthquakes could be triggered by a production increase cannot be rejected. Glowacka *et al.* (2005) modeled the Coulomb stress changes caused by fluid extraction (reservoir compaction) and showed that it could be large enough to trigger earthquakes. An analysis of seismicity recorded in the period of 1988 - 1996 (Glowacka *et al.*, 1997) showed the existence of a medium-term effect between injection and seismicity ($M>=3.0$). Comparison of the number of recorded earthquakes with the injection rates showed that during this period of 8 years, in 5 occasions seismicity increased 6-8 months after an increase in the injection rate.

II.4 Previous deformation analysis

The subsidence history in the Cerro Prieto region is well documented. From the analysis of the leveling surveys since 1977, Glowacka *et al.* (1999) noticed that, for the period 1977-1997, the subsidence rate at the center of the field increased after each fluid extraction increase. A more complete set of data, recorded during 1994-1997, allowed the estimation of the magnitude and shape of ground surface deformation in the CPGF and surrounding areas. The area of maximum subsidence rate, 12 cm/yr, coincided with the location of extraction wells. Another maximum of subsidence rate (9 cm/yr) was located to the east of the field, outside of extraction area. For this reason, the second maximum was interpreted as an area of fluid recharge. The observed subsidence rate is too high to be caused by tectonic activity only.

Subsidence in the study area was also studied using DInSAR by Carnec and Fabriol (1999) and Hanssen (2001) using ERS1/2 (*European Remote Sensing Satellites 1 and 2*) images acquired in the periods 1993 – 1997 and 1995-1997, respectively. Significant local subsidence up to 1.5 cm/moth was detected. Although agricultural activity in the area limited the investigation, interferometric monitoring revealed that the ground deformation is associated with the withdrawal of geothermal fluid and agreed with the leveling data.

Field mapping done since 1989 in the surrounding CPGF area shows that many of the subsidence-induced fractures, fissures, collapse features, small grabens, and vertical displacements are closely related to the known tectonic faults (Gonzalez *et al.*, 1998; Glowacka *et al.*, 1999; Suárez-Vidal *et al.*, 2008; Glowacka *et al.*, 2010). The subsidence is sufficient to affect infrastructure. The affected area is localized between the Cerro Prieto and the Morelia faults to the NW, and the Imperial and Saltillo faults to the SE, which limit the Cerro Prieto pull apart basin (Suárez-Vidal *et al.*, 2008).

Thus, the field observations show that the documented subsidence is bounded by the surface traces of the Cerro Prieto and Saltillo faults. Measurements using geotechnical instruments indicate that slip is accommodated mainly by aseismic creep along these faults. The vertical and horizontal components for the Saltillo fault are 6 cm/yr and 2 cm/yr, respectively. For the Cerro Prieto fault the vertical component is 3 cm/yr, with a horizontal component less than 1 cm (Glowacka *et al*. 1999, 2007, 2008). Analysis of the extension, amplitude, and temporal behavior of the slip on the Cerro Prieto and Saltillo fault suggest that these faults constitute a boundary of the actively subsiding area, and probably constitute a groundwater barrier.

To quantitatively evaluate the tectonic component of the subsidence recorded in the Mexicali Valley, Sarychikhina (2003) and Glowacka *et al.* (2005) modeled the elastic deformation caused in the pull-apart basin by the tectonic extension between the Imperial and Cerro Prieto strike-slip, right-lateral faults, using slip rates determined by GPS measurements (Bennett *et al.*, 1996). This model yielded a maximal tectonic subsidence rate of 0.45 cm/yr, over the CPGF. If compaction and isostasy are included, this rate could be as high as ~0.60 cm/yr. Thus, the estimated tectonic subsidence rate in the area of the CPGF accounts for only 4-5% of the total 12 cm/yr measured subsidence rate, leaving some 95% to anthropogenic causes. Independent estimates by Camacho Ibarra (2006), who estimates that 82-90 % of the observed subsidence in this region is anthropogenic, agree with this figure.

To evaluate the elastic deformation caused by fluid extraction in the CPGF, Mogi's model (Mogi, 1958) of a spherical hydrostatic pressure sources imbedded in an elastic half-space was used by Carnec and Fabriol (1999) and Hanssen (2001). Five sources were necessary to reproduce the fringe patterns observed on the interferograms (Carnec and Fabriol, 1999). The depth and location of three of the point sources are compatible with the location of the known reservoir.

Sarychikhina (2003) and Glowacka *et al.* (2005, 2010) used a mathematical model of rectangular tensional fracture (Yang and Davis, 1986) to model subsidence in the CPGF, arguing that this model is better for representing the geometry of geothermal reservoirs located in the tilted sedimentary layers and bounded by faults. The modeling was based on the hydrological model of the CPGF proposed by Lippmann *et al.* (1991) and was performed using the Coulomb 2.0 software; the model parameters were adjusted by the trial and error. The final model (Figure 5a) consists of five tensional rectangular fractures, which represent three geothermal reservoirs (α, β_1 and β_2), a shallow recharge aquifer that covers a wide zone between two major faults, and a local recharge aquifer located between the CPGF production zone and the Saltillo Fault (Sarychikhina, 2003; Glowacka *et al.*, 2005). Glowacka *et al.* (2010) added to the model a shear rectangular fracture representing a normal west-dipping Saltillo fault, in the eastern part of the study area, to improve the model and decrease the high residual values in this zone (Figure 5).

Both modeling, using Mogi's sources (Carnec and Fabriol, 1999; Hanssen, 2001) and rectangular tensional fractures (Sarychikhina, 2003; Glowacka *et al.*, 2005, 2010), provide the important information on the origin of the observed surface deformation. The location and depth of best-fit models bodies suggest that it can be related to geothermal fluid extraction.

Summarizing, analysis of leveling data and CPGF extraction history, and modeling of the tectonic and anthropogenic components of ground subsidence suggested that the current deformation rate is mainly related to the fluid extraction. The high deformation rate and spatial correlation between locations of the ground deformation maximum and extraction wells zone was confirmed by DInSAR method. However the field observations and geotechnical instruments data reveal that the geometry of the subsiding area is controlled by tectonic faults.

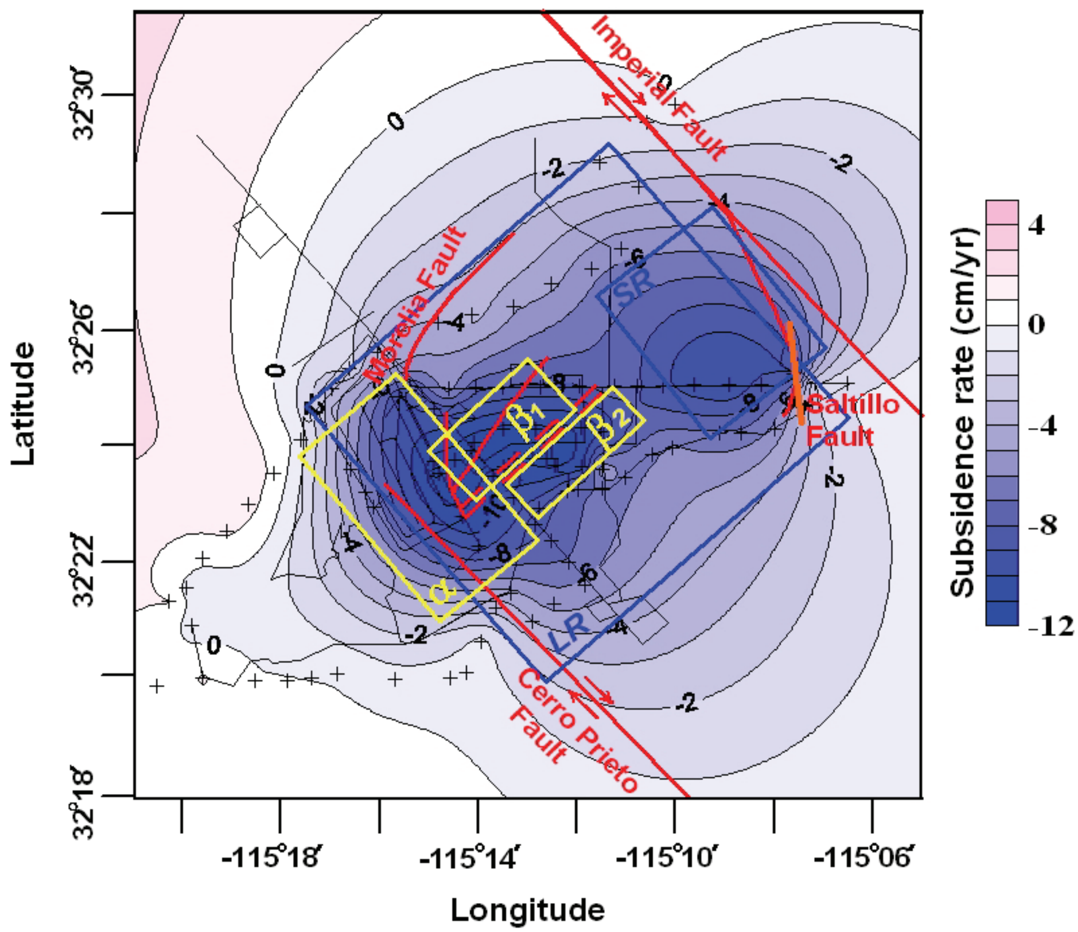

Figure 5: Modeling of the anthropogenic deformation in the Cerro Prieto Geothermal Field. Modified from Sarychikhina, 2003; Glowacka et al., 2005, 2010. Spatial distribution of the model's bodies is presented. Yellow rectangles are the surface projection of tensional rectangular fractures which correspond to the geothermal reservoirs. Blue rectangles are the surface projection of tensional rectangular fractures which correspond to aquifers of recharge. Orange line corresponds to the top of shear rectangular fracture representing the west-dipping normal Saltillo fault. The observed deformation is shown as background. Black crosses are the leveling benchmarks.

Figura 5: Modelación de la deformación antropogénica en el Campo Geotérmico Cerro Prieto. Modificado de Sarychikhina 2003, Glowacka et al., 2005, 2010. Distribución espacial de los cuerpos del modelo se presenta. Los rectángulos amarillos son la proyección sobre la superficie de las fracturas tensionales rectangulares que corresponden a los reservorios geotérmicos. Los rectángulos azules son la proyección sobre la superficie de las fracturas tensionales rectangulares que corresponden a los acuíferos de recarga. La línea anaranjada corresponde el techo de la falla de cizalla rectangular que representa la falla Saltillo que es una falla normal con el echado hacia oeste. La deformación observada está presentada como fondo. Las cruces negras son las bases de nivelación.

CHAPTER III

DINSAR BASIC THEORY AND PROCESSING

III.1 DInSAR basic theory

This first section of chapter III presents an overview of the basic theory required for understanding the DInSAR technique. Possible errors and technique limitations are also discussed. This section follows very closely several works that can be consulted to obtain more details on *Synthetic Aperture Radar* (SAR) theory and radar interferometry, and their applications. The works are those of Massonnet and Rabaute (1993), Gens and Vangenderen (1996), Bamler and Hartl (1998), Henderson and Lewis (1998), Massonnet and Feigl (1998), Price and Sandwell (1998), Bamler (2000), Bürgmann *et al.* (2000), Rosen *et al.*(2000) and Hanssen (2001).

III.1.1 Remote sensing in Earth science. Brief background of Radar.

Remote sensing is used to monitor or measure phenomena found in the Earth's lithosphere, biosphere, hydrosphere, and atmosphere. Most sensing devices record information about an object by measuring the emission or reflection of electromagnetic radiation. Remote sensing systems can be classified as either active or passive, according to whether they provide their own energy source for illumination or not. Radar, an acronym for *radio detection and ranging*, is an active sensor which involves the transmission and reception of microwave electromagnetic radiation, with frequencies roughly in the range of 10^8-10^{11} Hz and corresponding wavelengths of order the 1-1000 mm (Figure 6).

Imaging radars create a spatial image of targets. These radars generally emit wavelengths on the order of a few centimeters, which will penetrate clouds and precipitation. Water clouds have significant effect only on radars operating below 2 cm in wavelength; the effects of rain are relatively inconsequential at wavelengths above 4 cm. Thus, in theory, imaging radars can operate in day or night day and nearly all-weather operation (Figure 6).

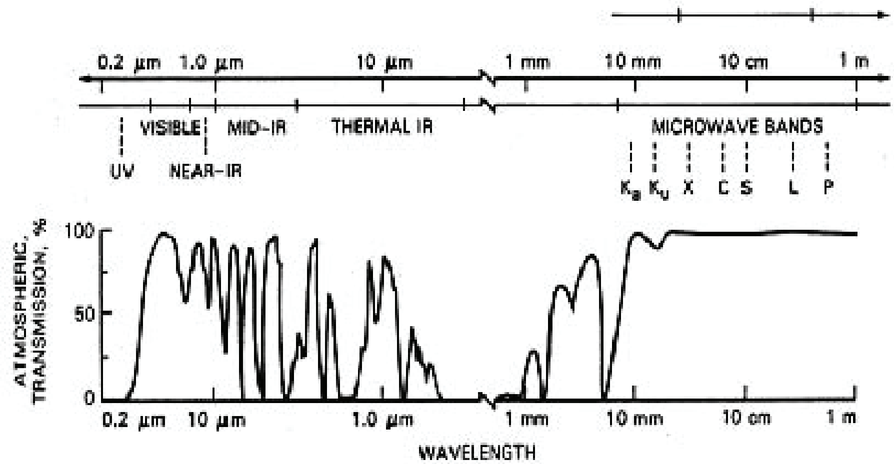

Figure 6: The electromagnetic (EM) spectrum, showing the bands used in remote sensing (upper graph). The atmospheric transmission of the EM spectrum is shown in the lower graph. Note that the operating areas for imaging radars are located in parts of the spectrum where atmospheric transmission is high (from Henderson and Lewis (1998)).

Figura 6: El espectro electromagnético (EM), mostrando las bandas usadas en la percepción remota (grafica superior). La transmisividad del espectro (EM) se muestra en la grafica inferior. Nótese que la zona de operación de los radares de imagen se localiza en la porción del espectro con alta transmisividad (de Henderson and Lewis (1998)).

A particular imaging radar uses a single wavelength within the specific segment of the microwave portion of the electromagnetic spectrum, known as a band (Figure 6). Satellite imaging radars typically use the X- (~2.5 – 4 cm;), C- (4 -8 cm), or L- (15-30 cm) bands. Historically, C-band is most commonly used (ERS-1, ERS-2, Envisat, RADARSAT-1 and RADARSAT-2) but L-band (SEASAT, JERS-1 and ALOS) and recently, X-band (TERRA-SAR) have also been used in publicly available SAR satellites. Each wavelength is reflected best by objects approximately the same size as the radar wavelength. X-band radar reflects off objects that are a few cm in size and therefore will be affected by vegetation and trees. L-band radars tend to penetrate all but the largest trees. The electrical properties of the ground surface, which usually vary with moisture content, will also affect the radar return.

Radar signals may also be polarized horizontally or vertically, which refers to the direction of vibration of the electromagnetic waves but in this work we use only vertically polarized data. As the radar "looks" to one side rather than vertically down, shadowing and layover, which distort the image, will occur in areas with topographic gradients.

Imaging radars can be divided into two main categories, depending on the imaging technique used: *Real Aperture Radar* (RAR) also called *Side Looking Airborne Radar* (SLAR) and the *Synthetic Aperture Radar* (SAR). For both radar types the side-looking imaging geometry applies.

III.1.2 Radar imaging geometry and spatial resolution

The geometry of an imaging radar is presented in Figure 7, which shows a radar platform traveling forward in the flight direction with the nadir directly beneath them.

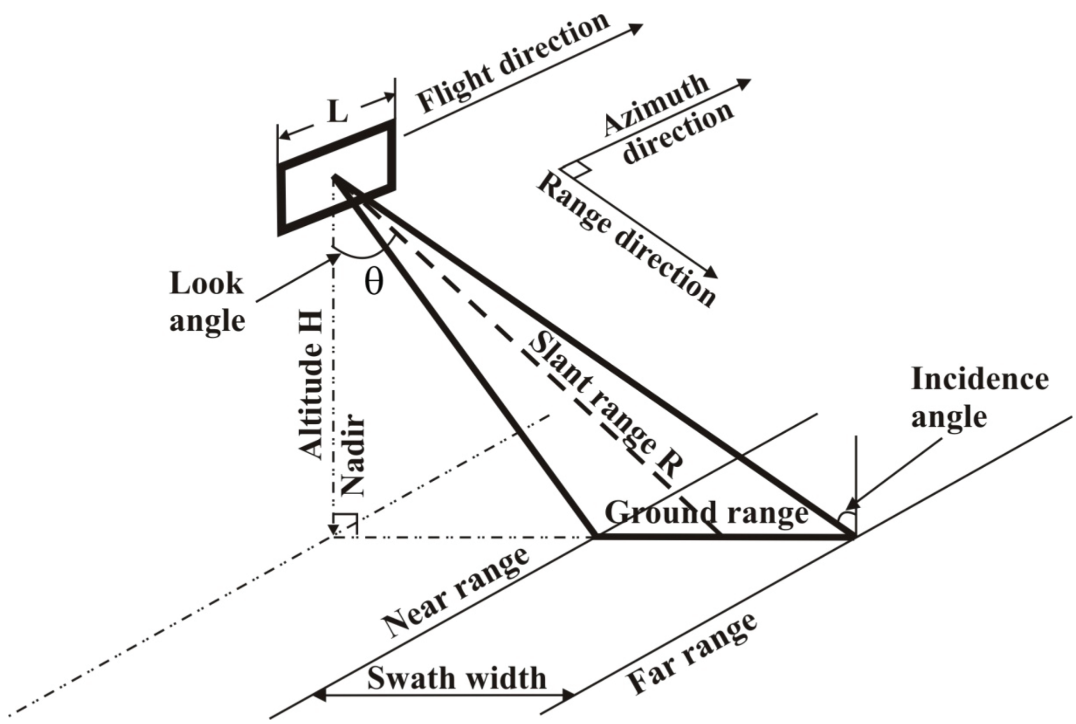

Figure 7: Radar imaging geometry.

Figura 7: Geometría del Radar.

The radar instrument emits a series of electromagnetic pulses obliquely at right angle to the flight direction illuminating a *swath* located some distance away the nadir. *Range* refers to the across-track dimension perpendicular to the flight direction, while *azimuth* refers to the along-track dimension parallel to the flight direction. The portion of the image swath closest to the nadir track of the radar platform is called the *near range*, whereas the portion of the swath farthest from the nadir is called the *far range*. The angle between the direction the antenna is pointing at and the nadir line, is the *look angle*. This angle varies across the image swath and is smaller in the near range than in the far range. The *incidence angle* is the angle between the axis of the radar beam and the normal to the local topography. These two angles are sometimes used synonymously, but that is only valid for a simplified geometry in which the Earth's curvature and the local topography are neglected. The radial *line of sight* (LOS) distance between the radar and each target on the surface is the *slant range distance*. The *ground range* distance is the true horizontal distance along the ground, corresponding to each point measured in the slant range. Radar data collected in the slant range domain are projected onto the ground range plane when these data are geocoded.

The radar image is composed of pixels. Each pixel denotes the information corresponding to a ground resolution cell. The dimensions of the ground resolution are defined by the ground range resolution and the azimuth resolution of a radar system.

Range resolution is directly related to the pulse length of the transmitted radar signal. The shorter the pulse length, the finer the range resolution. Pulse length, the physical length of the microwave signal, is given by the product of the speed of light, c, and the duration of transmission, τ. Because the radar signal must travel to the target and back to the sensor, the pulse length is divided by 2 to determine the slant range resolution ($c\tau/2$). To accommodate the different geometries of slant and ground range, the pulse length is divided by the sine of the look angle, θ. The resulting equation for ground range resolution, Δ_G, is:

$$\Delta_G = \frac{c\tau}{2\sin\theta}. \tag{1}$$

According to the equation (1), a better across-track resolution is acquired from a shorter pulse duration time τ . However, if the duration of the pulse is too short, it will not have enough energy to produce a strong echo. The design of the instrument, therefore, is a compromise between a sufficient *Signal-to-Noise Ratio* (SNR) and high resolution. It will be an ideal situation if we could achieve reasonable resolution using a longer pulse with large enough SNR. This is achieved by using a chirp pulse, in which the frequency varies with time. By cross-correlating the recorded echoes with the original chirp, the resulting wavelets will have improved range resolution. This is referred to as pulse compression or matched filtering. The improvement in range resolution is (Curlander and McDonough, 1991):

$$\Delta_G = \frac{c}{2B_W \sin\theta}, \tag{2}$$

where B_W is the frequency bandwidth of the transmitted pulse. According to the inverse relationship between range resolution and bandwidth, increasing resolution can be achieved by increasing the pulse bandwidth. For the ERS and Envisat systems, the nominal pulse length is 37.1 μsec and the nominal range bandwidth is 15.55 MHz. With this system configuration the slant resolution without matched filter techniques is about 5.6 km in length (according to equation (1)). Through use of a matched filter, its resolution can be improved to about 10 m and 25 m in the slant range and ground range, respectively. SLAR and SAR use the same method for improving range resolution.

The azimuth resolution is limited by the azimuth antenna footprint size. Basic antenna theory states that the resolution of the signal detected by an antenna, Δ_A, is inversely proportional to the length, L, of the antenna:

$$\Delta_A = \frac{\lambda}{L} R, \tag{3}$$

where λ is the wavelength of the imaging and R is the range distance. Nominal values for the C-band Envisat and ERS systems wavelength and antenna length are 5.6 cm and 10 m, respectively. Through equation (3), we can find that these satellites with slant range R = 800 km can have an along-track resolution of 4.5 km length. This means that objects in the

4.5 km range are expressed as one pixel in the image. Better resolution is achievable through a larger antenna, but often it is impractical to carry an extremely long antenna such as 500 m or even a couple of kilometers long. Real Aperture Radars do not provide fine resolution from orbital altitudes, although they have been built and operated successfully (for example COSMOS 1500, a spacecraft built by the former Soviet Union). For such radars, azimuth resolution can be improved only by longer antennas or shorter wavelengths. The use of shorter wavelengths generally leads to higher cloud and atmospheric attenuation, reducing the all-weather capability of imaging radars. Synthetic Aperture Radar uses signal processing to synthesize an aperture that is hundreds of times longer than the actual antenna by operating on a sequence of signals recorded in the system memory (see following subsection for details).

III.1.3 SAR Synthetic Aperture

To increase the image resolution in the azimuth direction, the SAR system uses spacecraft (or aircraft) movement and processing to simulate a larger sensor size. A single antenna moving along the flight line acquires the data sequentially and the effect is similar to using an array of antennas (Figure 8). Each ground target is illuminated several times from different locations generating numerous echoes that are recorded coherently (i.e., amplitude and phase as a function of time). Due to the motion of the radar platform, the frequency of the echoes varies due to the Doppler phenomenon. Echoes reflected from terrain in front of the moving sensor are shifted to higher frequencies than those reflected from behind are shifted lower. The amount of shift depends on the relative motion of the target with respect to the satellite which in turn depends on the location of the target. The variation in frequency is unique for each point in the azimuth direction. If the satellite motion is known precisely enough, another matched filter can be constructed that focuses the image in the azimuth direction. A higher along-track resolution is achieved independently of the distance between sensor and target by a small antenna (Elachi, 1988). The resolution can be expressed as:

$$\Delta_A = \frac{L}{2}. \tag{4}$$

The synthetic aperture technique improves the azimuth resolution for ERS and Envisat systems from 4.5 km to 5 m. After combining the results of the range and azimuth processing, each radar pixel will correspond to a specific ground location. Note that the azimuth resolution (~5 m for Envisat) is much better than the range resolution (~25 m).

The Envisat SAR data used in this thesis were pre-processed (focused) to the *Single Look Complex* (SLC) format by the ESA Processing and Archiving Centre. This SLC image is composed of many dots (pixels). For each pixel the amplitude and phase of the backscattered signal are preserved. In general, the amplitude image has been more commonly used. The phase in a single image is random but it is also possible to use the phase differences between two (or more) images to extract information. In this thesis, phase is used to measure ground surface motions. Such information makes the interferometry process possible and is described in the following subsection.

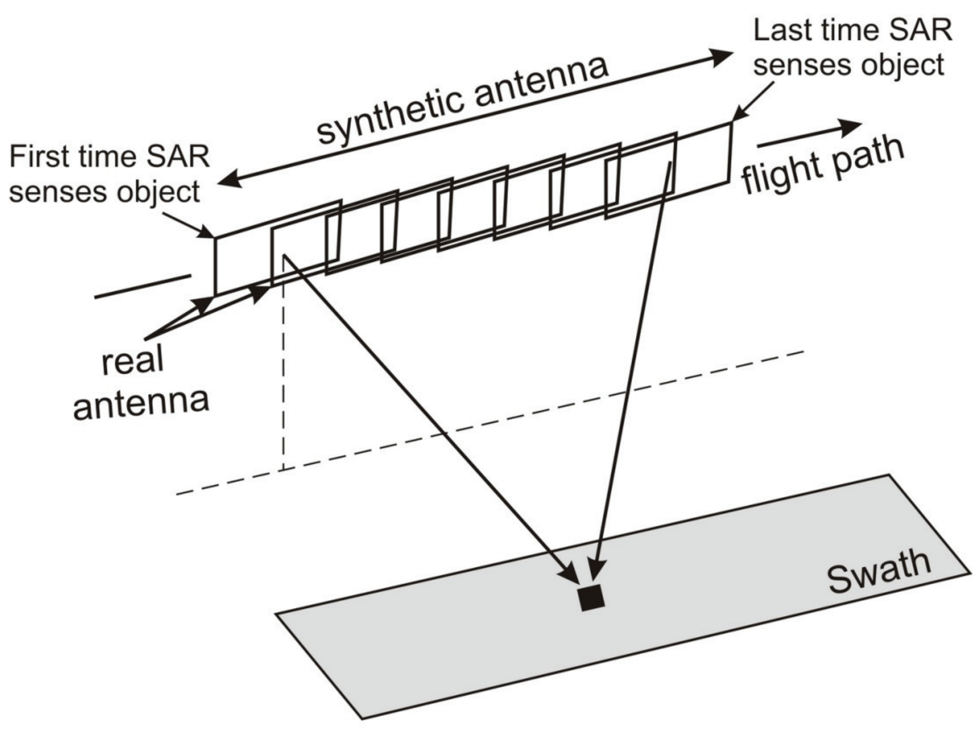

Figure 8: Schematic illustration of forming a synthetic aperture.

Figura 8: Ilustración esquemática de la formación de la apertura sintética.

III.1.4 SAR Interferometry (InSAR)

A SAR system produces images of the ground that comprise a nominally regular grid of complex values $g(x, y)$:

$$g(x, y) = u(x, y) + iv(x, y), \tag{5}$$

where $u(x, y)$ and $v(x, y)$ are the real and imaginary parts of the complex number. Such complex numbers can be represented in terms of amplitude $|g(x, y)|$ and phase $\phi(x, y)$:

$$g(x, y) = |g(x, y)| e^{i\phi(x, y)}, \tag{6}$$

where amplitude is defined as:

$$|g(x, y)| = \sqrt{u^2(x, y) + v^2(x, y)}, \tag{7}$$

and phase:

$$\phi(x, y) = \arctan \frac{v(x, y)}{u(x, y)}, \text{ when: } u(x, y) \neq 0. \tag{8}$$

To perform radar interferometry two SAR images are needed. SAR interferometry can be considered to be of two main types:

a) Single-pass interferometry, in which two or more antennas simultaneously image the same ground scene. The most prominent application of single-pass interferometry was made by the *Shuttle Radar Topography Mission* (SRTM) in 2000 to produce the global, 30 m spatial sampling (3-arsec), *Digital Elevation Model* (DEM). This method is not applicable to the monitoring of displacement at different times.

b) Repeat-pass interferometry, where separate passes over the same target area are used to form an interferogram (Figure 8). This type of SAR interferometry is used in this thesis for surface deformation monitoring.

In this thesis, the image acquired in the first pass is called the *master* (M) and the image acquired in the second pass is called the *slave* (S). The complex notation of the SAR images can be expressed as:

$$g_M(x, y) = |g_M(x, y)| e^{i\phi_M(x, y)}, \tag{9}$$

where:

$$\phi_M = \frac{4\pi R_M(x,y)}{\lambda} + \phi_{scat,M} + \phi_{prop,M} + \phi_{noise,M}, \qquad (10)$$

$$g_S(x,y) = \left|g_S(x,y)\right| e^{i\phi_S(x,y)}, \qquad (11)$$

where:

$$\phi_S = \frac{4\pi R_S(x,y)}{\lambda} + \phi_{scat,S} + \phi_{prop,S} + \phi_{noise,S}, \qquad (12)$$

where $\left|g_M(x,y)\right|$ and $\left|g_S(x,y)\right|$ are the complex terrain reflectivities, R_M and R_S are the ranges from the sensors to point $g(x,y)$ on the ground, λ is the wavelength, $\phi_{scat,M}$ and $\phi_{scat,S}$ represent scattering phases, $\phi_{prop,M}$ and $\phi_{prop,S}$ represent atmospheric propagation delays, and $\phi_{noise,M}$ and $\phi_{noise,S}$ are phase shifts due to the noise within a resolution cell in the two images. In these equations, the phase in the exponential is defined as modulo 2π.

After aligning and resampling the slave image to corresponding locations in the master grid (for details see following section III.2), the phase difference between the two images is determined by multiplication of the complex value of the master $g_M(x,y)$ by the complex conjugate of the slave $g_S^*(x,y)$:

$$g_M(x,y)g_S^*(x,y) \cong \left|g_M(x,y)\right|\left|g_S(x,y)\right| e^{i(\phi_M - \phi_S)}. \qquad (13)$$

This product of such multiplication is a complex interferogram. The phase of the complex interferogram represents the phase difference (modulo 2π) in slant range between two SAR acquisitions while the amplitude image contains the useful information on the SNR of the observed phase.

III.1.5 InSAR acquisition geometry and DInSAR technique

Figure 9 shows the geometry of repeat-pass interferometry. In repeat-pass InSAR, the spatial separation between two repeat orbits is known as the *baseline* which is the distance between the satellite positions at image acquisition. The baseline is often expressed in terms of perpendicular baseline $B_{\perp}$ and parallel baseline $B_{//}$ to the reference (master) look direction. In Figure 8, two satellite orbit positions are physically separated by a baseline which has length B and angle α with respect to the horizontal. Orbit 1 is at height H above some reference datum, generally the *World Geodetic System 1984* (WGS84) ellipsoid in the case of satellite interferometry. Angle θ is the look angle. The range from orbit 1 to a point in the ground at height *h* above the reference datum is $R_M = R$, and the range from orbit 2 to the same point is $R_S = R + \Delta R$.

If the scattering and atmospheric characteristics are equal for both acquisitions ($\phi_{scat,M} = \phi_{scat,S}$; $\phi_{prop,M} = \phi_{prop,S}$), and if noise can be neglected[1] ($\phi_{noise,M} = 0$; $\phi_{noise,S} = 0$), then the interferometric phase ϕ can be written as:

$$\phi = \phi_M - \phi_S = \frac{4\pi(R_M - R_S)}{\lambda} = \frac{4\pi\Delta R}{\lambda}. \tag{14}$$

For repeat-pass InSAR, due to the difference in the acquisition geometry, the interferometric phase will be proportional to the sum of a curved Earth, ΔR_e, a topographic, ΔR_t, and a deformation, ΔR_d, contribution to the range change:

$$\phi = \frac{4\pi}{\lambda}(\Delta R_e + \Delta R_t + \Delta R_d). \tag{15}$$

Therefore, the surface deformation can be measured from an interferogram if the other terms in equation (15) can be determined and removed. The curved Earth and topographic contributions to the range change are described by the equations:

$$\Delta R_e \approx B_{//}, \tag{16}$$

$$\Delta R_t \approx \frac{hB_{\perp}}{R\sin\theta}, \tag{17}$$

[1] I will refer in more detail to decorrelation and noise issues, in the next subsection.

where $B_{//} \approx B\sin(\theta-\alpha)$ and $B_{\perp} \approx B\cos(\theta-\alpha)$. The detailed mathematical and technical explanations of these resulting equations can be found in a number of papers and books on the theory and applications of InSAR given in the beginning of this chapter.

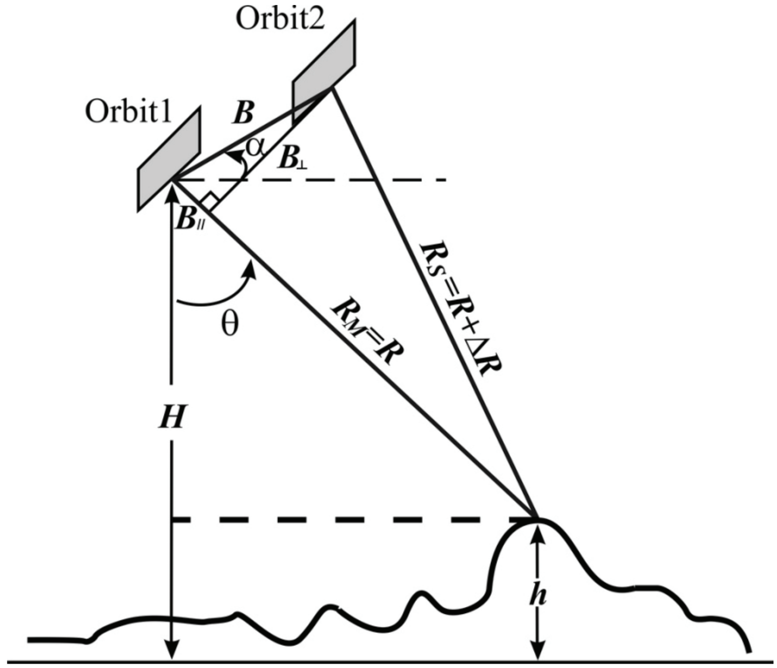

Figure 9: Geometry of repeat-pass interferometry. Two satellite orbit positions are physically separated by a baseline that has length B and angle α with respect to the horizontal. Orbit 1 is at height H above some reference datum. The angle θ is the look angle. The range from Orbit 1 position to a point in the ground at height h above the reference datum is $R_M = R$, and the range from Orbit 2 to the same point is $R_S = R + \Delta R$. $B_\perp$ and $B_{//}$ are, the perpendicular and parallel components, respectively, of the baseline to the reference (master) look direction.

Figura 9: Geometría de la interferometría del paso repetido. Las posiciones de dos orbitas del satélite están físicamente separadas por una línea de base de longitud B y ángulo α con respeto a la horizontal. La órbita 1 está a la altitud H sobre un nivel de referencia. El ángulo θ es el ángulo de vista del radar. El rango entre la posición en la Órbita 1 y un punto en la superficie a altitud h sobre un nivel de referencia es $R_M = R$, y el rango de la posición en la Órbita 2 al mismo punto es $R_M = R$. $B_\perp$ y $B_{//}$ son, respectivamente, las componente perpendicular y paralela de la línea de base con referencia a la dirección de vista del master (Orbita 1).

The baseline can be estimated by using precise orbits. For *European Space Agency* (ESA) SAR data, the precise orbit products provided by ESA are usually used as the initial parameters when calculating the orbital baseline (Scharroo and Visser, 1998). Depending on the quality of the orbit data, it may be necessary to re-estimate the baseline after initial processing of the interferogram.

The topographic effect can be simulated using *Digital Elevation Model* (DEM), or estimated from an independent interferogram and then subtracted from the original interferogram. The separation of phase contributions due to topography and displacement, in order to get the deformation field, is the basic idea of the *Differential SAR Interferometry* (DInSAR) approach.

The phase differences that remain as fringes in the differential interferogram are a result of range changes of any point on the ground displaced from one interferogram to the next. In the differential interferogram, each fringe is directly related to the radar wavelength and represents a displacement relative to the satellite of only half the wavelength; thus, the sensitivity of the interferometric phase to surface deformation is very high. In the case of a C-band SAR (ERS, Envisat, Radarsat) a 2π displacement phase corresponds to only 2.8 cm displacement along the LOS direction. Since the measured phases in the differential interferogram are wrapped modulo 2π, the ground displacement map is obtained by phase unwrapping of the interferogram. Phase unwrapping is used to estimate unambiguous differential interferometric phases and is therefore an important required step (see section III. 2).

III.1.6 Limits for DInSAR

It is theoretically possible to measure the surface deformation using DInSAR technique with sub-centimetric (C-band radars) or centimetric (L-band radars) accuracy. But in practice, several factors can degrade the quality of interferograms and thus reduce the accuracy of ground displacements inferred from them, limiting the applicability of the technique. The four main factors that affect the quality of interferograms are temporal decorrelation, spatial decorrelation, orbital errors, and atmospheric artifacts.

The preferred criterion to measure quality of the interferogram is the absolute value of the complex correlation coefficient, the so-called *coherence*. To successfully generate an interferogram, the phase between two images must be well correlated. The coherence is a measure of phase correlation (or phase reliability) between two complex SAR images g_M and g_S, and is defined as

$$\gamma = \left| \frac{\sum g_M g_S{}^*}{\sqrt{\sum |g_M(x,y)|^2 \sum |g_S(x,y)|^2}} \right|. \tag{18}$$

The summation is performed over the number of pixels. The coherence lies in the range $0 \le \gamma \le 1$; a value of zero indicates complete incoherence and the interferogram contains no useful information, whereas a value of one indicates complete coherence and the interferogram contains no noise. A coherence value can be assigned to each pixel of the interferogram to generate a quality map, often called a coherence map.

Temporal changes in the physical properties of the targets lead to decorrelation between the phases of the two images. This phenomenon is referred to as temporal decorrelation. Some of the main sources of decorrelation are the random displacements of the targets due to erosion, vegetation growth, cultivation, and changes in the water content of the targets. Decorrelation can occur in time spans ranging from seconds to years, depending on the surface characteristics. Correlation can be preserved for a long time (several years) in regions with bare rock, sparse vegetation, arid climate and urban settlements. Consequently, most InSAR and DInSAR studies to date have focused on areas that are dry and sparsely vegetated. Since temporal decorrelation is due to changes of the surface mainly at the scale of the radar wavelength, temporal decorrelation is highly dependent on the operating frequency of the radar (Zebker and Villasenor, 1992). InSAR data acquired using longer wavelengths, for example the L-band, exhibits lower temporal decorrelation as it penetrates most vegetation (Strozzi *et al.*, 2003).

Decorrelation also results from variations in imaging geometry. If the perpendicular baseline between the spacecraft position at the two times at which the images are acquired is non-zero, the difference in incidence angle alters the coherent sum of wavelets from the many small scattering elements within a resolution cell, so that measurements do not repeat exactly. This phenomenon, referred to as spatial decorrelation (Zebker and Villasenor, 1992), increases as the baseline increases. The required repeat orbit tolerance is estimated as the maximum normal component of the baseline, known also as *critical baseline* B_C, which depends on the radar wavelength λ, the sensor-target distance R, the ground range resolution Δ_G, and the look angle θ:

$$B_C = \frac{\lambda R}{2\Delta_G \cos^2 \theta}. \tag{19}$$

Following this argument, standard interferometry cannot be carried out if $B_\perp \geq B_C$. For Envisat the critical baseline is around 1300 m. However, in practice, baselines significantly shorter than the critical baseline are required (up to about 25% of the critical baseline are preferred). In the Envisat case, such an optimum baseline is about 300–400 m. This "short baseline requirement" significantly reduces the availability of adequate image pairs significantly.

The orbital and topographic errors are the other two factors that affect the differential interferometric phase and could create confusion in its interpretation. For SAR differential interferometry, an error in the baseline estimate can create a phase trend referred to as orbital fringes, which usually have a constant gradient in a certain direction, and thus they can be fitted and removed. In order to remove orbital fringes completely, an orbital accuracy on the order of 1 mm is required, which is far below the current precision orbit vectors having a *Root Mean Square* (RMS) accuracy on the order of 10 cm (Scharroo and Visser, 1998).

The influence of topographic error (DEM error) on an interferometric pair depends on the sensitivity of interferometric phase to the topography, measured by *ambiguity height* h_A, which is the topographic height required to produce one phase cycle or one fringe, and can be obtained from equation (17):

$$h_A = \left| \frac{\lambda R \sin\theta}{2B_\perp} \right|. \tag{20}$$

Topographic effects can be ignored for image pairs whose h_A values are much higher than the estimated vertical accuracy of DEM. Longer baselines are more sensitive to topographic error.

Another important source of error in SAR differential interferograms is due to variations in the atmosphere. This may be caused by variations in water vapor in the troposphere or by variations in electron density in the ionosphere. A relative delay in the radar signal will occur if atmospheric conditions, such as pressure, temperature and, principally, water vapor, are not the same at the time of the acquisition of the two radar images. The delay, in turn, leads to phase shifts, atmospheric artifacts that contaminate the interferogram. Variation in tropospheric water vapor may occur spatially or vertically. Spatial variations can cause up to two fringes in amplitude. Vertical variations due to a layered atmosphere will cause fringes associated with topographic elevation. Ionopheric effects are more significant for longer wavelengths (e.g. L band).

The presence of atmospheric effects is a serious problem because they hinder the capability of the DInSAR technique to resolve accurately ground deformation and may even completely obscure its signal (see Goldstein, 1995; Zebker *et al.*, 1997; Hanssen, 1998; Hanssen, 2001). Moreover, the atmospheric phase component is hard to calculate and the coherence maps cannot bring to light its presence. When dealing with only two SAR images, the identification of atmospheric artifacts and their quantification is an impossible task without using external information (e.g. GPS or satellite sensors as MERIS (*Medium Resolution Imaging Spectrometer*), MeteoSat). In some cases (e.g. high deformation rates or peculiar spatial patterns of deformation) the impact of the atmosphere on the differential interferometric phase can be neglected. In cases when a set of images is available, comparison of multiple interferograms can help to identify images that are heavily affected by atmospheric disturbances, in an effort to isolate these images. It is also possible to minimize the atmospheric effects by stacking multiple interferograms to boost the deformation signal and reduce the noise. The basic idea of interferograms stacking is to combine multiple observations into a single result. The main assumption is that the deformation phase is highly correlated while the error terms are uncorrelated between independent pairs.

In areas with substantial topographic relief variation in water vapor with height will cause a correlation of phase with topography. This can be estimated and removed by plotting phase change and topography.

Stacking of multiple interferograms is also widely used when reasonable coherency levels can only be obtained over short time periods. Several short-time period temporally contiguous interferograms can be summed to produce a pseudo-interferogram over a longer period. This summation enables low magnitude displacements to be monitored over longer periods, where no single coherent interferogram exists (see capture IV). The disadvantages of stacking are the degradation of the temporal resolution of DInSAR measurements, and that the method works best for long continuous signals.

III.1.7 Accuracy estimation for DInSAR data

As was explain above, the accuracy of DInSAR results is a complex function of many factors. The accuracy of a displacement measured by a single picture element of an interferogram is essentially meaningless, because the ability to measure ground movements with DInSAR depends less on the dispersion of random elements than it does on the recognition of fringes. Thus, in practical terms, calculating the formal uncertainty of displacements derived from interferograms is difficult (Dzurisin *et al.*, 1999). There is no straightforward method to estimate accuracy for the DInSAR data. The analysis of available literature allowed defining the more used strategies. The simple arbitrarily assumption of DInSAR data uncertainties could be used. For C-band radars, the generally accepted accuracy of DInSAR surface change measurement is ~1cm**,** under favorable surface and atmospheric conditions**.** However, the uncertainties of up to about 100 % of radar wavelength could be assumed (Strozzi *et al.*, 2001; Nishimura *et al.*, 2006). An estimate of the uncertainty can be made by comparing independent interferograms formed from different pairs of images, and supposing the same deformation pattern and magnitude is occurred for different periods spanned by the interferograms (Wicks *et al.*, 2001). The accuracy of DInSAR measurements could be evaluated by their comparison with measurements from ground based technique (GPS and/or leveling) (Alipour *et al.*, 2008; Hung *et al.*, 2010). The uncertainty of DInSAR data could also be estimated from the residuals in the non-moving areas (Kenyi and Kaufmann, 2001; Papanikolaou *et al.*, 2010).

In this thesis we used the residual estimation in non-moving area to determine the single interferogrm accuracy and the equation presesented in Strozzi *et al.* (2001) to evaluated the accuracy of DInSAR stacking data (see chapter IV).

III.1.8 Restrictions of DInSAR application for surface deformation study

DInSAR is used in a number of applications. Important results have been obtained in different branches of geophysics: ice and glacier dynamics (Goldstein *et al.*, 1993; Kwok and Fahnestock, 1996); earthquakes (Massonnet and Rabaute, 1993; Stramondo *et al.*, 1999; Fielding *et al.*, 2005); volcanoes (Massonnet *et al.*, 1995; Sigmundsson *et al.*, 1999; Amelung *et al.*, 2000); landslides (Carnec *et al.*, 1996; Fruneau *et al.*, 1996), and man-induced deformation like those produced by fluid extraction (Carnec and Fabriol, 1999; Fialko and Simons, 2000; Hole *et al.*, 2007) and mining (Carnec and Delacourt, 2000; Wegmüller *et al.*, 2004).

The magnitude of the deformation and the spatial scale over which it occurs determine whether a signal is measurable by differential SAR interferometry. The limits of detectability include: pixel size, swath width, gradient of deformation, and phase and atmospheric noise levels.

The *pixel size limit* restricts the spatial extent of an observable movement to values much larger than the dimension of a focused radar pixel. Deformation at smaller spatial scales, such as spalling in sidewalk pavement, does not appear in interferograms.

Similarly, the deformation is easiest to interpret if it fits within the ~100-km width of the radar swath; this is the *swath width limit*. It is possible to study broad signals by abutting successive radar images along the swath (parallel to the satellite ground track), but it is not straightforward to join two adjacent swaths (across track) because they do not start and end at exactly the same times.

The fringe pattern becomes incoherent in the presence of high spatial gradients or large deformation rates. If the relative displacement between two neighboring pixels exceeds one fringe, it cannot be measured using InSAR. Thus, the maximum theoretically detectable deformation gradient is one fringe per pixel. This is understandable, since the phase difference value in a wrapped interferogram is between $-\pi$ and π. This means that the maximum difference in phase between two neighboring pixels is 2π, corresponding to one fringe high phase gradients. In practice, the maximum detectable deformation gradient is much less, due to the presence of noise and phase decorrelation in the interferogram (see previous subsection). Previous investigations (e.g. Spreckels *et al.*, 2001; Wegmüller *et al.*, 2004) show that for C-band data it often becomes impossible to correctly resolve gradients of more than 3 phase cycles (fringes) per 1 km horizontal distance. Discontinuities such as surface rupture also exceed this limit because they produce an infinite gradient. Reducing the observation period and increasing the wavelength used (L-band) could be possible solutions to this problem.

The deformation is significant only if it produces a range change larger than the measurement uncertainty. This *small-gradient limit* restricts interpretation to signals with magnitude of the better part of a fringe (~1 cm) over a scene (~100 km), or strains larger than 10^{-7}. Tidal loading of the continents produces deformation close to this limit. Smaller signals are detectable if they are strongly structured like atmospheric waves.

III.2 DInSAR data processing steps.

In this thesis work, the InSAR data processing stage is performed using the *Delft Object-oriented Interferometric Software* (Doris) (Kampes and Usai, 1999; Kampes *et al.*, 2003; Kampes, 2005). Doris was chosen because it is a fully functional interferometric processing software in the public domain. Doris uses other public domain software to perform dedicated tasks. This includes *getorb* software to obtain precise orbital data records for the ERS and Envisat satellites (Scharroo and Visser, 1998), *Statistical-Cost, Network-Flow Algorithm for Phase Unwrapping* (snaphu) (Chen and Zebker, 2000, 2001), *Generic Mapping Tool* (GMT) for general plotting and gridding (www.soest.hawaii.edu/gmt; Wessel and Smith (1998)).

Doris is not a SAR processor, i.e. the input data for Doris interferometric processing must be in a SLC format, focused image.

There are six major processing steps necessary to compute a coherence map, interferogram, differential interferogram, and LOS displacement map: (1) data preparation, (2) coregistration of the radar images, (3) products generation (coherence, interferogram, differential interferogram), (4) filtering of the phase image, (5) phase unwrapping and (6) geocoding. These steps are now described at details.

Step 1: Data preparation.

First, two radar images are needed. One is the master and the other is the slave (image details in the Table 1).

The first step in the data processing consists of inputting of both master and slave data sets and creating a result file where the relevant parameters are stored (*Pulse Repletion Frequency* (PRF), wavelength, etc.). In order to decrease the time and disk space necessary for interferometric processing, the images was cropped. Figure 10 shows the magnitude and phase images of the cropped master image.

Table I. Image parameters.

Tabla 1: Parámetros de las imágenes.

Image Parameters	**Master Image**	**Slave Image**
Frame number	84	84
Orbit number	14667	15168
Acquisition date	19-DEC-2004	23-JAN-2005
Acquisition time (UTC)	17:50:34.24	17:50:35.68
Number of lines originally	24246	24244
Number of range pixels originally	5172	5172
Radar wavelength (m)	0.0562356	0.0562356
Sensor Platform Mission Identifier	ENVISAT-ASAR-SLC	ENVISAT-ASAR-SLC
Product type specifier	ASAR	ASAR

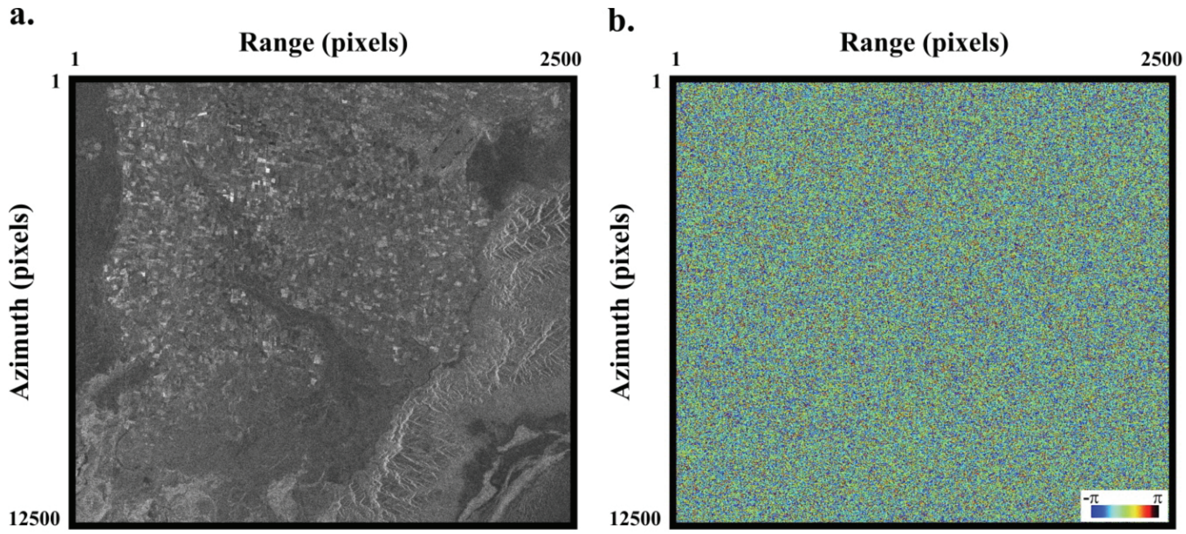

Figure 10: a. Magnitude image. Light colors represent high magnitude, whereas dark colors indicate areas of low magnitude of the returned signal. b. Phase image, color-coded according to the bar at lower right.

Figura 10: a. Imagen de magnitud. Los colores claros indican alta magnitud mientras que colores oscuros representan baja magnitud de la señal de regreso. b. Imagen de la fase, codificada en color según la barra de abajo a la derecha.

After inputting the SLC data, the satellite orbit interpolation step was performed. To obtain the precise orbit of the satellite, the *Delft Institute for Earth-oriented Space Research* (DEOS) program *getorb* and satellite ephemerides have been used. The *Orbital Data Records* (ODR) was obtained from the DEOS ftp site. Based on the image acquisition time and the image size in azimuth direction, the satellite ephemerides were extracted from ODR files and interpolated (using cubic splines) into one-second intervals. The satellite ephemerides were then converted into the output table in the following order: second_of_day, x, y, z. The orbit coordinate system is WGS84.

Step 2. Coregistration and resampling of the radar images.

Before the interferogram computation, the coregistration process of lining up two images (master and slave) covering the same area must be undertaken. This is essential and not always easy. Coregistration can be defined as a geometric image transformation and subsequent resampling of the slave image in such way that each ground point is located at the same position in both images. Subpixel accuracy in the coregistration process is necessary to obtain coherent interferometric products. The determination of the coregistration polynomial that describes the transformation of the slave to the master is performed in 4 steps in Doris.

In the first step the offset vector between master and slave images is calculated based on their orbits. This is the faster approach to obtain the offset within an accuracy of about 30 pixels. The second step is the coarse coregistration. The purpose of the coarse coregistration step is to determine one offset for the entire image, but with an accuracy of approximately one pixel. To perform this task, the cross-correlation technique based on the magnitude (squared amplitude) of both images, for a number of evenly distributed locations over the entire image, is applied. For coarse coregistration, 201 windows with 256 x 256 pixel size were distributed. The procedure consists of presenting a set of different offsets for given positions and determining the correlation between the images for each offset. The offset obtained in the previous step based on the satellite orbits was used as initial offset. In several cases, I had a problem with the automatic initial offset estimation, due to its very large value. In these cases an independent estimation was performed using the master and slave magnitude images and the *xv* software.

The offset with the highest correlation is the estimation for a particular position. Finally, the offset with the highest number of occurrences over the entire number of different positions is adopted as the approximate offset between the master and slave images. Although the computation can be performed in the space domain or spectral domain, the spectral domain method is faster. In the third step, a fine coregistration is performed in order to estimate a large number of offsets at evenly distributed locations with sub pixel accuracy. The same cross-correlation technique is used. However, the number of correlation windows is significantly increased. For the fine coregistration 601 windows with 64 x 64 pixel size were used, distributed over the magnitude image.

Before the fine registration both master and slave images were azimuth filtered. This filter removes the part of the spectrum that does not overlap due to the different Doppler frequency of the two images.

Finally, after the offsets are obtained at a number of positions in the image, a threshold is chosen to select patches that contain useful information, and a 2D-polynomial of degree 2 (by default) is fitted through these offset vectors. A least squares fit, weighted by the coherence, is used. Using the estimated polynomial, the slave image is resampled to the master grid.

Step 3: Computation of interferometric products

In this step the complex interferogram and the coherence image are generated.

Once the master and slave images are on the same grid, each complex pixel of the master image is multiplied by the complex conjugate of the same pixel in the slave image to find the phase differences between corresponding pixels. The phase of the complex interferogram represents the phase difference between the two SAR data sets, while the amplitude image contains useful information about the SNR of the observed phase. Figure 11a and b shows the phase and magnitude image of the complex interferogram for the Mexicali Valley study area, respectively. Fringes parallel to the flight path and corresponding to the uniform surface of the Earth are clearly visible, and in some places are disturbed by the topography or by some decorrelation (Figure 11a).

Before any further analysis and computation are performed, the phase corresponding to the effect of the curvature of the earth needs to be removed. The precise orbits and the WGS84 ellipsoid are used to compute the reference phase.

After this step the interferometric phase contains information on topography, possible deformation, and possibly atmospheric effect (Figure 11c). Thus, the topographic contribution must be removed from the interferogram to reveal the deformation. To do this, the topographic phase is simulated using a DEM and the estimated baseline, and then it is subtracted from the interferogram (Figure 11d). For this step *Shuttle Radar Topography Mission* (SRTM) 3-arcsec digital elevation model freely downloaded from NASA (*National Aeronautics and Space Administration*) via anonymous ftp at ftp://e0srp01u.ecs.nasa.gov/srtm/ was used. The remaining signal in the interferogram should be a contour map of surface deformation, expressed with fringes (a complete cycle of color, i.e., from blue to blue), each showing a full cycle of phase change (i.e. one wavelength, 5.66 cm for Envisat). Because the round-trip range is measured, each fringe represents half a wavelength surface change (2.83 cm for Envisat) along the radar line of sight. Atmospheric artifacts may also be present in the interferogram.

The resolution of the interferogram plays a very important role, especially when the purpose of interferometry is to detect deformation of relatively small spatial phenomena. In Doris, the interferogram is by default computed using a multilook factor of 5 in azimuth and 1 in range. In order to improve the SNR, to reduce the speckle and get approximately square shaped pixel, the interferogram was multilooked with a factor of 20 x 4, in the azimuth and range directions respectively. For Envisat, with pixel size of 5 m in azimuth, and 25 m in ground range, this results in 100 m x 100 m pixel ground resolution. This procedure decreases the resolution of the method, but improves the visibility of the fringes (improves coherence) that is very important in an area where the principal limitation of InSAR technique is temporal decorrelation.

Doris can also compute a coherence image that can be used as input for the cost function computations in the unwrapping program (Figure 12).

Step 4: Filtering of the phase image.

Phase filtering is applied to the differential wrapped phase interferogram in order to reduce the level of noise and improve the unwrapping process. Therefore this step can improve the quality of the final deformation maps. However, while filtering reduces noise in the interferogram, it does not necessarily enhance or recover the signal. In Doris, phase filtering can be applied using different methods, which include a simple pre-defined spatial averaging kernel, 2D convolution kernels, or the Goldstein filter (Goldstein and Werner, 1998). In this thesis the adaptive non-linear Goldstein filter was applied which makes use of the fact that the fringe spectrum is generally narrow band relative to broad-band noise spectrum. This adaptive radar interferograms filter is based on the concept of multiplication of the Fourier spectrum $Z(u,v)$ of a small interferogram patch by smoothed absolute $S\{|Z(u,v)|\}$ value to the power of an exponent α :

$$H(u,v) = S\{|Z(u,v|\}^{\alpha} Z(u,v) . \qquad (21)$$

where $H(u,v)$ is the filter response (the spectrum of the filtered interferograma); $S\{\ \}$ is a smoothing operator which represents convolution of power spectrum with 1 D kernel function; u and v are spatial frequencies; and α is the filter parameter. Patches are defined as a small square segment of the interferograma and are overlapped to prevent discontinuities at the boundaries[2]. The filter parameter α is an arbitrarily chosen value. In this thesis the α range is between 0 and 1.8. For the value of $\alpha = 0$, no filtering occurs. However, for large values of α, the filtering is strong. Useful value of α lie in the range 0.2 to 0.5 given interferograms with moderate correlation $\gamma > 0.25$. Interferograms with very low correlation benefit from larger patches sizes and higher value of α.

The adaptive interferogram filtering algorithm significantly improves fringe visibility and reduces noise introduced by temporal or baseline related decorrelation, thus helps to avoid the image corruption effect during the application of the unwrapping process. The variable bandwidth of the filter, derived directly from the power spectrum of the fringes preferentially smoothes the phase in regions with high correlation, but remains broad-band in regions where the correlation is low. Figure 14 a shows an example of filtered differential interferogram.

[2] In this thesis the parch size of 32 by 32 pixels with ~50% overlap in x, y was used.

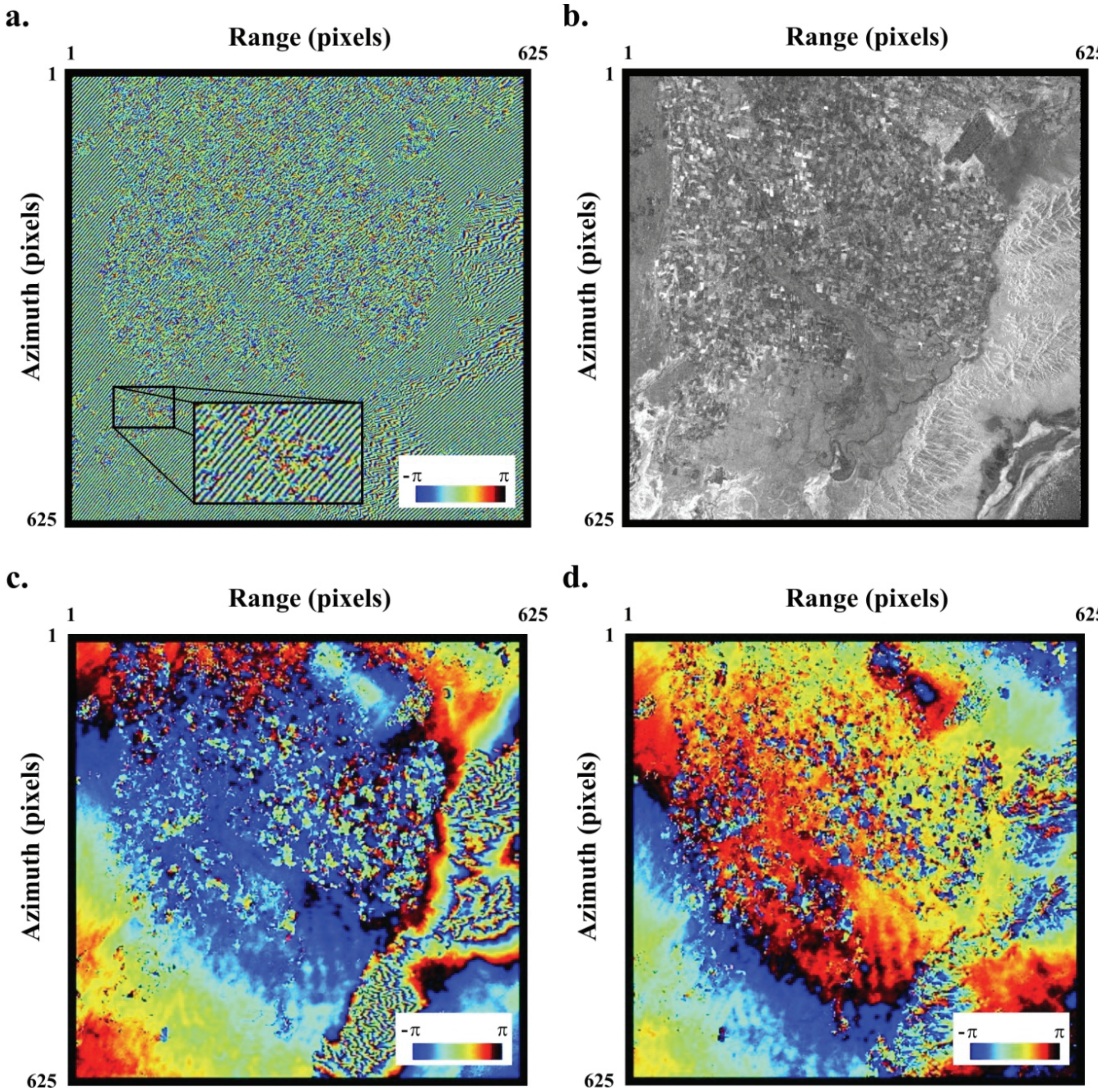

***Figure 11:** a. Phase image with a visible flat Earth pattern (pixel size 100 × 100 m^2). b. Magnitude image. c. The phase image of the complex interferogram. The reference phase has been subtracted. Visible fringes correspond to the deformation and to local topography. d. Differential interferogram. Topographic information has been removed from the complex interferogram using SRTM DEM.*

***Figura 11:** a. Imagen de fase interferométrica con un patrón de "terreno plano" visible patrón (el tamaño de pixel es de 100 × 100 m^2). b. Imagen de magnitud. c. Imagen de fase interferométrica después de substraer la fase de referencia (del cuerpo de referencia). Las franjas visibles corresponden a la deformación y a la topografía local. d. Interferograma diferencial. La información topográfica fue quitada del interferograma inicial usando el MDE (Modelo Digital de Elevación) de la misión SRTM.*

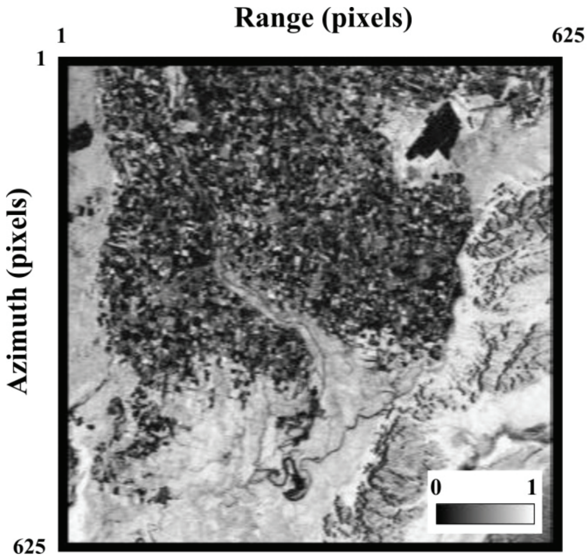

Figure 12. Coherence image.

Figura 12. Imagen de coherencia.

Step 5: Phase Unwrapping.

Phase unwrapping is the reconstruction of the original phase from the wrapped phase representation. A schematic illustration of the phase unwrapping process in 1-D and 2-D is presented in Figure 13. The correct integer number of whole phase cycles has to be found in order to obtain the absolute phase signal. However, due to the presence of phase noise, the unwrapping process is a critical step of the interferometric processing chain.

Doris calls the snaphu phase unwrapping software for the phase unwrapping computations. The snaphu phase unwrapping software is described in Chen and Zebker (2000, 2001). Phase unwrapping calculates the phase change in the interferogram from one point to the next and then integrates it to get the smooth phase function. Thus, if the surface is smooth (with no, or only small, phase jumps between points) the unwrapping process is easy. The process is difficult if the surface is rough. It any case, phase jumps from point to point should not exceed one half cycle from point to point. An unwrapped interferogram is presented in Figure 14b.

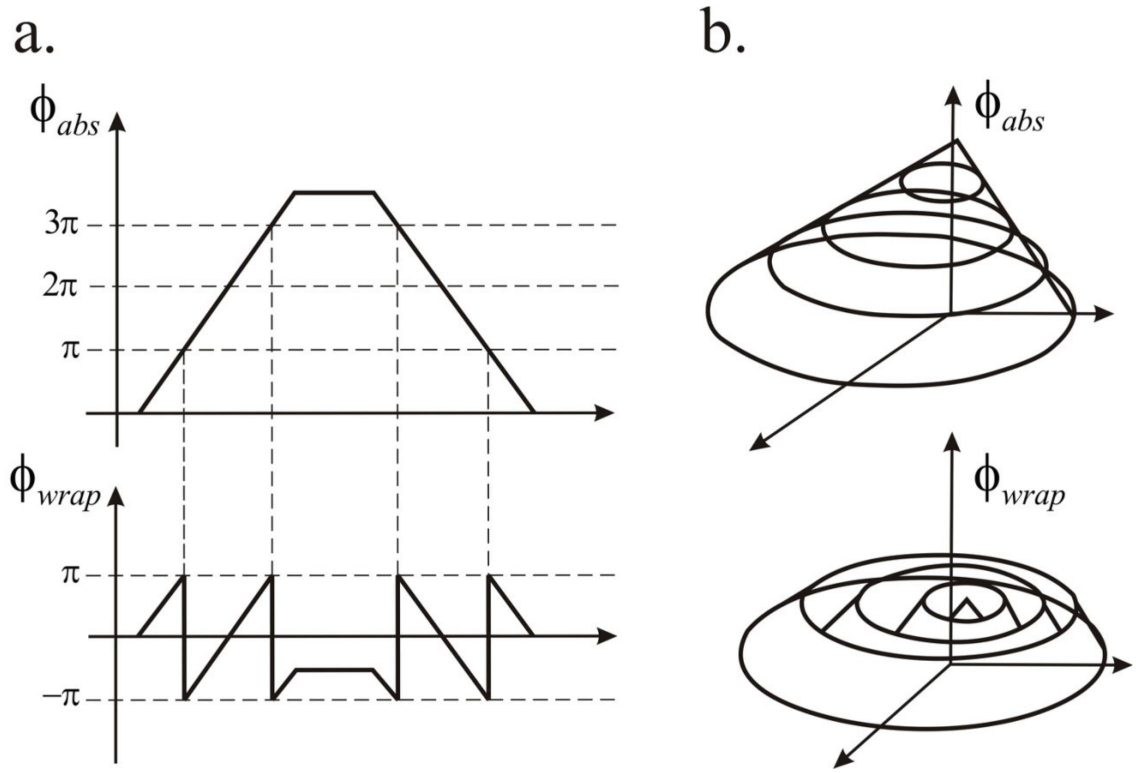

Figure 13: Schematic illustration of phase unwrapping in (a) 1-D (from Belabbes, 2008) and (b) 2-D (from Hadj Sahraoui et al., 2006).

Figura 13: Ilustración esquemática del desenrollo de la fase en (a) 1-D (de Belabbes, 2008) y (b) 2-D (de Hadj Sahraoui et al., 2006).

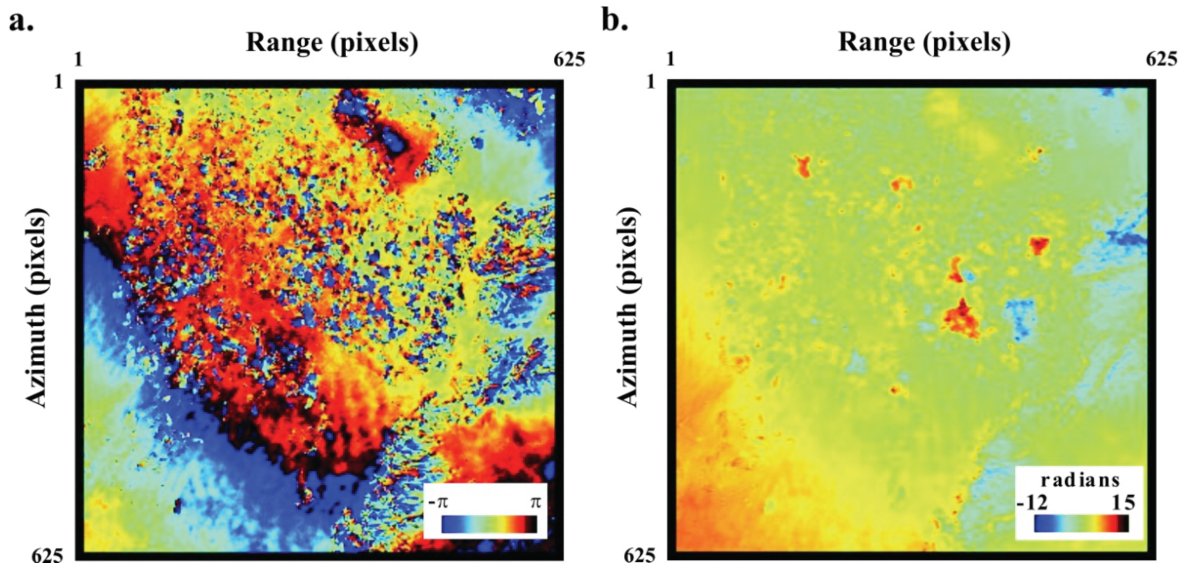

Figure 14: a. Wrapped phase interferogram filtered using the Goldstein radar interferogram filter ($\alpha = 0.2$). b. Unwrapped interferogram.

Figura 14: a. Interferograma de fase enrollada filtrada usando filtro de interferogramas del radar de Goldstein ($\alpha = 0.2$). b. Interferograma de fase desenrollada.

Step 6: Geocoding.

In this step the pixel coordinates are georeferenced, and files with longitude and latitude coordinates are created using the precise orbit information. Using these files and the GMT software, the matrices of geocoded coherence, amplitude, wrapped and unwrapped phase data are created and gridded. The linear trend in phase, due to inaccurate data on satellite's position, was calculated and removed from unwrapped phase data, and incoherent areas, having coherence <0.1, were masked out. The LOS displacement grid was created from unwrapped phase data, using the corresponding wavelength (5.66 for Envisat) and equation (14). The visualization of geocoded results was performed using ER Mapper 7.1. The final LOS displacement map is in geographic coordinates system and *North American Datum 1927* (NAD27) (Figure 15).

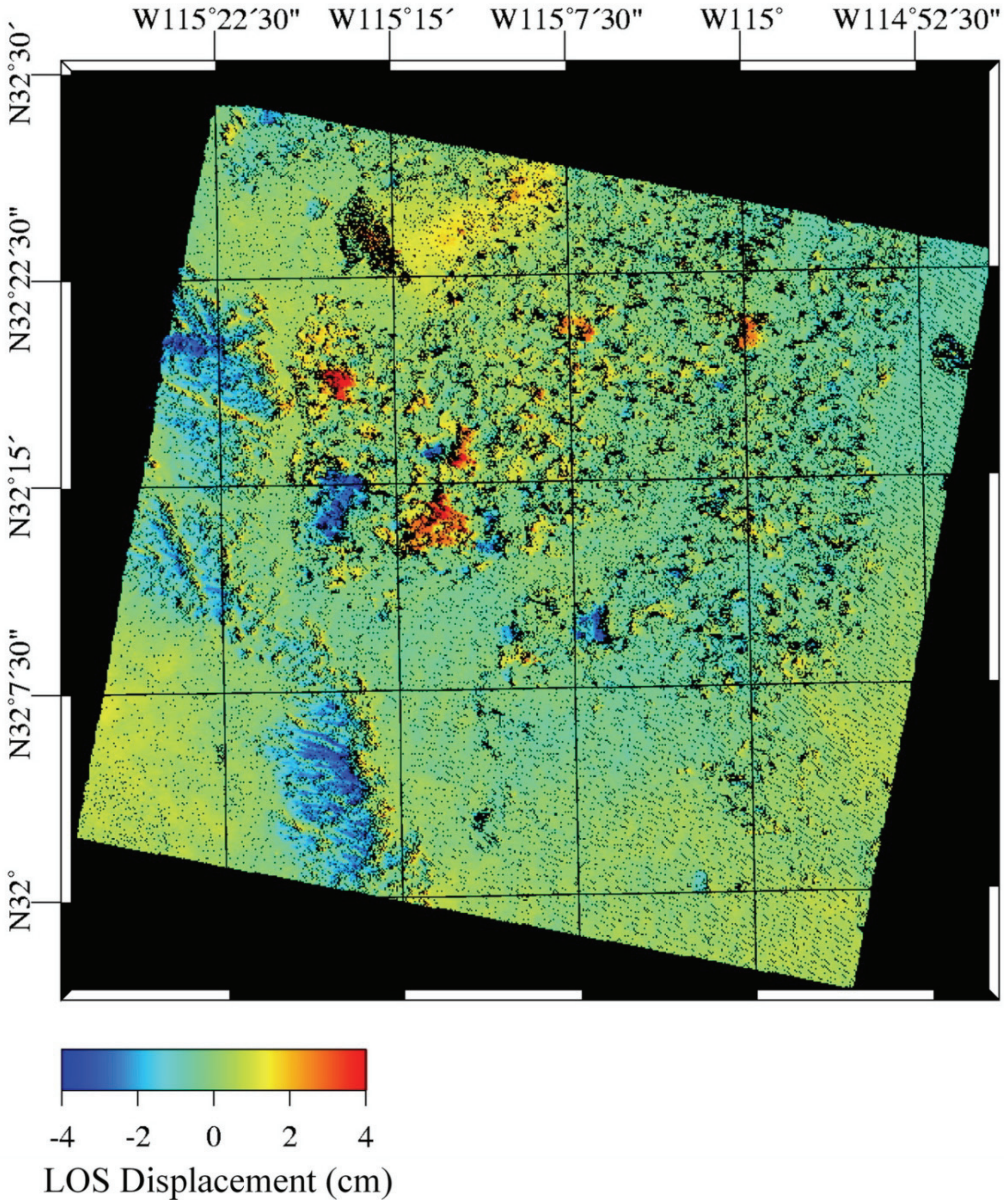

Figure 15: LOS displacement map in geographic coordinate system and NAD27 datum. Areas of low coherence (<0.1) are masked.

Figura 15: Mapa del desplazamiento a lo largo de línea de vista del radar (LOS) en coordenadas geográficas y NAD27 datum. Las áreas de baja coherencia (<0.1) están enmascaradas.

CHAPTER IV

THE SPATIAL AND TEMPORAL CHANGES IN THE ANTHROPOGENIC SUBSIDENCE PATTERN IN THE MEXICALI VALLEY: RESULTS FROM DINSAR AND LEVELING.

IV.1 Introduction

Land subsidence is a complex deformation process and may be defined as the slow sinking of the land surface. Land subsidence occurs both naturally and through anthropogenic means. Relatively slow subsidence caused by the natural process of sediment compaction due to its own weight and tectonic movements (geological or natural subsidence) is widespread but seldom causes problems on human timescales. More rapid subsidence of the ground surface is usually attributed to human activities (anthropogenic subsidence), such as the subtraction of earth material by mining or the extraction of fluids from an aquifer or geothermal and hydrocarbons reservoir. However, it is better not to underestimate the importance of natural subsidence as it may be linked to the causes of subsidence during human activities (Whittaker and Reddish, 1989; Martz, 2009).

In a geothermal field, surface deformation occurs as a consequence of extracting the geothermal fluid at a speed higher than the recharging and/or injection rate. The surface deformation occurs even if the reservoir is deep and isolated from shallow groundwater (Vasco *et al.*, 2002). Land subsidence is induced by volume changes or reduction of subsurface pore pressure in the geothermal reservoir by depletion of the fluid storage, which reduces the reservoir's compressive strength and allows subsidence of overlying strata into the reservoir; but other factors, including contraction by cooling, could contribute. In the Mexicali Valley, the Cerro Prieto Geothermal Field has been utilized on a large scale to provide heat to generate electricity, causing localized subsidence (Glowacka *et al.*, 1999, 2005; Sarychikhina, 2003).

Even if the ground subsidence due to fluid extraction does not pose the type of hazards associated with sudden and catastrophic natural events like earthquakes or volcanic eruptions, its economic and environmental impacts can be substantial. Ground subsidence can disrupt surface drainage, reduce aquifer system storage, form ground fissures (cracks and separations) and damage properties, farmlands, and infrastructures that may be costly to replace or repair (Schumann *et al.*, 1986; Sheng and Helm, 1998; Feng *et al.*, 2008; Wang *et al.*, 2009). It can also greatly increase the flooding potential in the coastal areas and areas which surround the aqueducts or canals (Potok, 1991; Yong *et al.*, 1991; Dixon *et al.*, 2006; Cabral-Cano *et al.*, 2008).

Geothermal fluid and/or oil and gas reservoirs are likely to be associated with faults. Thus, pre-existing tectonic faults or/and faults originally caused by subsidence are an important concern when considering land subsidence, in the case of geothermal fluid, oil and gas extraction. Pre-existing faults can affect the stress distribution of the reservoir and produce unpredictable surface subsidence results. Any slippage of the fault can result in changes of groundwater flow or change the permeability as faults can act as hydrologic barriers. Fault displacement may also propagate to the surface creating surface displacement which may affect engineered structures. The orientation of the faults can also contribute to the shape and extension of the subsidence-affected area (Ferronato *et al.*, 2007). However, it is important to sign that often times it is difficult to deduce whether subsidence along a fault line has been caused by tectonic movement or if the mechanism is anthropogenic.

In the Mexicali Valley the ground fissuring and faulting, and local infrastructure damages caused by subsidence have been described and mapped by González *et al.* (1998), Lira (1996, 1998, 2005), Glowacka *et al.* (2006, 2010) and Suárez-Vidal *et al.* (2008) (Figure 16). Identification of land subsidence in the geothermal field and monitoring of the spatial and temporal changes of its pattern and magnitude can provide important information about the dynamics of this process and its controlling geological structures. This information can be useful for estimating future subsidence, so measures can be taken to prevent damage to infrastructure and environment.

Identification and monitoring of ground deformation can be accomplished using a number of techniques. In this chapter, the analysis of ground subsidence in the Mexicali Valley was performed. The DInSAR data from conventional two-pass DInSAR method and from stacking was analyzed. The stacking results which span December 2004 and December 2005 were compared with available leveling data from the 1994-1997 and 1997-2006 periods in an attempt to evaluate the changes in the spatial pattern and rate of subsidence. The observed subsidence pattern was also compared to the tectonic framework of the region.

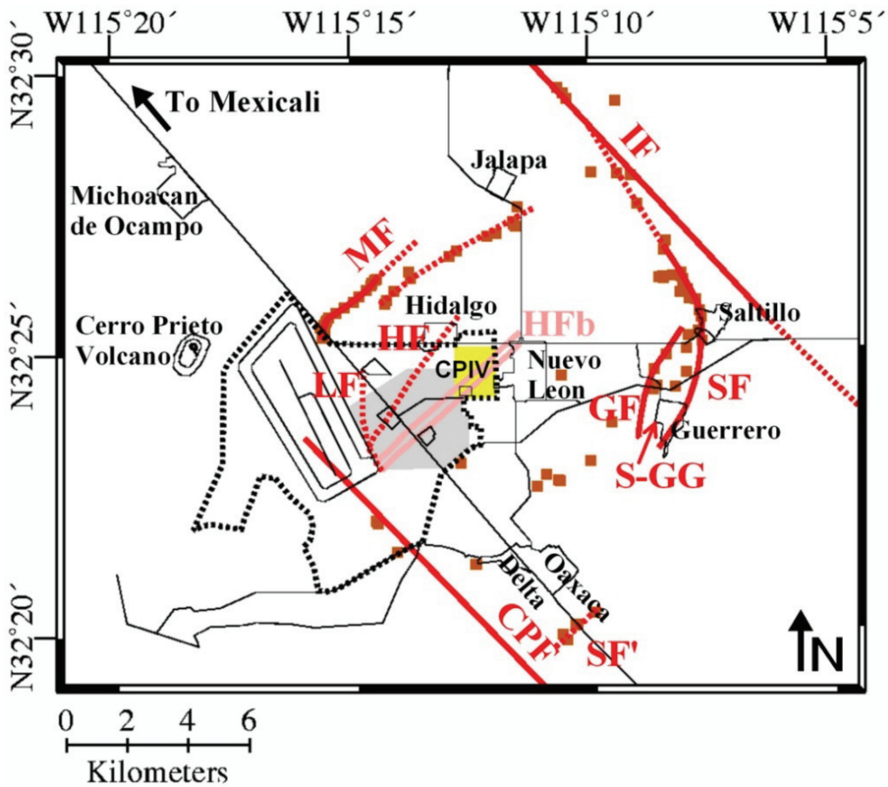

Figure 16: Detailed plan of the study area with principal roads, villages and features (as Cerro Prieto volcano and evaporation pond) (solid black line). Solid red lines are well-known surface traces of tectonic faults. CPF=Cerro Prieto fault, IF=Imperial fault, SF=Saltillo fault, MF=Morelia fault, GF=Guerrero Fault. SF and GF form structure known as Saltillo-Guerrero graben (S-GG). Dotted red lines are proposed surface fault traces based on mapped fissure zones (brown squares) from González et al. (1998), Lira (2006), Suárez-Vidal et al. (2007, 2008), and Glowacka et al. (2006, 2010) and wells data (as a case of HF=H fault, and LF=L fault) from Lippmann et al. (1984). SF' is continuation of Saltillo fault as proposed by Suárez-Vidal et al. (2008). HFb is H fault on the intersection with top of β reservoir (solid rose lines). The black dotted line frames the limits of the CPGF. The gray polygon indicates extraction area before year 2000; the yellow rectangle indicates the extraction area of CPIV which started the operation since 2000.

Figura 16: El plan detallado del área de estudio con principales caminos, poblados y características (tales como Volcán Cerro Prieto y laguna de evaporación). Líneas continuas rojas son las trazas superficiales de fallas conocidas. CPF=Cerro Prieto, IF=falla Imperial, SF=falla Saltillo, MF=falla Morelia, GF= falla Guerrero. SF y GF forman estructura conocida como graben Saltillo-Guerrero (S-GG). Líneas rojas discontinuas son trazas superficiales de fallas propuestas basando en las zonas mapeadas de fisuras (cuadrados cafés) de González et al. (1998), Lira (2006), Suárez-Vidal et al. (2007, 2008), and Glowacka et al. (2006, 2010) y datos de pozos (como es el caso de HF=falla H y LF=falla L) (Lippmann et al., 1984). SF' es continuación de falla Saltillo como fue propuesto por Suárez-Vidal et al. (2008). HFb es la intersección de la falla H con el techo del reservorio β (líneas rosas solidas). La línea negra punteada enmarca los límites del CPGF. El polígono gris indica el área de extracción hasta el año 2000, un rectángulo amarillo indica el área de extracción de CPIV que inició su operación a partir de 2000.

IV.2 DInSAR data analysis

IV.2.1 Data

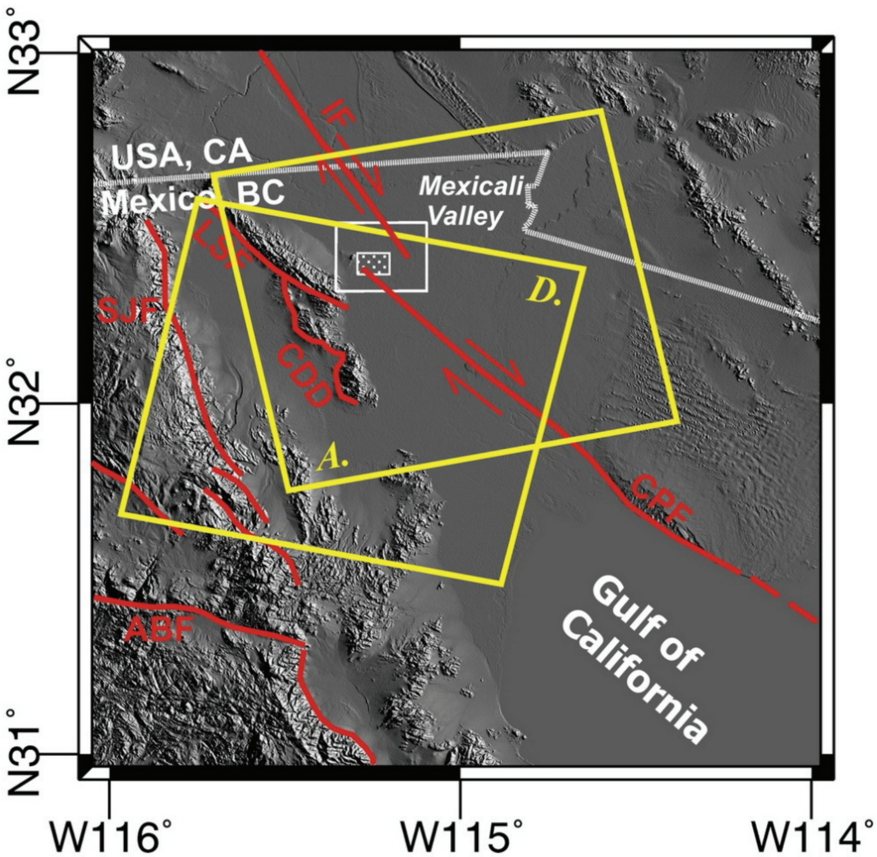

Figure 17: Regional map of the study area. SRTM DEM is used as the background. Large yellow rectangles indicate the spatial coverage of Envisat SAR images. D indicates descending track, and A indicates ascending track. The white rectangle represents the study area. The smaller filled rectangle represents the Cerro Prieto Geothermal Field. The principal tectonic faults are also indicated: CPF=Cerro Prieto fault, IF=Imperial fault, ABF=Agua Blanca fault, SJF=Sierra Juarez fault, LSF=Laguna Salada fault and CDD=Cañada David detachment.

Figura 17: Mapa regional del área de estudio. SRTM DEM es utilizado como fondo. Los rectángulos amarillos indican la cobertura espacial de las imágenes SAR de Envisat. D indica imagen descendente y A indica imagen ascendente. El rectángulo blanco representa el área de estudio. El rectángulo pequeño relleno representa el Campo Geotérmico de Cerro Prieto. Las principales fallas tectónicas también son indicadas: CPF=falla Cerro Prieto, IF=falla Imperial, ABF=falla Agua Blanca, SJF=falla Sierra Juárez, LSF=falla Laguna Salada y CDD=falla de bajo ángulo Cañada David.

Data from Envisat ASAR systems were used for the analysis presented in this chapter. The Envisat satellite was launched by the ESA in February 2002. Envisat ASAR is a C-band sensor with an average (scene center) incidence angle of 23° and 35 days revisit. A total of 17 SLC images from descending satellite track 84 and frame 2961 and 5 SLC images from ascending satellite track 306 and frame 639 were acquired over the study area from October 2003 to May 2006 by the ESA. The spatial coverage of these images is presented in Figure 17.

IV.2.2 Interferograms processing and analysis

Interferometric processing was done using the public domain DORIS InSAR package (Kampes *et al.*, 2003) following the steps described in chapter III.2.

First, 10 and 136 possible interferometric pair's combinations were formed from ascending and descending datasets, respectively (Table II & III).

Table II: $B_{\perp}$ ***(m)/*** B_{temp} ***(days) for possible interferometric pairs combinations from ascending track (track 306, frame 639) datasets. The gray background indicates interferometric pairs with better baselines parameters. Red numbers identify the interferometric pairs presented in this thesis.***

Tabla II: $B_{\perp}$ ***(m)/*** B_{temp} ***(días) para las posibles combinaciones de pares interferométricos del paso ascendiente (paso 306, toma 639). El fondo gris indica los pares interferométricos con mejores parámetros de líneas de base. Los números rojos señalan los pares interferométricos presentados en este trabajo de tesis.***

Master Image	***Slave Image***			
	2004/02/24	***2004/05/04***	***2006/04/04***	***2006/05/09***
2003/12/16	-157/70	-589/140	-877/840	-1346/875
2004/02/24		-430/70	-720/770	-1188/805
2004/05/04			-290/700	-765/735
2006/04/04				-470/35

Master Image	Slave Image															
	2004/05/23	2004/09/05	2004/10/10	2004/12/19	2005/01/23	2005/02/27	2005/04/03	2005/05/08	2005/06/12	2005/07/17	2005/08/21	2005/09/25	2005/10/30	2005/12/04	2006/02/12	2006/03/19
2003/10/26	-128/210	280/315	-147/350	-699/420	-648/455	-587/490	-1025/525	183/560	-641/595	239/630	-269/665	-445/700	57.6/735	-690/770	-988/840	-278/875
2004/05/23		401/105	-37/140	-579/210	-524/245	-466/280	-902/315	2/350	-521/385	358/420	-152/455	-321/490	140/525	-570/560	-867/630	-163/665
2004/09/05			-408/35	-978/105	-924/140	-865/175	-1302/210	-106/245	-919/280	-46/315	-548/350	-721/385	264/420	-968/455	-1267/525	-557/560
2004/10/10				-578/70	-520/105	-466/140	-899/175	303/210	-521/245	363/280	-162/315	-318/350	144/385	-571/420	-865/490	-175/525
2004/12/19					77/35	112/70	-323/105	877/140	58/175	937/210	430/245	264/280	719/315	9.1/350	-290/420	422/455
2005/01/23						75/35	-378/70	822/105	60/140	882/175	378/210	204/245	662/280	-73/315	-345/385	373/420
2005/02/27							-433/35	765/70	-53/105	824/140	318/175	154/210	607/245	-103/280	-401/350	310/385
2005/04/03								1201/35	386/70	1259/105	756/140	581/175	1041/210	338/245	46/315	750/350
2005/05/08									-817/35	61/70	-450/105	-620/140	-160/175	-870/210	-1166/280	-460/315
2005/06/12										879/35	371/70	206/105	660/140	-49/175	-348/245	-364/280
2005/07/17											-507/35	-678/70	220/105	-928/140	-1225/210	-516/245
2005/08/21												-181/35	291/70	-419/105	-720/175	-14/210
2005/09/25													460/35	-260/70	-547/140	178/175
2005/10/30														-710/35	-1007/105	-302/140
2005/12/04															-300/70	412/105
2006/02/12																-712/35

Table III: $B_{\perp}$ (m)/B_{temp} (days) for possible interferometric pairs combinations from descending track (track 84, frame 2961) datasets. The gray background indicates interferometric pairs with better baselines parameters. Red numbers identify the interferometric pairs presented in this thesis.

Tabla III: $B_{\perp}$ (m)/B_{temp} (días) para las posibles combinaciones de pares interferométricos del paso descendiente (paso 84, toma 2961). El fondo de color gris indica los pares interferométricos con mejores parámetros de líneas de base. El fon rojo distingue los pares interferométricos que están presentados en

Very strong spatial decorrelation was observed for interferometric pairs with perpendicular baselines longer than 400m; these interferometric pairs were excluded from the analysis. By limiting the baseline, the most incoherent interferograms were rejected. The higher limit of perpendicular baseline involves the minimal height ambiguity (height differences corresponding to an interferometric fringe) of ~20 m. The relative height error of SRTM DEM is ~6 m (Muller and Backes, 2003), resulting in no more than ~0.3 fringes, or 0.8 cm, of line-of-sight error in the interferogram with the longest perpendicular baseline. Moreover, the Mexicali Valley has flat topography (with exception of the Cerro Prieto volcano and the foothills of the Cucapah Mountains), a feature that helps mitigate any topography-related artifacts in interferograms.

Subsequently, the residual interferograms were analyzed individually to identify fringes with common geographic location in different interferograms, so that the fringes representing land subsidence could be separated from atmospheric artifacts. It is known that spatial variability of the atmosphere with time, and therefore the fringes produced by atmospheric effects do not usually lie at constant geographic position in independent interferometric pairs, whereas land subsidence may continue to occur at the same locations for a period of time due to prevalence of the conditions responsible for the land subsidence. Visual analysis of residual interferograms also helped to identify the interferometric pairs with strong phase noise.

I found that, in spite of having a short perpendicular baseline, several differential interferograms present a high level of phase noise due to temporal decorrelation of the signal, induced by variations in the dielectric properties of the targets, between the two acquisitions. The highly vegetated areas surrounding the CPGF cause significant phase decorrelation of SAR pairs over periods longer than 3 months (105 days), due to the seasonal growth and the movements caused by the wind on the grown plants. By contrast, the mainly desert area of the CPGF maintains high levels of coherence over longer time intervals (Figure 18).

Figures 18 and 19 show geocoded differential interferograms constructed using the two-pass method. All differential interferograms show poorly to fairly well-defined fringes with a common geographic location. Therefore, the observed fringes are not due to atmospheric effects but to ground deformation. The elliptical northeast-southwest directed fringe pattern indicates an increase in range. The relatively steep look angle of the Envisat radar (~23°), the similarity of the fringe pattern for the differential interferograms from descending and ascending tracks (see Figure 18a and b) and the evidence for vertical displacement in the study area from ground-based observations, including leveling measurements, suggest that the observed range increase is mostly due to surface subsidence.

In all the short-term differential interferograms (Figure 18a and b; Figure 19), the highest deformation rate area, elliptical with northeast-southwest elongation, has two isolated regions of maximal subsidence. The first centre of subsidence is located in the CPGF production zone (Figure 16). The second is located in the area between the eastern limits of the CPGF and the Saltillo fault, which was proposed as recharge zone in previous studies (Glowacka *et al*., 1999; Sarychikhina, 2003). The complex subsidence pattern (in form of digit “8”) may indicate the existence of some buried structures within and/or below the aquifer-bearing sedimentary basin fill.

Despite the high phase decorrelation level of the interferometric pairs covering longer time intervals (Figure 18c and d), the same fringe pattern persists in the CPGF production zone where the contours of the fringes outline an elliptic subsidence basin.

The boundary of the subsiding area is well resolved in all short-term interferograms, and it appears to have a surface of about 140 km^2. The area affected by subsidence coincides largely with the shape of the Cerro Prieto pull-apart basin described by Suárez-Vidal *et al.*, 2008. The subsiding area boundaries appear to correlate with faults and/or fissures zones as can be seen in Figures 18 and 19 where they are superimposed onto the differential interferograms. The subsidence ceases abruptly toward the southeast and east at the Saltillo fault. The Cerro Prieto fault limits the subsiding area in the southwest. The subsidence observed along the Saltillo fault is much more abrupt than in the Cerro Prieto fault. This agrees with observations from vertical crackmeter and 3-D witness installed on Saltillo and Cerro Prieto fault, respectively (Glowacka *et al.* 2007; 2008). As it was mentioned in chapter II, the vertical component of displacement for the Saltillo fault is 6 cm/yr and for the Cerro Prieto fault is 3 cm/yr over the 3 meter span of the instruments. The Morelia fault and the fractures zone that continue toward the Imperial fault mark the northern limit of subsidence. The deformation appears less important south and southeast of the fissure zone, which appears to be a continuation of the Saltillo fault, as proposed by Suárez-Vidal *et al.* (2008), and named here SF' (Figure 18 and 19). Note that the influence of the Saltillo-Guerrero graben is not observed in the differential interferograms.

Besides the above described fringe pattern with a common geographic location for all interferograms, a smaller circular fringe pattern is observed south of the evaporation pond in the 2004/12/19-2005/02/27 and 2005/02/27-2005/06/12 interferograms (Figure 19a and b). This fringe pattern is also observed in the 2005/01/23-2005/04/03 and 2005/08/21-2005/10/30 interferograms. In Figure 19a and b the fringe pattern indicates a decrease in range, the same for the 2005/01/23-2005/04/03 interferogram. However, for the 2005/08/21-2005/10/30 interferogram, it indicates an increase in range. The other interferograms were also analyzed but this fringe pattern was not found or was difficult to separate from phase noise. Carnec and Fabriol (1999) observed a similar fringes pattern which indicates decrease in range for 1995/12/16-1996/05/04 interferograms. They attributed this decrease in range to uplift related to the reinjection of waste fluid at the southern part of the evaporation pond, because the central part of observed bowl shaped pattern is located 3 km south of three reinjection wells. However, Hanssen (2001) attributed this fringe pattern to atmospheric artifacts. More detailed geodesic and geophysical studies would be necessary to investigate the origin of this pattern.

Except for the described small circular fringe pattern south of the evaporation pond, the regions surrounding Cerro Prieto pull-apart basin do not show any significant signs of surface deformation and consequently are considered stable for the purposes of this thesis. Some local phase gradients outside of the subsidence area may be due to residual topographic or atmospheric noise.

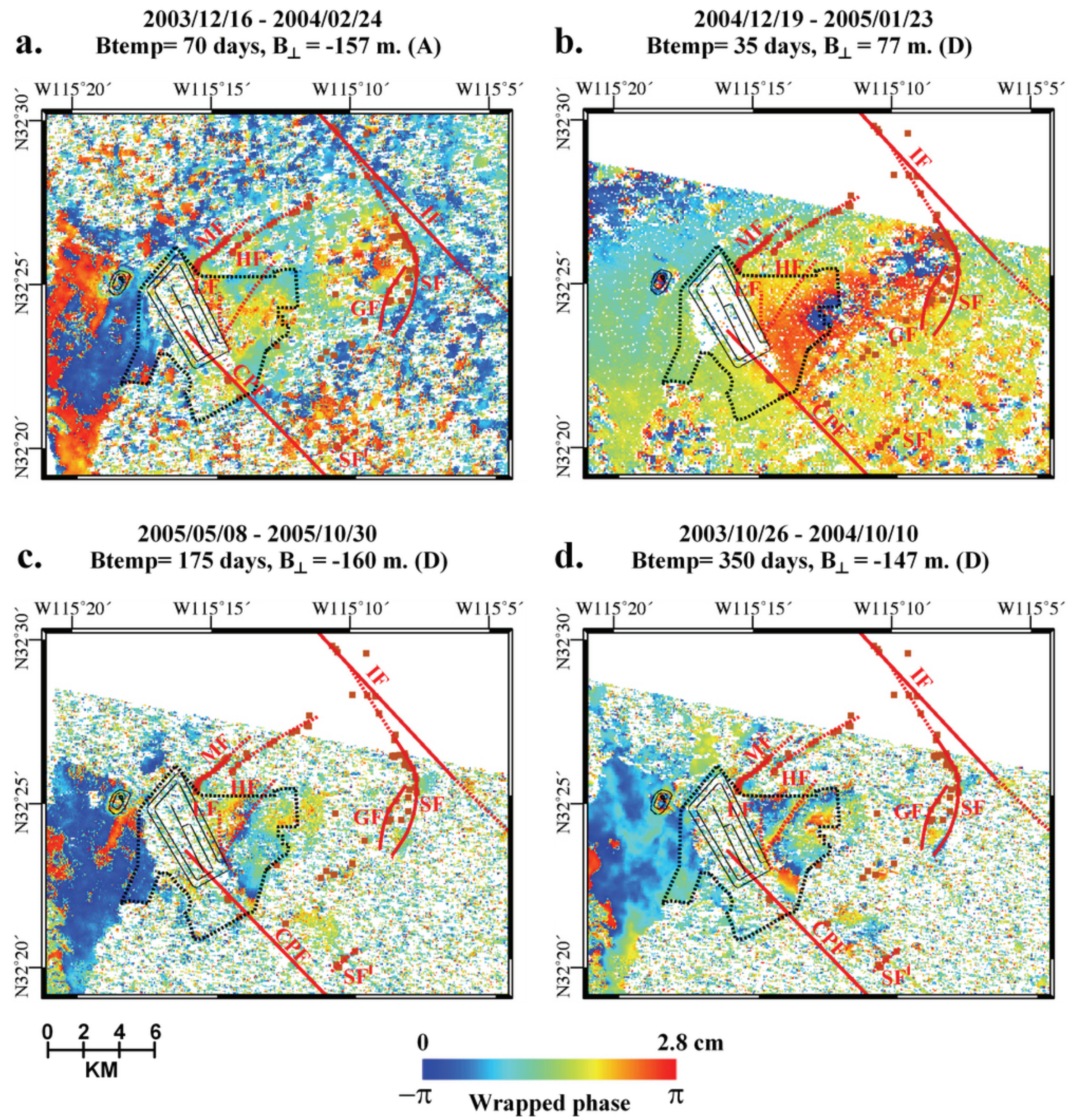

Figure 18: Geocoded differential interferograms. Areas of low coherence (<0.1) are masked. A and D indicate ascending and descending tracks, respectively. The black dotted line frames the limits of the CPGF. The borders of the evaporation pond and the Cerro Prieto volcano are superposed on the images for reference. Faults notation is as in Figure 16.

Figura 18: Interferogramas diferenciales geocodificados. Las áreas de baja coherencia (<0.1) están enmascaradas. A y D indican el paso ascendiente y descendiente, respectivamente. La línea negra punteada enmarca los límites del CPGF. Laguna de evaporación y el volcán Cerro Prieto están sobrepuestos a las imágenes como referencia. Notación de fallas como en la Figura 16.

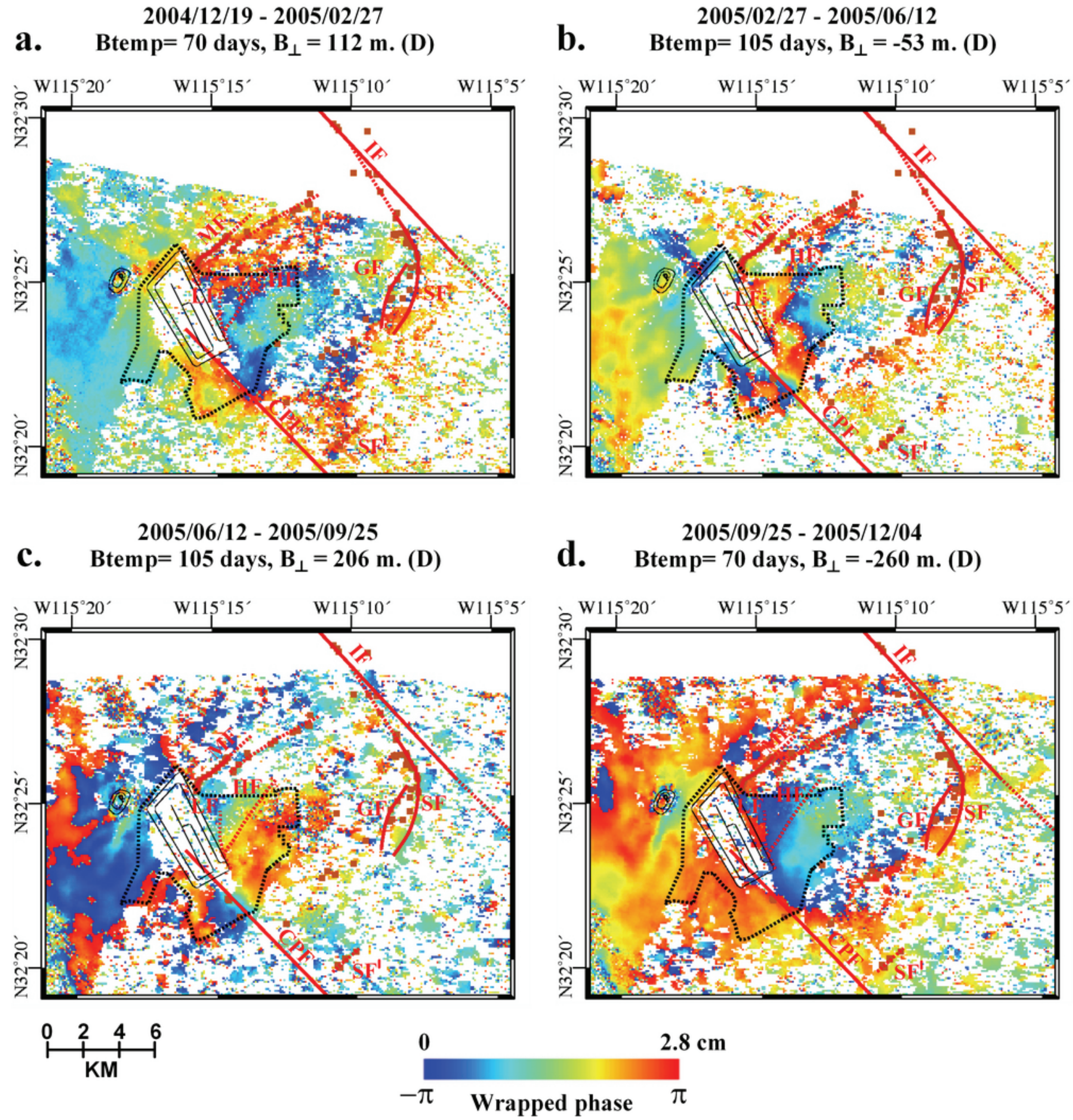

Figure 19: Geocoded differential interferograms. Areas of low coherence (<0.1) are masked. D indicates descending track. The black dotted line frames the limits of the CPGF. Faults notation is as in Figure 16.

Figura 19: Interferogramas diferenciales geocodificadas. Las áreas de baja coherencia (<0.1) están enmascaradas. D indica el paso descendiente. La línea negra punteada enmarca los límites del CPGF. Notación de fallas como en la Figura 16.

IV.2.3 Interferograms stacking

In order to calculate the yearly rate of deformation, a simple d*ifferential interferogram stacking method* was applied. Stacking differential interferograms involves the summing multiple differential interferograms into a single interferogram. This is useful for overcoming the two shortcomings of conventional DInSAR: the low coherence over long temporal separations and the atmospheric influence. Four, visually less noisy, differential interferograms of successive periods, with temporal separations between 70 and 105 days (Figure 19), were selected for stacking.

The phase of each interferogram was first unwrapped using a statistical minimum-cost flow algorithm implemented in the snaphu package (Chen and Zebker, 2001), corrected by orbital error, converted to the LOS displacement (see chapter III.2), and referenced to a common point in the space, which is the fixed point for the leveling 1997-2006 data, benchmark 10037, (Figure 20). The results from the stacking LOS displacement map covered the 350 days long period between December 2004 and December 2005 (Figure 21a). Note that the stacking procedure involves a loss of data over an area representing a union of all decorrelation areas in the original interferograms. Fortunately, the radar phase coherence is preserved for most of the study area. The pattern of subsidence in the resulting LOS displacement map is similar to the pattern obtained in individual interferograms. It consists of an elongated in a NE–SW direction subsidence bowl with two localized areas of subsidence inside. The observed radar LOS displacements were interpreted as indicative of ground subsidence above the geothermal reservoirs and theirs recharge aquifers. The subsiding area is correlated with the area of the Cerro Prieto pull-apart basin. As it can be seen in Figure 21a, the maximum estimated deformation rate is ~16 cm/yr, and occurs in the recharge zone. The maximum deformation rate in the CPGF production zone is ~10 cm/yr.

IV.2.4 Data error estimation

The expected accuracy of LOS displacement rate obtained from interferograms stacking, Δv_{LOS}, was computed as proposed by Strozzi *et al.* (2001):

$$\Delta v_{LOS} = \frac{\sqrt{n}E}{t_{cum}}. \qquad (22)$$

Here, n is the number of interferograms used for stacking, t_{cum} is the total time interval covered by stacking, and E is the assumed phase error of a single interferogram. There is no straightforward method to estimate observation error for the single interferogram. In this thesis the observation error for each interferogram used in the stacking was estimated from the residuals in the non-moving area. These residuals correspond to non-displacement related interferometric disturbances induced mainly by DEM inaccuracies and noise in the differential interferograms. As non-moving area was considered triangular area (~90 km^2) located to the south-east from the evaporation ponds (Figure 20). RMS error for each interferogram was calculated (Table IV) and the average RMS error of ±0.7cm was used to calculate LOS displacement rate accuracy of the stacking. Using equation (22) the expected LOS displacement rate estimation error of approximately ± 1.5 cm/yr was obtained.

Table IV: Estimated uncertainty in the LOS displacement (cm) for single interferogram. The estimation was performed for each interferogram used in the stacking.

Tabla IV: Incertidumbre en el desplazamiento LOS (cm) estimado para una sola interferograma. La estimación fue realiza para cada interferograma usada en el apilamiento.

Master Image	*Slave Image*	*Uncertainty in the LOS displacement (cm)*
2004/12/19	2005/02/27	0.6
2005/02/27	2005/06/12	1.2
2005/06/12	2005/09/25	0.5
2005/09/25	2005/12/04	0.6
	Average:	***0.7***

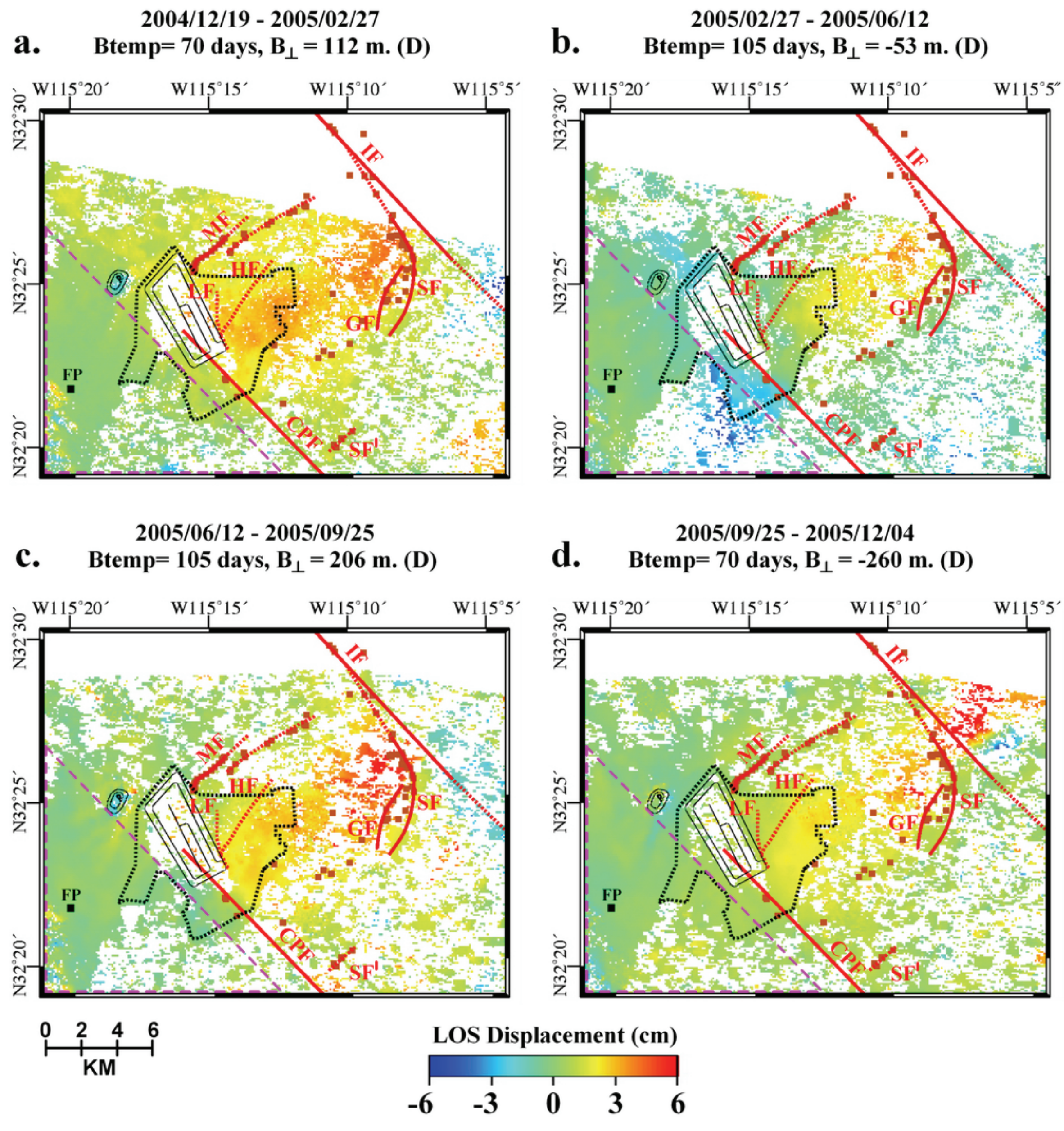

Figure 20: Geocoded LOS displacement maps. Areas of low coherence (<0.1) are masked. D indicates descending track. FP is the fixed point. The magenta dotted triangle marks the limits of the area considered stable and used in the estimation of the error of displacement for the single interferogram. The black dotted line frames the limits of the CPGF. Faults notation is as in Figure 16.

Figura 20: Mapas geocodificados de desplazamiento LOS. Las áreas de baja coherencia (<0.1) están enmascaradas. FP es el punto fijo. D indica el paso descendiente. El triangulo morado punteado marca los límites del área considerada estable que fue usada para la estimación del error de desplazamiento para un solo interferograma. La línea negra punteada enmarca los límites del CPGF. Notación de fallas como en la Figura 16.

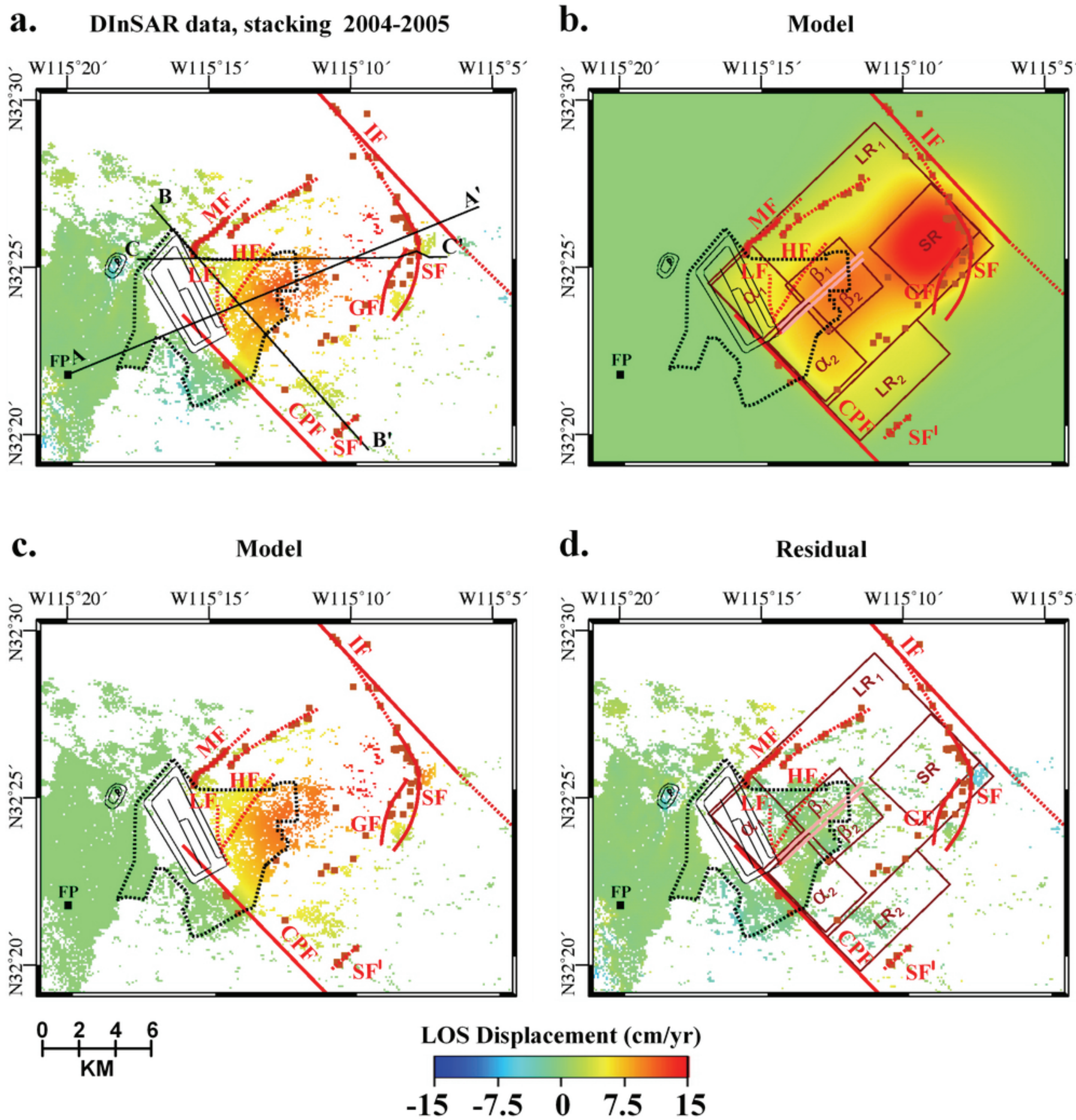

Figure 21: a. Geocoded map of LOS displacement rate (cm/yr) for December 2004-December 2005 period obtained using the stacking technique. b and c. Best-fit model predicted LOS displacements. d. Residuals between observed (a) and predicted (b) LOS displacements. Areas of low coherence (<0.1) are masked in a, b, and d. FP is the fixed point. The black dotted line frames the limits of the CPGF. The black lines correspond to the profiles A-A', B-B' and C-C' illustrated in Figures 22-24. Brown rectangles in b and d show the tensional rectangular fractures of the best-fit model (Table V). Faults notation is as in Figure 16.

Figura 21: a. Mapa geocodificado de velocidad de desplazamiento LOS (cm/año) para el periodo de Diciembre 2004 – Diciembre 2005 obtenido usando la técnica de apilamiento. b y c. Desplazamiento LOS predicho por el modelo de mejor ajuste. d. Residuo entre desplazamiento LOS observado (a) y modelado (b). Las áreas de baja coherencia (<0.1)

están enmascaradas en a, b y d. FP es el punto fijo. La línea negra punteada enmarca los límites del CPGF. Las líneas negras corresponden a los perfiles A-A', B-B' y C-C' mostrados en las Figuras 22-24. Rectángulos cafés en b y d muestran fracturas tensionales rectangulares del modelo de mejor ajuste (Tabla V). Notación de fallas como en la Figura 16.

IV.3 Modeling of DInSAR data.

As it was mentioned above, the subsidence indicates volume contraction within the reservoir. It seems appropriate, therefore, to attempt to model the surface deformation with volume change at depth. Mathematical models initially used in vulcanology and hydrofracturing theory are now widely applied to predict the deformation caused by the extraction of fluids. Perhaps the model most commonly used is Mogi's (1958) model in which a series of idealized point-sources are imbedded within an elastic half-space. This model was used by Mossop and Segall (1997) to model subsidence in the Geysers geothermal field, and by Carnec and Fabriol (1999) and Hansen (2001) to model subsidence in the CPGF. Another model frequently used is the model of deflation of a triaxial ellipsoidal cavity in an elastic half-space (Davis, 1986). It was used in the modeling of the subsidence in the Coso geothermal field (Fialko and Simons, 2000). More realistic models are those of Segall (1989) and Walsh (2002) that use a poroelastic framework and slightly more complicated reservoir geometry.

However, none of the models previously discussed seem to address several of the complexities presented in the CPGF. The detailed description of each of these models, including deficiencies and advantages for the subsidence modeling in the CPGF, is given by Sarychikhina (2003).

The CPGF reservoirs are located in tilted sedimentary layers and bounded by faults. At any rate, the mathematical model of rectangular tensional fractures (Yang and Davis, 1986) seems to be the one that captures the best the geometry of the CPGF reservoirs. This model was used by Sarychikhina (2003) and Glowacka *et al.* (2005) to model subsidence in the CPGF detected by 1994-1997 leveling surveys. Each fracture is characterized by a series of geometrical parameters such as its center location (*x, y, z*), length (*L*), width (*W*), azimuth (*Azm.*), dip (*Ang.*) and closure (*p*). Note that the rectangular tensile fracture has zero thickness that volume reduction is achieved by fracture closure or disappearance of material on the fracture plane. The resulting model was described in the chapter II.4 and is based in a hydrological model of the field (Halfman e*t al.,* 1984; Lippmann *et al.*, 1991). The modeling was done by trial and error using Coulomb 2.0 software (King *et al.*, 1994; Toda *et al.,* 1998).

For the 2004-2005 DInSAR data, a forward model similar to one described above was applied to find the rectangular tensional fractures that fit the best the observed LOS displacement field. The modeling was performed using the Coulomb 3.1 software. Initial parameters were based on the 1994-1997 leveling data model (Sarychikhina, 2003; Glowacka *et al.*, 2005), hydrological model of the CPGF (Halfman e*t al.,* 1984; Lippmann *et al.*, 1991), and data of surface fissures and faults from geological surveys (González *et al.*, 1998; Glowacka *et al.*, 2006, 2010; Suárez-Vidal *et al.*, 2008). The calculated vertical, D_U, easting, D_E, and northing, D_N, components of the surface displacement vector were converted into line-of-sight displacement (i.e. range change, ΔR,) during the modeling using the expression for a LOS acquired in a right looking direction in a descending track (Fialko *et al.*, 2001), which is:

$$\begin{bmatrix} -\cos(\theta) & -\sin(\theta)\cos(\alpha) & \sin(\theta)\sin(\alpha) \end{bmatrix} \begin{bmatrix} D_U \\ D_E \\ D_N \end{bmatrix} = \begin{bmatrix} \Delta R \end{bmatrix}, \tag{23}$$

where θ and α are the look angle and azimuth of the satellite heading vector, respectively. The synthetic LOS displacement field was compared with the observed LOS displacement data.

The parameters of the best-fit model are presented in Table V. The best fit model consists of four closing fractures, two of which correspond to geothermal reservoirs, divided by the normal SE-dipping fault H into two blocks: α (α_1 and α_2) and β (β_1 and β_2). Three remaining fractures correspond to recharge aquifers: *SR* (small recharge) and *LR* (large recharge) with *LR'* as its continuation.

The calculated LOS displacements are shown in Figure 21b with the rectangular tensional fracture corresponding to the best fitting solution. Figure 21c shows the predicted LOS displacement field with superimposed DInSAR low coherence data mask. Figure 21d shows a residual after subtracting the best fitting model from the data, and Figures 22-24 show three profiles across the subsidence zone with the observed and modeled LOS displacements. As one can see from Figures 21-24, both shape and magnitude of the modeled surface LOS displacement are quite similar to the observed ones; the absolute value of the residual at most observation points is about 0.0 – 1 cm /yr, although local discrepancies show as much as 5 cm/yr. The nature of these local discrepancies is discussed in the next section. The best-fit model gives a RMS of 1 cm.

While the initial model was based on the 1994-1997 model, the final best-fit model differs from that one. First, more fractures were applied to fit the data. The α reservoir was divided into two blocks with different fracture closures, a feature that is in agreement with hydrological and geological models of the CPGF. *LR'* was added to *LR* recharge aquifer to model the complex form of the subsidence pattern in the southern zone. There were not leveling benchmarks in this zone in 1994-1997 therefore the DInSAR data reveal better the subsidence extension in this direction. The depth of *SR* fracture centre was increased from 1500 to 2800 m, first, to be in better agreement with geological model and, second, to explain the depth range of slip events proposed by Glowacka *et al.* (2010).

Fracture	Model Fractures Parameters									Volume change m^3/yr	
								P* (m)			
	X_0 (m)	Y_0 (m)	Z_0 (m)	L (m)	W (m)	Azm. (°)	Ang. (°)	94-97	2005	94-97	2005
α_1	664224	3586226	1028	4142	3151	136	1	0.075	0.015	9.8E+05	2.0E+05
α_2	667518	3582923	1448	4569	3151	136	1	0.035	0.035	5.0E+05	5.0E+05
β_1	667739	3587407	2060	1435	4014	138.5	4	0.12	0.12	6.9E+05	6.9E+05
β_2	669054	3585919	2460	1836	4014	138.5	4	0.12	0.15	8.8E+05	1.1E+06
sr	673482	3589177	2800	3796	4923	134	7	0.115	0.23	2.1E+06	4.3E+06
LR1	669372	3587781	862	9474	12778	136	1	0.04	0.04	4.8E+06	4.8E+06
LR2	671460	3581382	810	2624	6876	136	1	0.04	0.04	7.2E+05	7.2E+05
									Total	1.1E+07	1.2E+07
										< 15%	

Table V: Models fractures parameters and volume change caused by fractures closure. 94-97 is the model which fit the leveling 1994-1997 data. 2005 is the model which fit the DInSAR data. P^* is the fracture closure (positive).

Tabla V: Parámetros de las fracturas de modelos y cambio de volumen causado por el cierre de fracturas. 94-97 es el modelo-resultado de ajuste de los datos de nivelación de 1994-1997. 2005 es el modelo-resultado de ajuste de los datos de DInSAR. P^*es el cierre de fracturas (positivo)

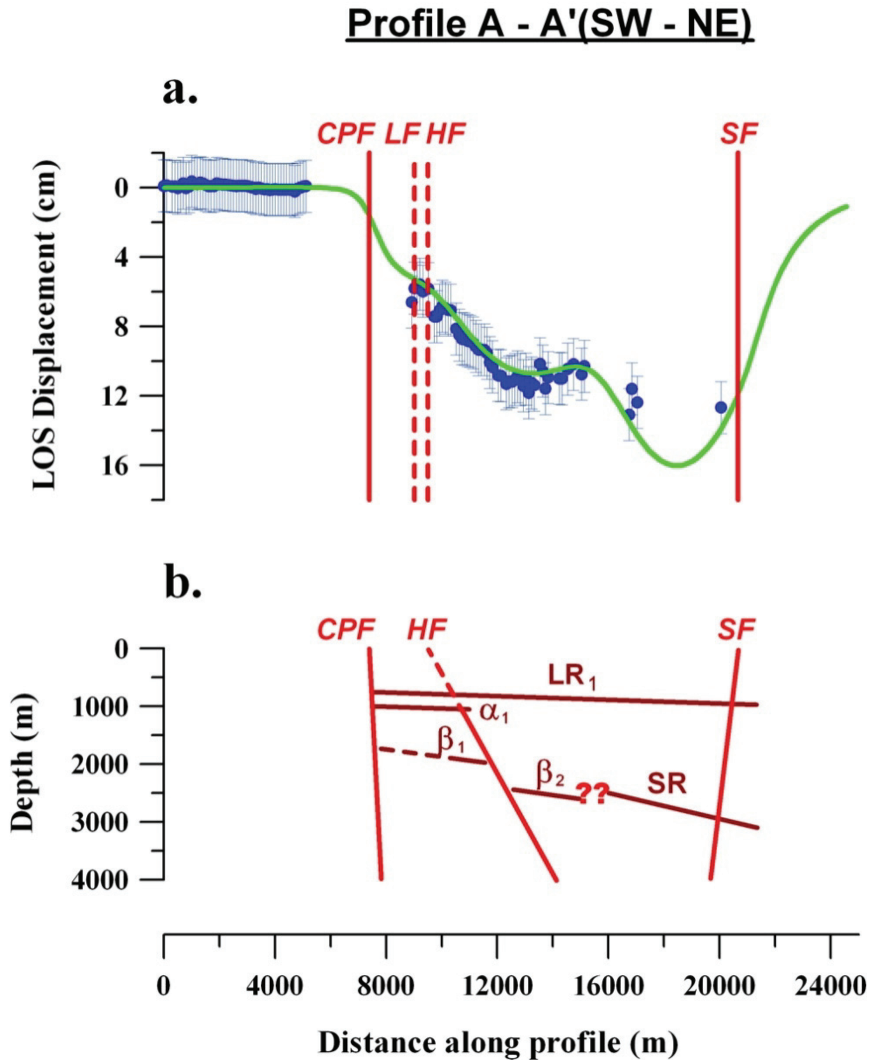

Figure 22: a. Comparison between DInSAR data (derived from interferograms stacking) and model prediction along the profile A-A'. The location of profile is presented in Figure 21a. Blue circles are DInSAR data. Error bars indicate expected LOS displacement rate estimation error of DInSAR data and is ±1.5 cm. Green solid line is best-fit model. Positive LOS displacement values indicate ground subsidence. b. Best-fit model along the profile (brown solid line). Dotted brown line shows the β1 reservoir extensions from geological data (model). Depth down is positive. Faults notation is as in Figure 16. The HF is shown with solid red line in the depths of α and β reservoirs because its trace is well known in those depths from wells data. Interrogation symbols represent the unknown but expected structural limit based on observed subsidence pattern and results of modeling.

Figura 22: Comparación entre datos de DInSAR (derivados del apilamiento de interferogramas) y predicciones del modelo a lo largo de perfile A-A'. La localización del perfil está presentada en Figura 21a. Los círculos azules representan los datos de DInSAR. Las barras de error indican el error esperado de la estimación del desplazamiento LOS de los datos de DInSAR y es de ±1.5 cm. La línea solida verde es el modelo del mejor ajuste.

Valores positivos de desplazamiento LOS indican el hundimiento de la superficie. b. Modelo de mejor ajuste a lo largo del perfil (líneas cafés). La línea café discontinua muestra la extensión de reservorio β_1 de los datos (modelo) geológicos. Profundidad hacia abajo es positiva. Notación de fallas como en la Figura 16. Falla H está representada con la línea roja solida en las profundidades de los reservorios α y β debido a que su traza en estas profundidades es bien conocida de los datos de pozos. Los signos de interrogación representan un límite estructural desconocido pero esperado basando en el patrón de la subsidencia observada y resultados de modelación.

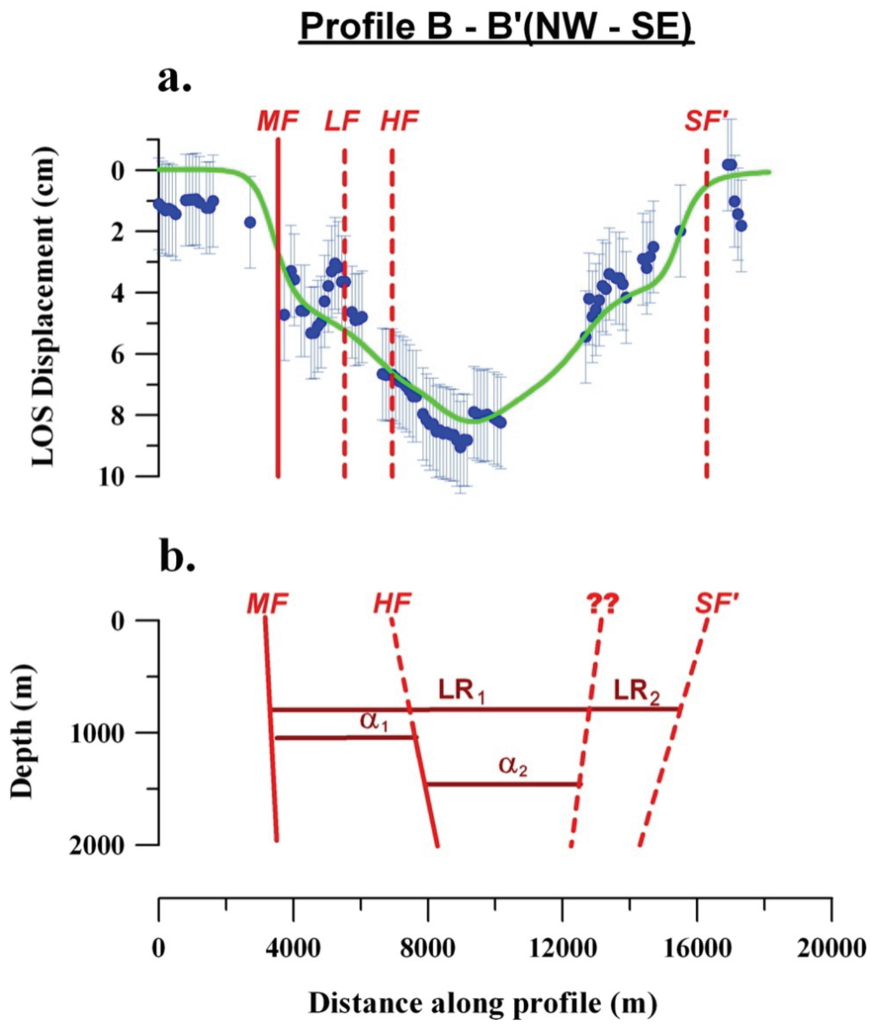

Figure 23: a. Comparison between DInSAR data (derived from interferograms stacking) and model prediction along the profile B-B'. b. Best-fit model along the profile. The location of profile is presented in Figure 21a. Interrogation symbols represent the unknown but expected fault based on observed subsidence pattern and results of modeling. Notation is as in Figure 22.

Figura 23: a. Comparación entre datos de DInSAR (derivados del apilamiento de interferogramas) y predicciones del modelo a lo largo de perfile B-B'. b. Modelo de mejor

ajuste a lo largo del perfil. La localización del perfil está presentada en Figura 21a. Los signos de interrogación representan una falla desconocida pero esperada basando en el patrón de la subsidencia observada y resultados de modelación. Notación es como en la Figura 22.

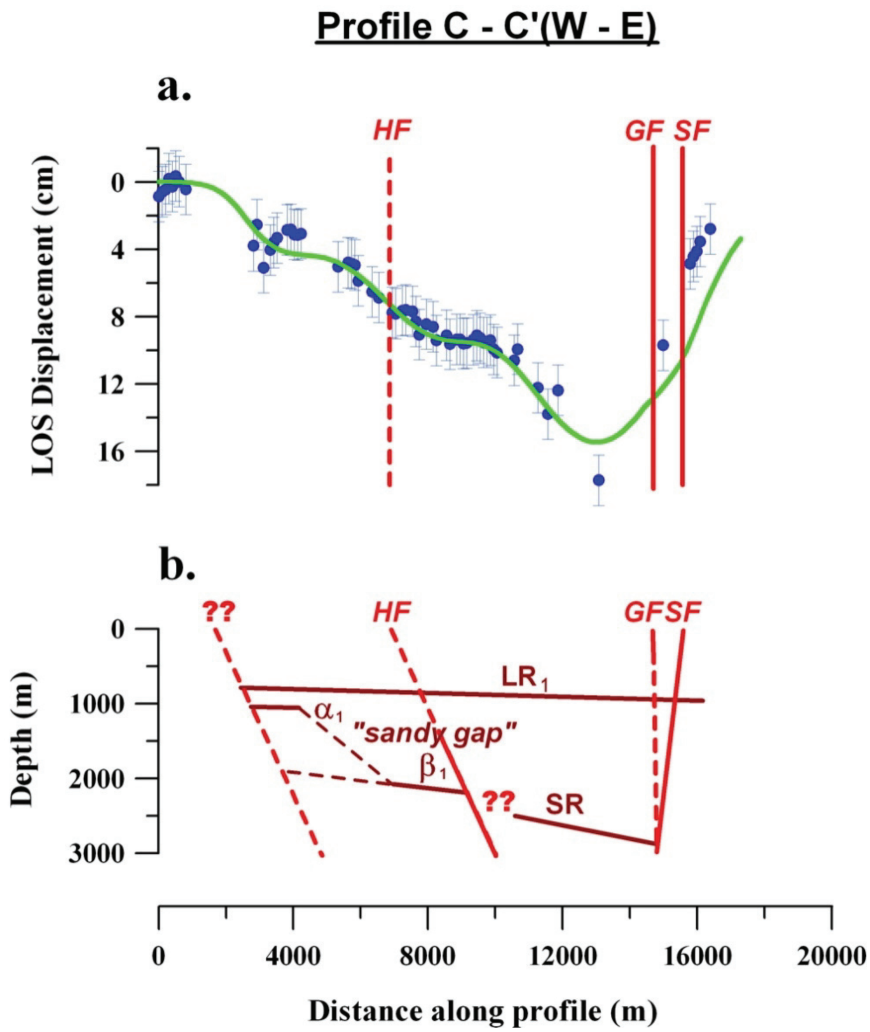

Figure 24: a. Comparison between DInSAR data (derived from interferograms stacking) and model prediction along the profile B-B'. b. Best-fit model along the profile. The location of profile is presented in Figure 21a. Interrogation symbols represent the unknown but expected fault and structural limit based on observed subsidence pattern and results of modeling. Notation is as in Figure 22.

Figura 24: a. Comparación entre datos de DInSAR (derivados del apilamiento de interferogramas) y predicciones del modelo a lo largo de perfile C-C'. b. Modelo de mejor ajuste a lo largo del perfil. La localización del perfil está presentada en Figura 21a. Los signos de interrogación representan una falla y un límite estructural desconocidos pero esperados basando en el patrón de la subsidencia observada y resultados de modelación. Notación es como en la Figura 22.

IV.4 Comparison of leveling surveys with DInSAR data.

The deformation rate obtained by the DInSAR stacking method was compared with 1994-1997 and 1997-2006 leveling results (Glowacka *et al.*, 1999, 2006), in order to evaluate the changes in the spatial pattern and rate of land subsidence. The velocity contour maps in cm/yr from the leveling data, projected to the LOS direction using equation (21) and considering only vertical displacement component, are shown in Figure 25a and b. The contours were obtained by interpolation of the data using the Kriging algorithm. The leveling data from the 1994-1997 survey was referenced to the fixed point for 1997-2006 survey (10037). The 1994-1997 leveling survey shows a maximum LOS displacement rate of ~10 cm/yr in the center of the CPGF production zone and ~8 cm/yr in the recharge zone (Figure 25a). The 1997-2006 leveling survey evidences an increase in LOS displacement rate in the recharge area reaching a value of ~12 cm/yr (Figure 25b). However, note that the LOS displacement rate in the production CPGF zone decreased to ~9 cm/yr in the same period. It is likely that this reduction in the subsidence rate is an artifact in the interpolation caused by the loss of a number of benchmarks in that area over the years (Figure 25a and b).

The velocity contour plot in cm/yr from DInSAR data is illustrated in Figure 25c. Figure 26 gives a comparison of DInSAR-derived profiles with the surveys data (leveling 1994-1997; 1997-2006). Figures 25 and 26 reveal that the subsidence in the recharge zone increased by a factor of ~1.5 between 1997 and 2005. The maximum subsidence magnitude in the CPGF extraction zone did not change during this period; however, its locus migrated to the northeast. To ensure that the observed changes in the LOS displacement pattern are actual effects and not the effects of the different techniques used, the velocity contour map from DInSAR data of only the pixels in location of 1994-1997 leveling benchmarks was drawn (Figure 25d). In case the value of a pixel could not be determined, the value from nearest pixel (distance less than 500m) was taken instead. Total number of 64 values was used. The results suggest that the observed changes in pattern and rate of subsidence are real.

Next I proceeded to verify the robustness of the model obtained in section IV.3. I did so by changing the closure of the fractures of the model to see if I could reproduce the 1994-1997 leveling data. The rationale behind this idea is that, of course, the same set of fractures is responsible for the subsidence in the study area at different time. The results are shown in Figure 27 and the parameters of model are shown in the Table V. The best fit model has a RMS of 1 cm/yr. The residuals in most of the leveling benchmarks range between 0 and 2 cm/yr. However, large residuals, up to 4 cm/yr, are observed in three benchmarks located in the western border of evaporation pond. The leveling data suggests that this zone is subsiding; whereas the DInSAR suggests that this zone is practically stable (Figures 25 and 26). There is not measurement from those benchmarks from leveling survey 1997-2006 to determine the possible origin of this discrepancy. However, a differential interferogram obtained by Carnec and Fabriol (1999) using ERS 1 images acquired in 16/12/1995 and 04/05/1996 clearly shows that this zone is practically stable. Based on this result the more likely explanation of observed discrepancy is the possible unreported restoration work done on those benchmarks during the frequent reparations of the evaporation pond borders. As no confirmation of this is available, it may also be due to a subsurface effect such as change in the hydrological regime. Additional analysis of archived ERS 1/2 SAR images for 1994-2005 period is required to address this point.

In the calculations it was assumed that the change in volume of every particular fracture of both best-fit models is equivalent to the volume removed from (or added to) the fracture (and ignoring compaction effects which are difficult to constrain). With this assumption, using the estimated values of the fracture dimensions and their closure, the volume change in the reservoirs and aquifers was evaluated for two periods: 1994-1997 and 2004-2005 (Table V). From Table V it can be seen that volume change in 2005 period is ~15% more than for 1994-1997 which is comparable with net extraction (extraction-injection) change which is about 18% larger for 2005 period comparing with net extraction in 1994-1997 (Figure 28).

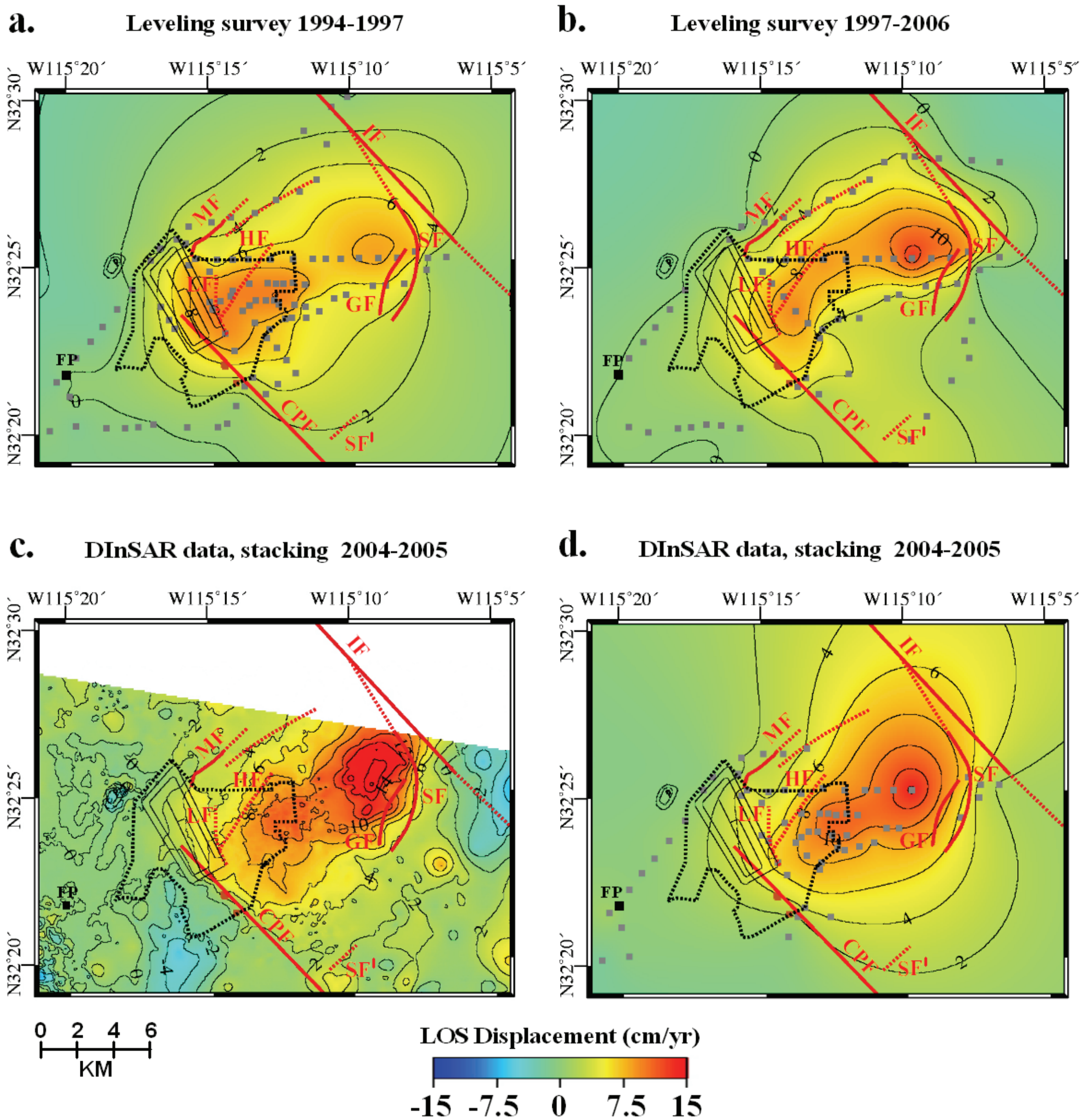

Figure 25: Contour maps of LOS displacement velocity (cm/yr) obtained using data from leveling surveys 1994-1997 (a) and 1997-2006 (b), and DInSAR stacking 2004-2005 (c & d).The contours were obtained by interpolation of the data using the Kriging algorithm. Contouring of DInSAR stacking data was performed using the value of all pixels with coherence >0.1 (c) and only these in location of the 1994-1997 leveling benchmarks (d). FP is the fixed point. The black dotted line frames the limits of the CPGF. The gray squares are location of benchmarks used for interpolation and contouring. Faults notation is as in Figure 16.

Figura 25: Mapas de contornos de velocidad de desplazamiento LOS (cm/año) obtenidos de datos de nivelación de 1994-1997 (a) y 1997-2006 (b), y DInSAR usando la técnica de apilamiento 2004-2005 (c y d). Los contornos fueron obtenidos por la interpolación de los datos usando el algoritmo de Kriging. El trazado de las líneas de contornos de datos de

DInSAR fue realizado usando los valores de todos los pixeles con coherencia > 0.1 (c) y solo en localización de bases de nivelación de 1994-1997 (d). FP es el punto fijo. La línea negra punteada enmarca los límites del CPGF. Los cuadrados grises son las bases usados para la interpolación y creación de contornos. Notación de fallas como en la Figura 16.

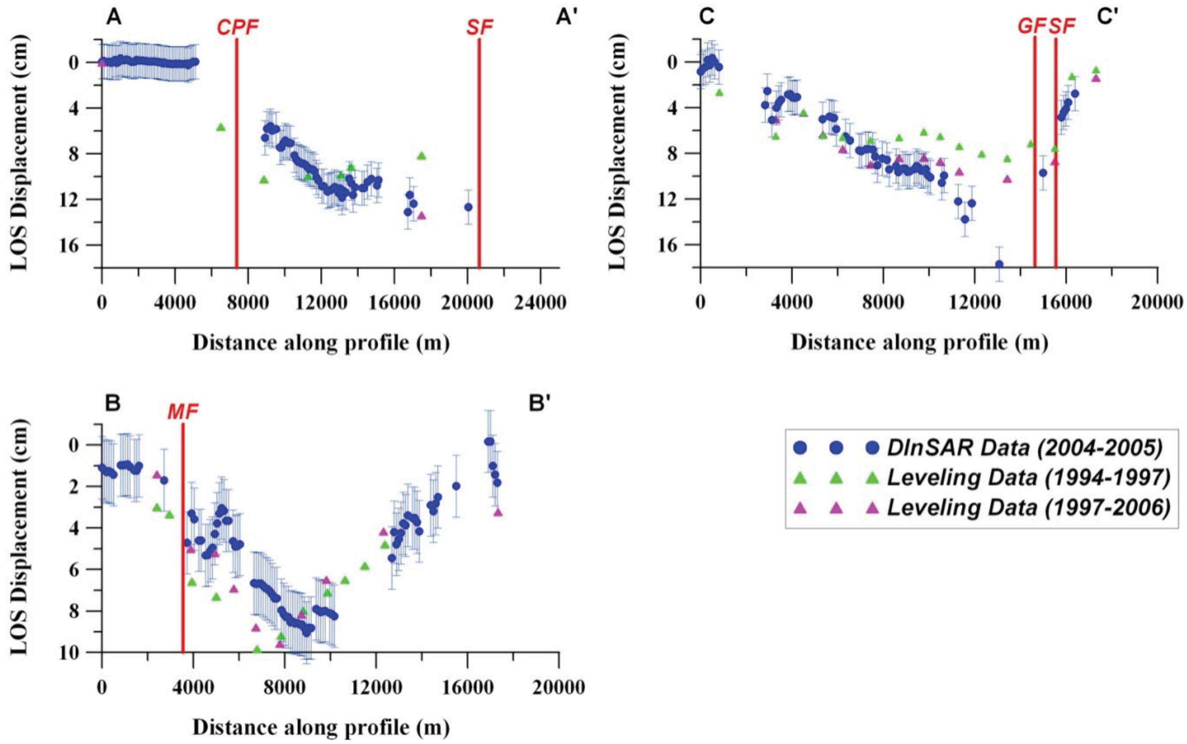

Figure 26: Comparison between DInSAR 2004-2005 data (derived from interferograms stacking) and ground survey data from 1994-1997 and 1997-2006 periods along the profiles A-A', B-B' and C-C'. The location of each profile corresponds to black lines in Figure 21a. Ground survey data are projected to the LOS direction. Positive LOS displacement values indicate ground subsidence. Error bars indicate expected LOS displacement rate estimation error of DInSAR data and is ±1.5 cm. Solid red lines represent the faults with known surface traces: MF=Morelia fault, CPF=Cerro Prieto, SF=Saltillo fault, GF=Guerrero fault.

Figura 26: Comparación entre datos de DInSAR de 2004-2005 (derivados de apilamiento de interferogramas) y datos de nivelación de 1994-1997 y 1997-2006 a lo largo de perfiles A-A', B-B', C-C'. La localización de cada perfil se presenta como línea negra en Figura 21a. Los datos de nivelación están proyectados a la dirección de LOS. Valores positivos de desplazamiento LOS indican el hundimiento de la superficie. Las barras de error indican el error esperado de la estimación del desplazamiento LOS de los datos de DInSAR y es de ±1.5 cm. Línea roja solida representa las fallas con trazas superficiales conocidas: MF=falla Morelia, CPF=falla Cerro Prieto, SF=falla Saltillo, GF=falla Guerrero.

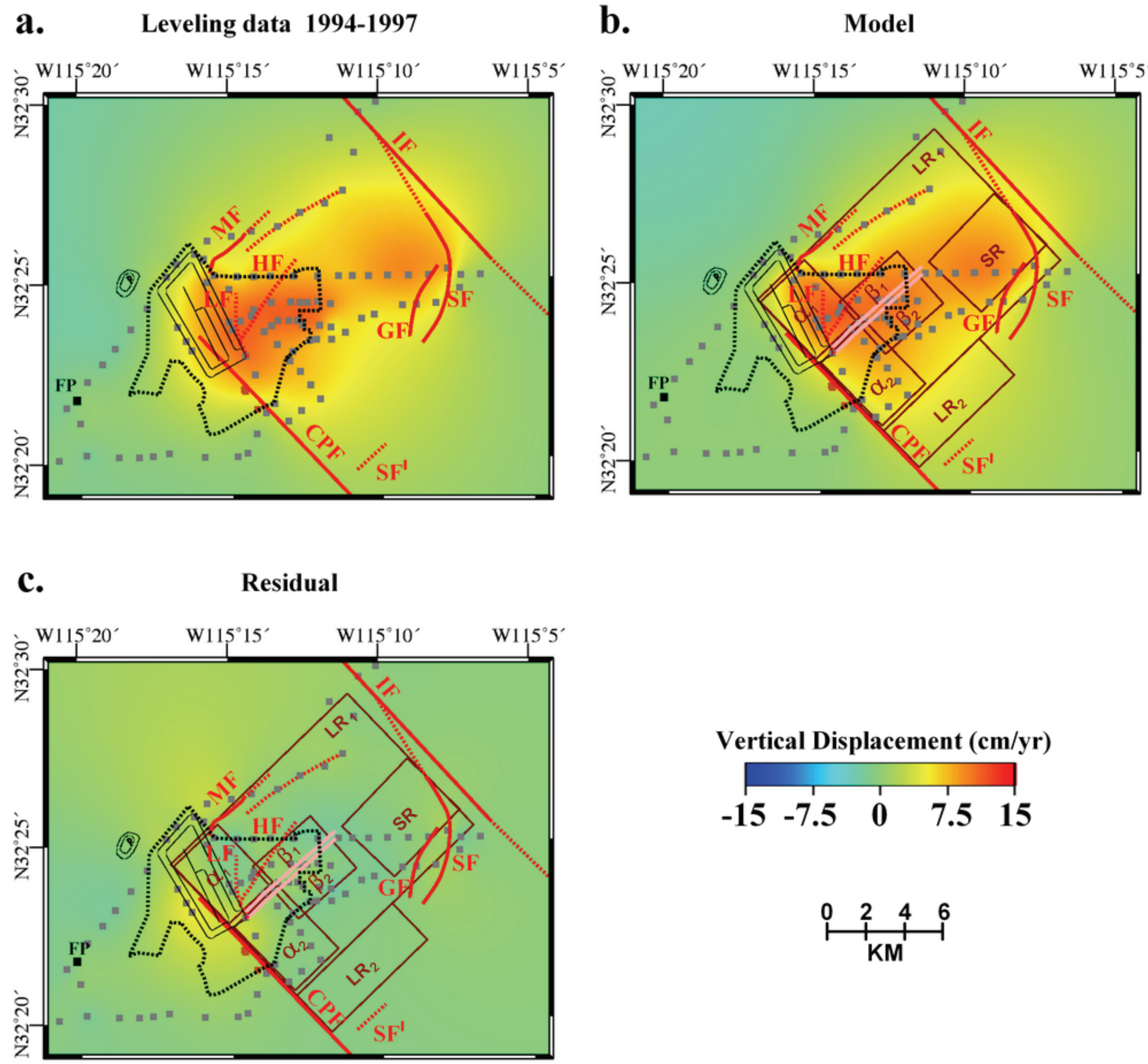

Figure 27: Vertical displacement from leveling surveys 1994-1997 (a) and predicted by the best-fit model (b). c. Residuals between observed (a) and predicted (b) vertical displacements. FP is the fixed point. The gray squares are leveling benchmarks. The black dotted line frames the limits of the CPGF. Brown rectangles in b and c show the tensional rectangular fractures of the best-fit model. Faults notation is as in Figure 16.

Figura 27: a. Desplazamiento vertical de nivelación de 1994-1997 (a) y predicho por el modelo de mejor ajuste (b). c. Residuo entre el desplazamiento vertical observado (a) y modelado (b). Rectángulos cafés en b y c muestran fracturas tensionales rectangulares del modelo de mejor ajuste. FP es el punto fijo. La línea negra punteada enmarca los límites del CPGF. Los cuadrados grises son las bases de nivelación. Notación de fallas como en la Figura 16.

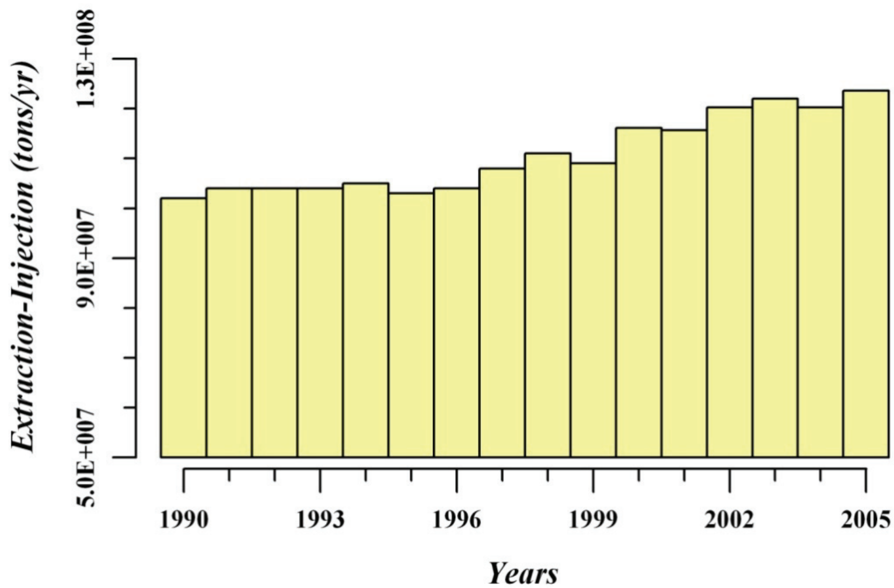

Figure 28: Net extraction (extraction-injection) evolution in CPGF at last 15 years (modified from page 27, CFE (2006)).

Figura 28: Evolución de la extracción neta (extracción-inyección) en el CPGF en los últimos 15 años (modificado de la pagina 27, CFE (2006)).

IV.5 Results and discussion

In this chapter, a differential interferometric analysis of space-borne Envisat SAR was conducted to map the extent and pattern of the anthropogenic subsidence of the Mexicali Valley. The differential interferograms clearly show a deformation signal with a time span of up to 1 year. However, the temporal decorrelation increases considerably for the interferometric pairs that span more than three months in the areas covered by agricultural fields around the CPGF. It makes the DInSAR phase of long time period interferograms difficult to measure and unwrap. On the other hand, the atmospheric distortion in the interferogram spanning short time period, theoretically, could reach up to 50%. For this reason, a single short time spanning interferogram is not an accurate measurement. Visual analysis of a series of single short time interferogramas was performed in an attempt to distinguish the deformation signal from atmospheric noise. The stacking of 4 successive short time spanning interferograms was also performed in order to obtain the long time period interferogram and reduce the atmospheric noise. The resulting from stacking interferogram covers December 2004–December 2005 period. The estimated accuracy of DInSAR LOS displacement data derived from the stacking is ±1.5 cm. The analysis of DInSAR data from ascending and descending tracks, and ground based data shows that the DInSAR LOS deformation signal is mainly due to land subsidence. The analysis of DInSAR data (series of single interferograms and stacked interferogram) shows that the radar data provided a detailed mapping of both the amplitude and spatial extent of land subsidence in the study area. DInSAR observations reveal that the total area of ground deformation appears as a roughly NE-SW oriented elliptical-shaped feature with two bowls exhibiting high LOS deformation rates in the December 2004–December 2005 period: ~16 cm/yr in the recharge zone (east – northeast of the study area) and ~10 cm/yr below in the east boundary of CPGF production zone, which corresponds to ~17 cm/yr and ~11 cm/yr of subsidence, respectively. The DInSAR mapping also confirms that the tectonic faults control the spatial extent of the observed subsidence, and constitute, probably, groundwater flow barriers for aquifers/reservoirs. The shape of subsiding area also correlates with Cerro Prieto pull-apart basin (Suárez-Vidal *et al.,* 2008).

Several individual interferograms revealed a small zone with change in range south to the evaporation pond. The sign of this change varies for different interferograms. The changes in range in the same geographic location were observed earlier by Carnec and Fabriol (1999) and Hansen (2001). These authors gave different explanations for the observed signals. Carnec and Fabriol (1999) attributed this range change to ground deformation caused by reinjection, and Hansen (2001) interpreted this signal as atmospheric error. More detailed geodesic and geophysical studies are necessary to clarify the origin of this range change.

The DInSAR LOS displacement was modeled using a series of rectangular tensional fractures embedded in an elastic half-space. The model is based on hydrological model of the CPGF and includes the information of rupture and fissure zones from geological survey and wells data. The final model consists of seven rectangular fractures. Four of them correspond to geothermal reservoirs; the remaining three represent recharge aquifers. Comparison of the observed and modeled surface displacements shows a reasonable agreement. The discrepancies between the model and the DInSAR data are around 0-6 cm/yr. An area with large residuals is located in the eastern block of the Saltillo fault, which is considered as a fluid flow barrier and subsidence boundary. This fault has a curved shape what is impossible to model with the applied model of rectangular tensional fracture.

Figures 22-24 b present the structure of the best-fit model and location of the known and proposed faults along three profiles. The best-fit model confirms the strong controlling role of tectonic faults in anthropogenic subsidence because they bound the contracting reservoirs and aquifers. Along the profiles shown in the Figures 22-24 two unknown but expected faults are traced based on observed subsidence pattern and/or results of modeling. The location of these faults (or fault zones) is shown in Figure 29. The first proposed fault appears to limit the subsiding area to the northwest (Figure 24b). As this area corresponds to the evaporation pond where the loss of coherence in DInSAR data is observed and it is impossible to perform geologic and leveling survey, this limit could be attributed to Cerro Prieto fault, Morelia fault or unknown fault (Figure 29). The second proposed fault limits the α_2 reservoir to the south and could be one of several normal faults, oblique to the major faults, of the Cerro Prieto pull-apart basin (Figure 23b and 29). This fault does not rupture the surface. However, the ground fissuring in this zone is additional evidence of a sub-surface fault. The best-fit model and the observed subsidence pattern also suggest the existence of other buried structures within and below the aquifer-bearing sedimentary basin fill, between the eastern edge of CPGF (β_1 and β_2 reservoirs from the model) and the recharge zone (*SR* aquifer from the model, see also Figures 22b and 24b). This structure appears to have linear form, parallel to the principal faults: the Cerro Prieto and the Imperial faults (Figure 29). Aydin and Nur (1982) proposed a model of pull-apart basin formation in which the similar structure is formed, approximately in the middle of the extensional zone. Therefore, the origin of the observed structure is tectonic. However it is difficult to determine if this limit between two subsidence basins is only stratigraphic or also represents a faulting zone.

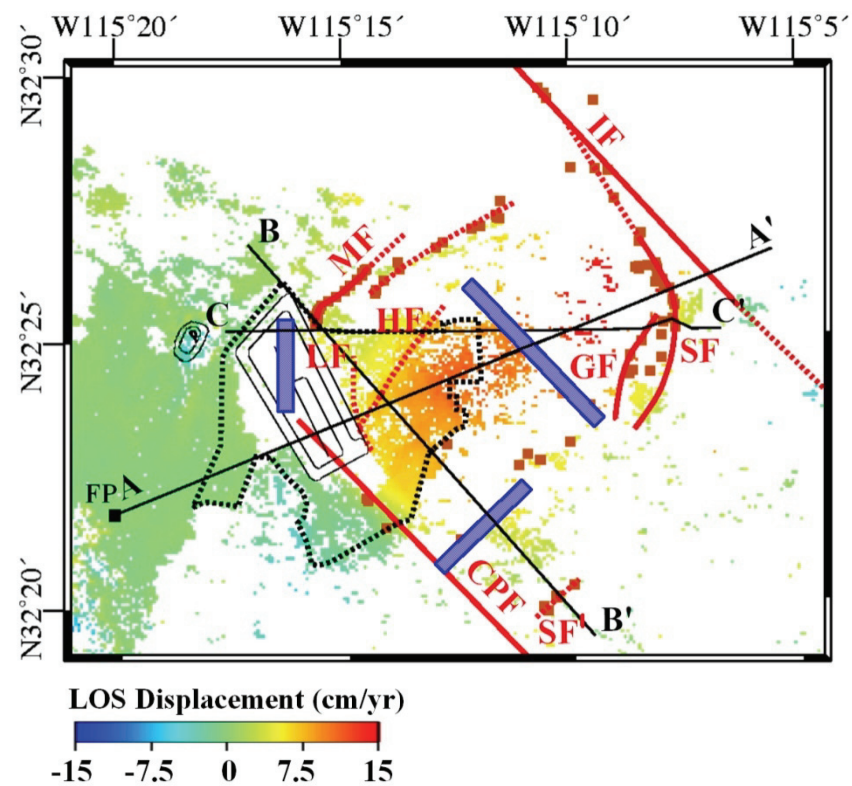

Figure 29: The spatial localization of unknown but expected based on observed subsidence pattern and/or results of modeling faults or structural limits (blue rectangles). DInSAR stacking data (2004-2005) with masked areas of low coherence (<0.1) are shown as background. FP is the fixed point. The black dotted line frames the limits of the CPGF. The black lines corresponds to the profiles A-A', B-B' and C-C' illustrated in Figures 22-24. Faults notation is as in Figure 16.

Figura 29: La localización especial de fallas o límites estructurales desconocidos pero esperados basando en el patrón de la subsidencia observada y/o resultados de modelación (rectángulos azules). Datos de apilamiento de DInSAR (2004-2005) con áreas de baja coherencia (<0.1) enmascaradas se presenta como fondo. La línea negra punteada enmarca los límites del CPGF. Las líneas negras corresponden a los perfiles A-A', B-B' y C-C' mostrados en las Figuras 22-24. Notación de fallas como en la Figura 16.

A comparison of the deformation rates obtained using different techniques and time intervals indicate that the average rate of deformation has increased since 1997. The maximum increase of deformation rate is observed in the recharge zone. The center of deformation in the CPGF production zone is migrating to the northeast. These results suggest that the land subsidence in the study area is a dynamical process. The changes in the ground deformation pattern may be caused by production increase in the CPGF due to the newest power plant (CP IV) which started operating in 2000 in the eastern part of field, as was suggested by Sarychikhina *et al*., 2007 and Glowacka *et al.*, 2010. Since the electricity production at the CPGF is an indispensable part of Baja California economy, economic pressure will result in future increase of extraction rate and field limits expansion and consequently, increased subsidence rate and its extension area. So the evaluation of geological hazard due to subsidence process is required for Mexicali Valley area. For this, several scenarios of CPGF development need to be taken into account to predict the subsidence and its environmental impact.

Besides the strong ground deformation, the geothermal fluid exploitation in the CPGF can affect the crustal stresses and trigger earthquakes, as was presented in the chapter II.3. Several studies showed the correlation of seismicity in space and time with production (Majer and McEvilly, 1982; Glowacka and Nava, 1996; Fabriol and Munguía, 1997; Glowacka *et al.*, 2005). To investigate if the production increase described here and north-east migration affect the seismicity pattern the RESNOM (Red Sísmica de Noroeste de Mexico), seismic network of northwest of Mexico, earthquakes catalog was used. The threshold magnitude of completely reported events was considered to be M=3.0 based on studies of Frez and González (1991) and Glowacka and Nava (1996). The earthquakes of M≥3.0 and M ≥4.0 which occurred in the area defined in the Figure 30a in the 1990-2005 period were analyzed. Figure 30b shows the number of earthquake per year. Without taking into account the exceptionally large number of earthquakes in 2002 (related with February, 2002 seismic swarm), it is not clear if the increase of number of earthquakes of M 3.0 and M 4.0 since 2000 took place. As the predominant part of triggered by geothermal production earthquakes are microearthquakes with M<3.0, the vast majority of triggered event was, probably, not included in this analysis due to catalog lower threshold magnitude. The location of earthquakes was also analyzed. However the location error of more than ±2 km did not allow to obtain clear results. It is evident that the microseismic monitoring study with more precise epicenters location is required. This microseismic monitoring would provide some warning of changes in patterns of seismicity related to changes in the geothermal production and changes in stress field thus providing useful information for seismic hazard assessment and monitoring of reservoir dynamics.

a.

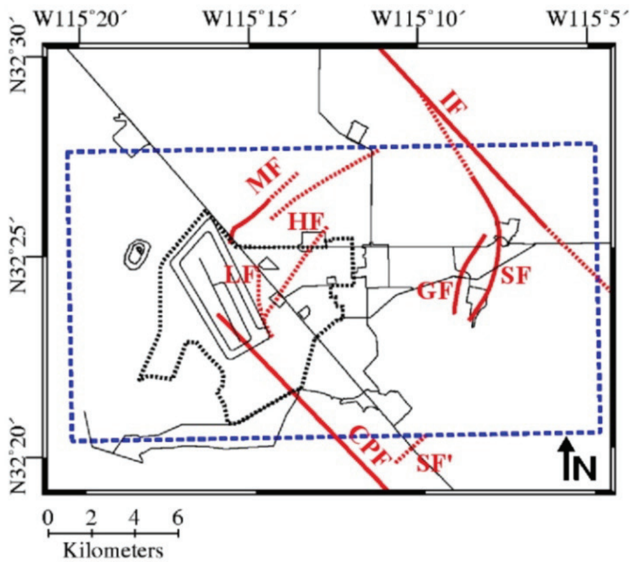

b.

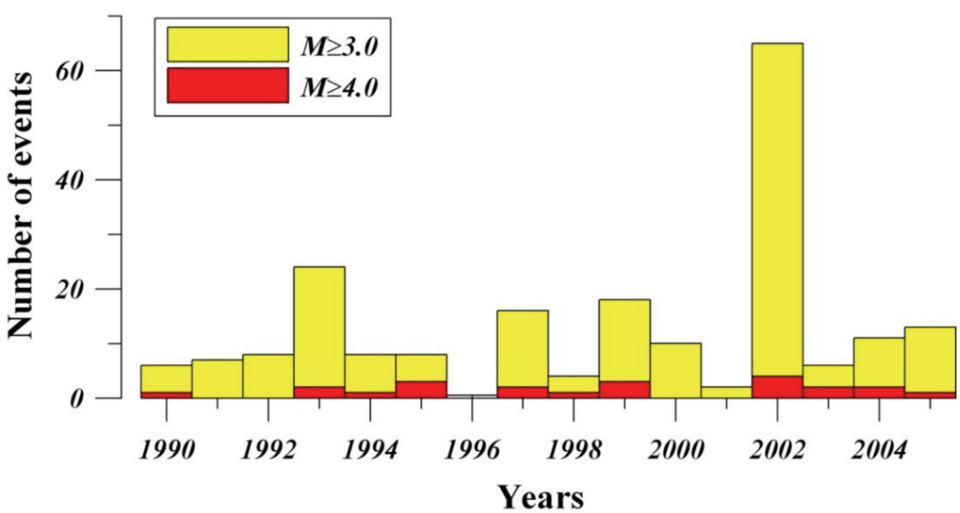

Figure 30: Analysis of seismicity and geothermal production correlation. a. The area of analyzed earthquake occurrence (dotted blue rectangle). The plan of the study area with principal roads, villages and features (as Cerro Prieto volcano and evaporation pond) (solid black line) are shown as background. The black dotted line frames the limits of the CPGF. Faults notation is as in Figure 16. b. Number of earthquakes per year.

Figura 30: Análisis de correlación entre sismicidad y producción geotérmica. a. Área de ocurrencia de sismos analizados (línea azul discontinua). El plan del área de estudio con principales caminos, poblados y características (tales como Volcán Cerro Prieto y laguna de evaporación) se muestra como fondo. La línea negra punteada enmarca los límites del CPGF. Notación de fallas como en la Figura 16. b. Número de sismos por año.

CHAPTER V

SURFACE DISPLACEMENT AND GROUNDWATER LEVEL CHANGES ASSOCIATED WITH THE MAY 24, 2006, MW5.4 MORELIA FAULT EARTHQUAKE

Part of this chapter is published in the *Bulletin of the Seismological Society of America* (BSSA). The reference of this publication is: Sarychikhina, O., E. Glowacka, R. Mellors, R. Vázquez, L. Munguía and M. Guzmán. 2009. Surface displacement and groundwater level changes associated with the 24 May 2006 Mw5.4 Morelia fault earthquake, Mexicali Valley, Baja California, Mexico. *Bull. Seism. Soc. Am.* 99(4): 2180-2189.

V.1 General Information

On 24 May 2006 at 04:20 (UTC) a moderate-size (Mw=5.4) earthquake occurred in the Mexicali Valley, Baja California, México, roughly 30 km to the southeast of the city of Mexicali (Figure 31). Locally, this earthquake was strongly felt and caused minor damage. Numerous cracks and ruptures in the surface were also created. The earthquake was recorded by local and regional seismic networks, as well as by continuously recording geotechnical instruments (crackmeters and tiltmeters) and well piezometers.

The hypocenter was located at 115.26° W, 32.41° N, at a depth of 3.6 ± 1 km (Munguía *et al.*, 2009). The epicentral error is ± 1km. This event appears to be related to the Morelia fault, which is a SE dipping normal fault that trends obliquely to the major faults in the area. The surface rupture of the earthquake (Figure 31) was about 5 km-long and showed predominantly normal faulting. The maximum vertical displacement was up to 30 cm and horizontal motion was less than 4 cm (Lira, 2006; Suárez-Vidal *et al.*, 2007). Fault plane solutions determined using teleseismic data (Table VI) show a normal dip-slip mechanism with NE-SW trending nodal planes. The surface faulting implies that the nodal plane 1, which dips SE, is the fault plane.

A foreshock of Mw=4.2 occurred just one minute and 20 seconds before the main shock, which was followed by a series of moderate and low magnitude aftershocks. Hypocentral parameters for the May 2006 Morelia earthquake sequence in the Mexicali Valley are given in Table VII (from Munguía *et al*., 2009). The hypocentral parameters of only ten aftershock events, out of the many earthquakes that were recorded locally by strong motion stations, are presented. These are the events that had the larger moment magnitudes and were recorded in three or more strong motion stations within 20 kilometers from the epicenters (Munguía *et al*., 2009). The location of the events is shown in the Figure 31.

This earthquake is of significant interest, due to its proximity to an urban area and to its surprisingly strong effects for an earthquake of such size (see Munguía *et al.*, 2009). In the following sections, an analysis of the ground deformation and of groundwater level change caused by the May 24, 2006 earthquake, as measured by a variety of ground-based and space-based techniques, is presented. The results of modeling the source fault parameters using the available surface deformation and groundwater level change data are also presented.

Table VI: Comparison of source parameters estimates for the May 24, 2006 earthquake. NP1 and NP2 refer to Nodal Plane 1 and 2 from the Centroid Moment Tensor (CMT). The fault dimensions estimates from empirical relationship (Wells and Coppersmith, 1994) are also presented. Field observations and best-fit model are from a study realized as part of this thesis.

Tabla VI: Comparación de los parámetros de la fuente estimados para el sismo de 24 de mayo de 2006. NP1 y NP2 son planos nodales de CMT (the Centroid Moment Tensor). Las estimaciones de las dimensiones de la ruptura obtenidas a partir de las ecuaciones empíricas también son presentadas. Las observaciones de campo y el modelo de mejor ajuste son un estudio realizado como parte de este trabajo de tesis.

Source		Strike (º)	Rake (º)	Dip (º)	Length (km)	Width (km)	Slip (cm)	Scalar Moment (N×m)
Global CMT	NP1	32	-89	44				1.07×10^{17}
	NP2	210	-91	46				
Wells and Coppersmith (1994) for Mw = 5.4					5	5.6		
Field observation		40 - 56			5		20-30	
Final model		48	-89	45	5.2	6.7	34	1.18×10^{17}

Table VII: Hypocenter parameters for the 24 May 2006 Morelia earthquake sequence in the Mexicali Valley (modified from Munguía et al., 2009).

Tabla VII: Parámetros hipocentrales para secuencia sísmica de 24 de mayo de 2006 en Valle de Mexicali (modificado de Munguía et al., 2009).

No	Date yyyy/m/d	Time hr:mn:s	Lat N (º)	Lon W (º)	Depth (km)	Mw
1	2006/5/24	4:19:05.5	32.4	115.28	3	4.2
2	2006/5/24	4:20:26.1	32.41	115.26	3.6	5.4
3	2006/5/24	4:25:13.3	32.41	115.22	4.6	4.1
4	2006/5/24	9:58:48.2	32.40	115.29	2.7	3.7
5	2006/5/27	9:31:20.4	32.37	115.29	3.9	3.4
6	2006/5/27	10:21:35.1	32.36	115.28	3.9	4.5
7	2006/5/27	17:03:58.3	32.37	115.3	3	3.5
8	2006/5/28	7:40:20.0	32.42	115.21	4.6	4.4
9	2006/5/28	11:55:23.2	32.42	115.22	4.1	4.6
10	2006/5/28	11:57:46.6	32.42	115.21	4.2	3.9

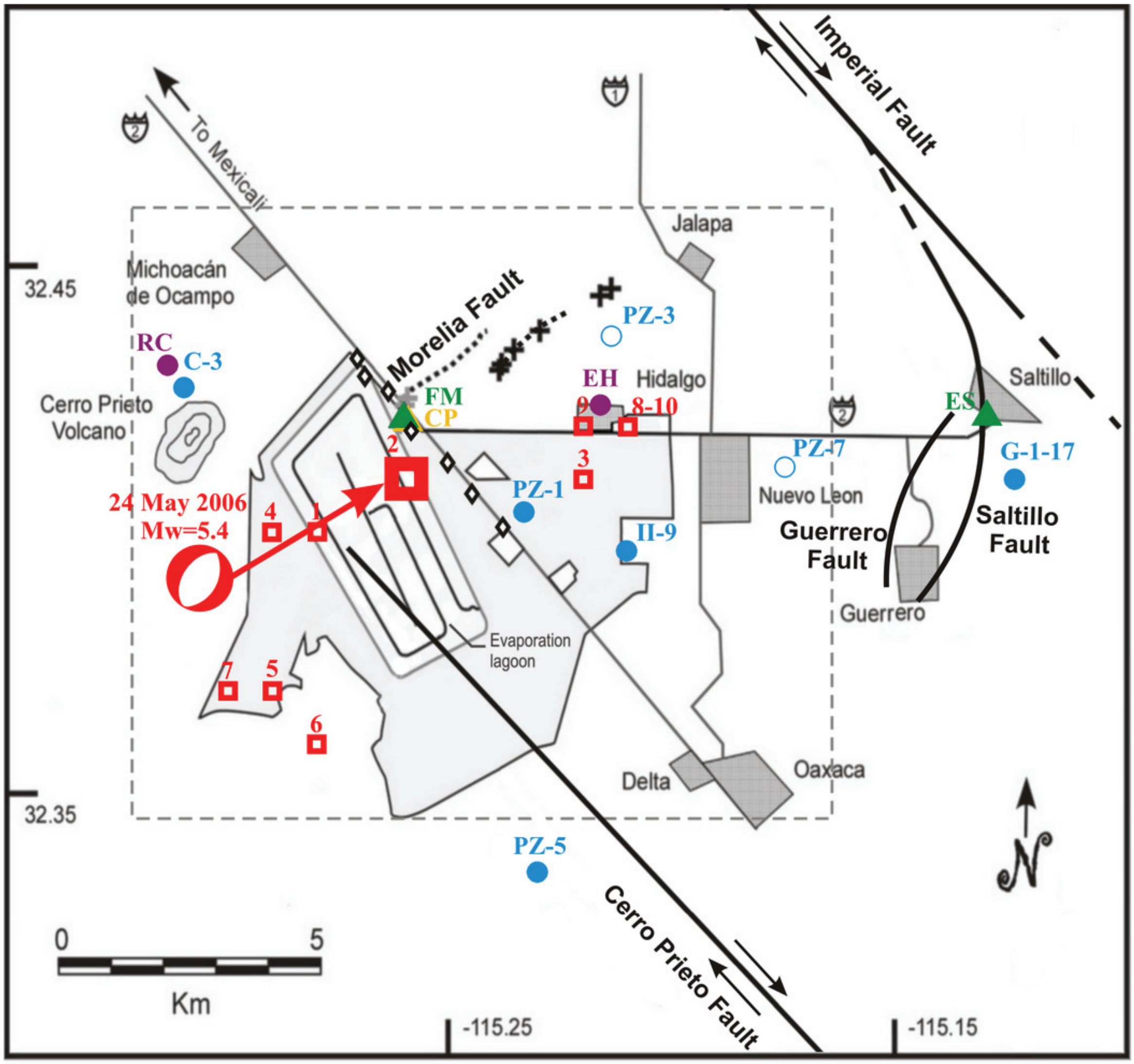

Figure 31: Map of the Mexicali Valley showing the epicenters (red squares) of the May 2006 earthquakes sequence, determined by Munguía et al. (2009). The number corresponds to the event number in Table VII. The focal mechanism (Global CMT) for the main May 24, 2006 event is shown. The main active faults in the area are presented. The green triangles indicate the location of the vertical crackmeters at the Morelia fault (FM) and the Saltillo fault (ES). The dotted line and the gray and the black crosses correspond to points at which surface faulting was observed by Lira (2006), Suárez-Vidal et al. (2007), and Sarychikhina et al. (2009) respectively. Filled and empty blue circles indicate wells showing coseismic water level rise and drop, respectively. The yellow triangle indicates the surface tiltmeter (CP). Violet circles indicate borehole tiltmeters (EH and RC). The light gray shaded area is the Cerro Prieto Geothermal Field. Dark gray shades indicate are urban areas. The dashed rectangle is the area plotted in Figures 34-35, 39.

Figura 31: Mapa del Valle de Mexicali con las localizaciones epicentrales (cuadrados), determinadas por Munguía et al. (2009), de la secuencia sísmica de Mayo de 2006. El número corresponde al número de evento en la Tabla VII. El mecanismo focal (Global CMT) para el evento principal de 24 de Mayo de 2006 se muestra en la figura. Se presentan las principales fallas activas. Los triángulos verdes son los grietómetros verticales en la falla Morelia (FM) y en la falla Saltillo (ES). La línea punteada, las cruces grises y las cruces negras corresponden a puntos en los cuales el rompimiento cosísmico de la superficie fue observado por Lira (2006), Suárez-Vidal et al. (2007), y Sarychikhina et al. (2009), respectivamente. Los círculos azules rellenos y vacios son los pozos en los cuales subida y bajada cosísmicas de nivel de agua fueron, respectivamente, observadas. El triángulo amarillo indica el inclinómetro de superficie (CP). Los círculos violetas son los inclinómetros de pozos (EH y RC). El área de color gris claro corresponde al Campo Geotérmico Cerro Prieto. Las áreas de color gris oscuro son las zonas urbanas. El rectángulo punteado es el área graficada en las Figuras 34-35, 39.

V.2 Data

The May 2006 earthquake sequence occurred in a region monitored by a network of continuously recording geotechnical instruments and well piezometers. The area is also periodically surveyed by leveling surveys (see chapter I.3). The surface data was supplemented by DInSAR. Next the available data are summarized.

V.2.1 Recordings from geotechnical instruments

The May 2006 earthquakes sequence was recorded by five instruments: two vertical crackmeters (FM and ES), two borehole tiltmeters (EH and RC) and one surface tiltmeter (CP) (see chapter I for instruments description). The location of the instruments is presented in the Figure 31. The observed amplitudes of surface displacement and tilt offset are listed in Table VIII and shown in Figure 32.

The vertical crackmeters are installed at the Morelia fault (FM), which was responsible for the May 24, 2006 earthquake, and at the Saltillo fault (ES).

The record of the vertical FM crackmeter showed that the total motion during the May 24, 2006 earthquake, after corrections for installation angle (30° from the horizontal) and instrument separation from the benchmark, is 20-25 cm, which matches the reported field observations of surface offset.

The record of the vertical ES crackmeter showed 2 mm of vertical motion in the Saltillo Fault, probably triggered by the mainshock in Morelia Fault. The ES vertical crackmeter is located ~13 km to the east from the epicenter.

The tiltmeters report impulsive tilt variation (offset) in two components, correlated with May 24, 2006 Mw=5.4 event (Figure 32). The observed tilt offset amplitudes are characterized by simultaneous occurrence at recording stations and disperse values ranging between 21 (North component of RC) and more than 2000 microradians (East component of EH). The aftershocks also caused some tilting effects detected by the tiltmeters.

Table VIII: Geotechnical instruments coordinates (Geodetic Projection, NAD27), and coseismic displacements and tilt change amplitude, both observed and predicted by the preferred fault model. For the tiltmeters (EH, RC and CP) the uplift in the North and East directions corresponds to positive tilt change.

Tabla VIII: Coordenadas de los instrumentos geotécnicos (Proyección Geográfica, NAD27) y desplazamiento y cambio de inclinación cosísmicos, tanto observados como predichos por el modelo final de la falla. Para los inclinómetros (EH, RC y CP) una subida en las direcciones Norte y Este corresponde a cambio positivo de la inclinación.

Geotechnical Instrument	Latitude N (°)	Longitude W (°)	Observed		Predicted	
			Displacement (mm)			
FM	32.4213	115.2596	70 (200- 250*)		~240	
ES	32.4264	115.1277	2		---------------	
			Tilt (μrad)			
			North	East	North	East
EH	32.4249	115.2193	-420	---------	4	50
RC	32.4303	115.3131	-21	-40	-0.695	0.975
CP**	32.4212	115.2592	170	930	920	-900

* Displacement after correction for installation angle and for instrument separation from the benchmark.

** For the surface CP tiltmeter, originally uplift in the North and East directions corresponded to negative tilt change. The sign of the CP data was inverted to be in agreement with those of other tiltmeters.

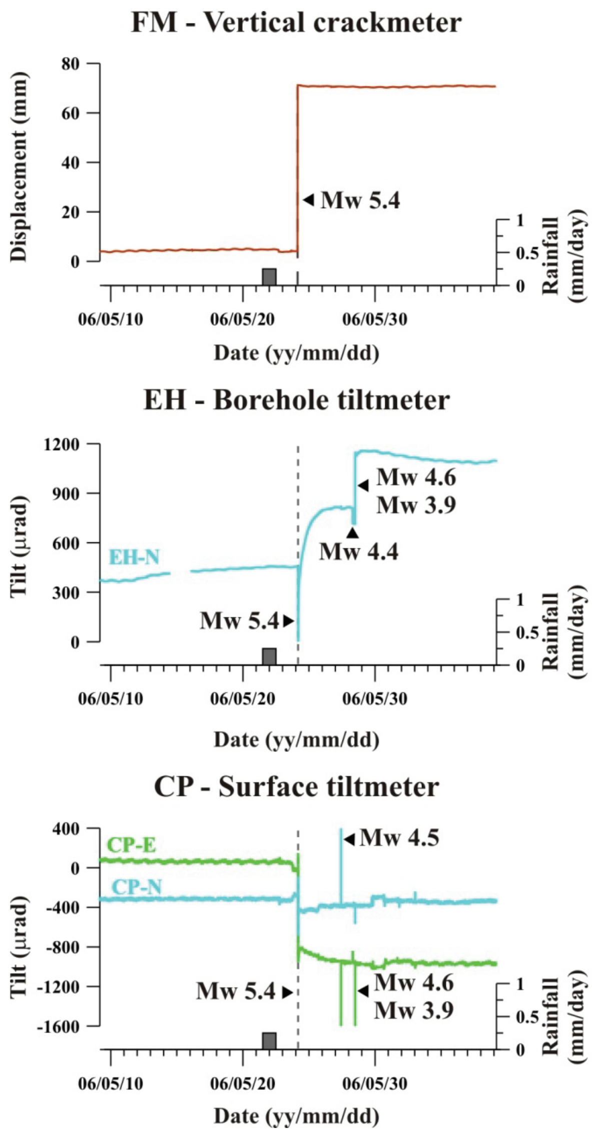

Figure 32: Geotechnical instruments records showing the surface displacement and tilt related to the May 24, 2006 earthquake. The changes caused by aftershocks are indicated. For the tiltmeters two components: North and East, are presented (except EH East component which was out of range). Surface uplift in North and East directions correspond to tilt increase for the borehole tiltmeters, and to tilt decrease for the surface tiltmeter. The timescale covers a range of 15 days before and after the May 24, 2006 earthquake. The sampling interval is 20 minutes for the vertical crackmeters, and four and two minutes for the borehole and surface tiltmeters, respectively. Rainfall data from the Yuma Mesa weather station are also presented.

Figura 32: Registro de instrumentos geotécnicos mostrando el desplazamiento del terreno e inclinación relacionados con el sismo del 24 de Mayo de 2006. Los cambios causados por réplicas están señalados. Para los inclinómetros se presenta dos componentes: Norte y Este, se presentan (excepto por la componente Este de EH que se encontraba fuera de rango). Una subida del terreno en direcciónes Norte y Este corresponde a incremento de la inclinación para los inclinómetros de pozo y disminución de ésta para el inclinómetro

superficial. La escala de tiempo cubre 15 días antes y después del evento principal. El intervalo de muestreo es 20 minutos para los grietómetros verticales, y 4 y 2 minutos para los inclinómetros de pozo y superficial, respectivamente. Datos de precipitación de la estación meteorológica de Yuma Mesa también son presentados.

The data from the FM vertical crackmeter were used for the source fault parameters modeling (see chapter V.4), because this crackmeter directly reports the coseismic motion in the fault which generated the earthquake; unlike the ES vertical crackmeter which probably reports the triggered motion in another fault. The tiltmeters data were not included in the source fault modeling because the shallow and surface tilt sensors are influenced not only by the surface displacement caused by the earthquake but also by motions on cracks, fractures, and on minor faults near the instrument site, as well as by instability of the benchmarks, as has been noted for other earthquakes (McHugh and Johnston, 1977; Allen, 1978; Wyatt, 1988; Takemoto, 1995).

V.2.2. Leveling survey

Leveling measurements in the Mexicali Valley began in the 1960's, as part of the geothermal field preparations and as surveys for tectonics studies. The most recent leveling survey (first-order, first-class) measurement was performed in February 2006, three months before the earthquake. After the earthquake, a repeat survey was carried out in June 2006 across the Morelia fault, at 7 benchmarks along profile AA' (Table IX, Figure 31). The length of the leveling profile is 4.75 km (~1.70 km on the foot wall and 3.05 km on the hanging wall). The maximum relative vertical displacement is 20 cm, which matches the displacement reported by field observations and recorded by the crackmeter. The estimated uncertainty is ±3 mm, using the approach of Dzurisin *et al.* (2002).

V.2.3. Field surface rupture observations

In addition to the instrumental records, field observations were also conducted on June 03, 2006, 9 days after the earthquake. Evidence of surface faulting was found along more than 5 km to northeast from the epicenter (Figures 31), with 1-30 cm of vertical displacement and dip to the SE, as reported also by Suárez-Vidal *et al*. (2007) and Lira (2006). Surface faulting to the west of the evaporation pond (W-SW from the epicenter) was not observed. The visible surface fault traces suggest that faulting could have developed along two sub-parallel fault segments, instead of a single one (Munguía *et al.,* 2009).

Table IX: Leveling line benchmark coordinates (Geodetic Projection, NAD27) and vertical coseismic displacements relative to LE-03.

Tabla IX: Coordenadas de las bases del perfil de nivelación (Proyección Geográfica, NAD27) y desplazamiento cosísmico vertical relativo a la base LE-03.

Benchmark	Latitude N (°)	Longitude W (°)	Height (m) before EQ	Height (m) after EQ	Vertical displacement (cm)
10066	32.4329	115.2708	11.155	11.15645	-0.162
LE-03	32.4306	115.2698	12.557	12.5569	0
10065	32.4275	115.2640	10.213	10.27102	-5.758
10064	32.4199	115.2586	9.701	9.86651	-16.56
10063	32.4133	115.2505	8.879	9.07248	-19.345
10062	32.4075	115.2449	8.829	9.03283	-20.431
10061	32.4010	115.2381	7.448	7.57857	-13.014

V.2.4. Groundwater level data

During the May 24, 2006 earthquake, six piezometers of the Mexicali Valley Piezometric Network were in operation, and all recorded a groundwater level change at the time of the earthquake (Figure 33 and Table X). Figure 31 shows the location of these piezometers. The change, which occurred as a step-like offset up to 6.7 m in amplitude (well PZ-1), was largest at wells closest to the surface rupture. The other wells showed changes on the range of 1 to 55 cm. Well II-9, which is not instrumented, showed changes in flow after the earthquake. Note that coseismic groundwater level response is not instantaneous; groundwater level in the well cannot track arbitrarily fast changes of aquifer pressure because a change of groundwater level in the well requires water to flow into or out of the well. This degradation of groundwater level response to aquifer pore pressure is often termed "wellbore storage" and depends on the characteristics of each particular well. The groundwater level changes following the May 24, 2006 earthquake show that, the largest wellbore storage effect is at the location of C-3 well, where it took about 10 hours for the groundwater level to reach its highest value after the earthquake (Figure 33).

After the May 24, 2006 earthquake the elevated or declined groundwater level began to recover gradually (with exception of PZ-7 well) as a result of the pressure diffusion caused by a pressure gradient in the aquifer. This groundwater level recovery causes the recharge from, or discharges to, the surrounding formations. Note how at the PZ-7 well the coseismically declined groundwater level continued to fall gradually after the May 24, 2006 earthquake (Figure 31). This phenomenon is related, possibly, to outflow of groundwater through fractures induced by the earthquake, as proposed by King *et al.* (1999).

The groundwater level changes in response to the Mw 4.4 (# 8 in Table VII and Figure 31), and the Mw 4.6 and Mw 3.9 (# 9-10 in Table VII and Figure 31) aftershocks are also observed in the groundwater level records of the PZ-1, PZ-3 and PZ-7 wells. The groundwater level change in response to the Mw 4.5 (# 6 in Table VII and Figure 31) aftershock was observed in groundwater level record of PZ-1 well.

Table X: Coordinates and depth of piezometric wells (Geodetic Projection, NAD27). Observed coseismic water-level changes are listed. Static volume strain at the well depth calculated using the preferred fault model; negative values mean contraction. Static volume strain efficiency calculated using the observed water-level changes and the estimated static volume strain (see chapter V.4).

Tabla X: Coordenadas y profundidad de los pozos piezométricos (Proyección Geográfica, NAD27). Se lista el cambio de nivel de agua cosísmico observado. Deformación volumétrica estática calculada a la profundidad de pozos usando es modelo final de la falla; valores negativos corresponden a contracción. Eficiencia de la deformación volumétrica estática calculada usando el cambio de nivel de agua observado y la deformación volumétrica estática estimada (en el capítulo V.4).

Well	Latitude N (°)	Longitude W (°)	Depth (m)	Water-level change (cm)	Static Volume strain Model	Static volume strain efficiency (mm/nε)
C-3	32.4261	115.3102	150	55	-1.27E-06	0.43
G-1-17	32.4059	115.1244	150	10	-1.07E-07	0.93
PZ-3	32.4342	115.2140	150	-28	1.50E-06	0.19
PZ-5	32.3332	115.2318	150	1	-3.19E-08	0.31
PZ-7	32.4078	115.1724	150	-3	7.08E-07	0.04
PZ-1	32.4040	115.2343	500	670	-1.48E-05	0.45
II-9	32.3957	115.2109	15	flow	contraction	------------------

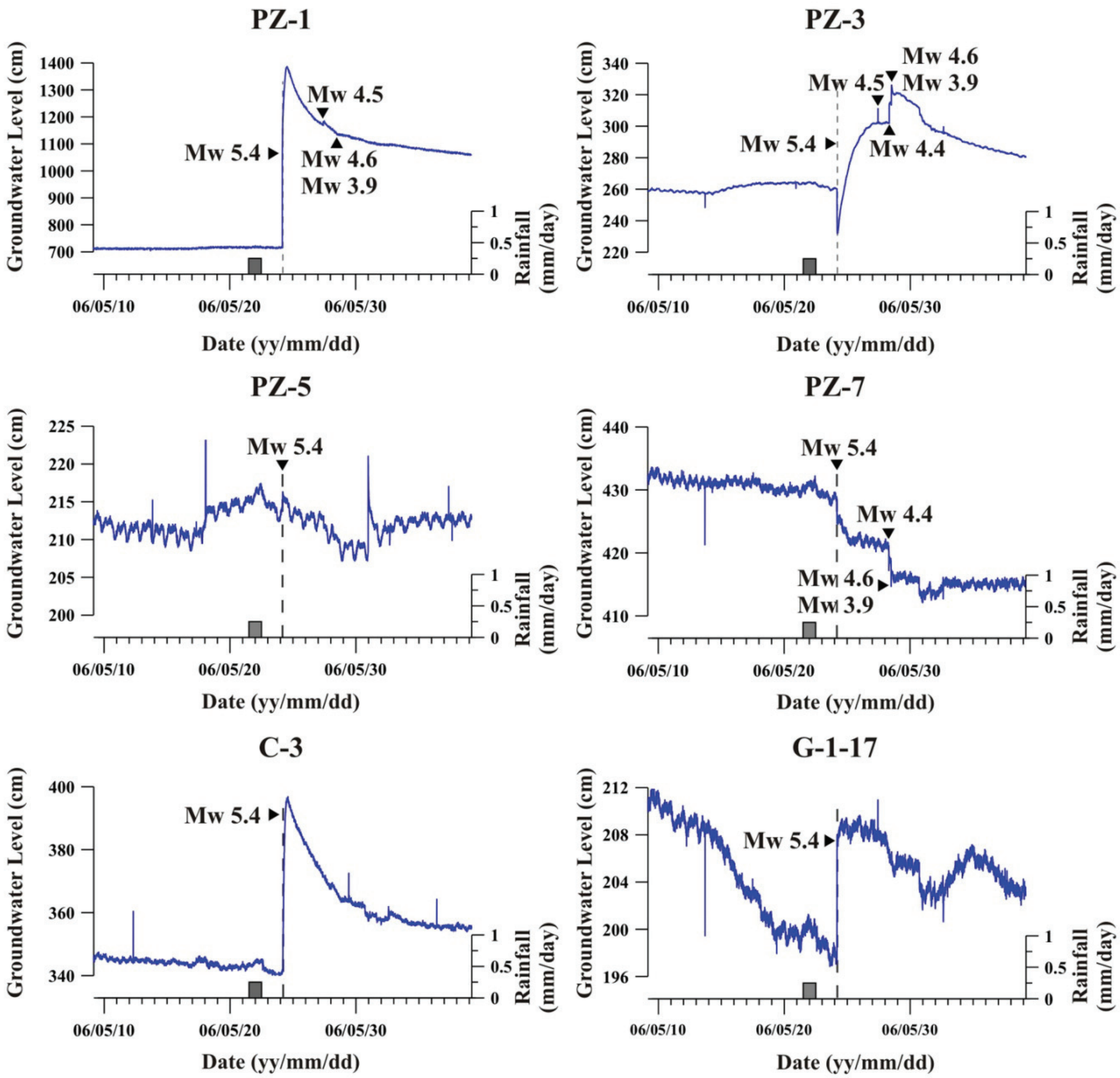

Figure 33: Groundwater level record from wells where the May 24, 2006 mainshock-related changes were observed. Changes caused by aftershocks are indicated. This timescale covers a range of 15 days before and after the mainshock. The records are corrected by atmospheric pressure. The sampling interval is five minutes. Rainfall data from Yuma Mesa meteorological station are also presented.

Figura 33: Registro de nivel de agua subterránea de los pozos donde fueron observados los cambios relacionados con el evento principal del 24 de Mayo de 2006. Los cambios causados por replicas están señalados. La escala de tiempo abarca 15 días antes y después del evento principal. El registro de nivel de agua subterránea está corregido por la presión atmosférica. El intervalo de muestreo es de 5 minutos. Son presentados los datos de precipitación de la estación meteorológica de Yuma Mesa.

V.2.5 DInSAR data

In an attempt to supplement the surface observations and gain an improved understanding of the temporal and spatial distribution of the coseismic surface deformation, DInSAR was used. Interferometric results were processed as described in chapter III. 2. In addition, selected interferograms were also reprocessed by R. Mellors from raw signal data, using the ROI_PAC software (Rosen *et al.*, 2004), to verify results.

All possible interferometric pairs that span the time of the earthquake were processed from the Envisat ASAR images acquired within a time window of 1 year (~ 6 months before and after the earthquake) from both ascending (track 306) and descending (track 84) orbits. Five images from ascending and six from descending orbits were available. The interferometric pairs with $B_{\perp} > 400\,\text{m}$ were discarded, leaving for the analysis a total of five coseismic interferograms. The temporal and perpendicular baselines of the available images are summarized in Table XI. The best resulting interferogram is shown in the Figure 34a; additional coseismic interferograms are shown in the Figure 35.

Unfortunately, the area of the earthquake shows considerable decorrelation on all co-seismic interferograms. This is due in part to an evaporation pond and to farming activity. This decorrelation is also observed on interferograms that do not span the earthquake (see chapter IV). It is likely that some of the decorrelation near the known surface rupture is due to large phase gradients, as the observed surface rupture was spatially complex and possessed up to 20 cm of vertical offset.

Despite the decorrelation, a clear signal was observed in the wrapped phase image. This signal appeared as a series of fringes roughly parallel to the known surface fault and consistent with normal faulting (Figure 34a and 35). Since the fringes occur on independent interferograms, I am confident that they are not due to atmospheric effects. Since the area is topographically flat and fringes are not observed on other interferograms with larger baselines, errors in the DEM can also be ruled out, with the exception of a small area near the 300 m high Cerro Prieto volcano, west of the evaporation pond, which consistently shows large phase residuals. At least 5 fringes to the southeast of observed surface fault (i.e. at least 14 cm LOS displacement; if vertical, at least 15 cm) could be detected in the wrapped interferogram presented in the Figure 34a. Note that fringes are not observed to the west-southwest of the evaporation pond (and epicenter). This, coupled with the field observations, suggests that the earthquake nucleated at the west end of the rupture and propagated to the northeast.

Due to the low coherence of the coseismic images, it is difficult to unwrap the entire interferogram without strong unwrapping errors. The unwrapped results show a deformation field with a smooth pattern across the surface fault rupture. This is because the unwrapping algorithm is dealing with quite noisy signal in which case it seeks for some minimum-cost solution to link the deformed area to the southeast (hanging wall) to the undeformed or slightly deformed area to the northwest (foot wall). The unwrapping errors influence the source fault modeling, producing results that are inconsistent with the field observation data. Therefore, the analysis was solely focused on the wrapped interferograms.

Previous studies have shown that sections of the study area are subsiding at rates of approximately 1 cm per month due to extraction of geothermal fluid in the CPGF (Glowacka *et al*, 1999; Hanssen, 2001; Sarychikina, 2003). Therefore, it is likely that the deformation signal observed in the interferograms includes anthropogenic deformation.

The rate of anthropogenic deformation (assumed to be subsidence) was estimated using previous leveling lines and DInSAR (Sarychikhina *et al.*, 2007). Both individual interferograms and stacks of interferograms were examined. Stacks reduce the effect of atmospheric anomalies but also smooth out temporal variations. A stack formed by the linear combination of 4 interferograms spanning the time between 19 Dec 2004 and 4 December 2005 (350 days; see chapter IV) shows a clear consistent deformation (assumed to be vertical subsidence) that matches the deformation pattern observed on a 70 day interferogram spanning a time just prior to the earthquake. Because the single interferogram matches the spatial pattern of the stack (as well as the leveling line), I do not believe that it is contaminated by large atmospheric artifacts. I decided to use this single interferogram as a measure of the subsidence rate for the co-seismic interferograms rather than the multi-year stack because it should provide a better estimate of the subsidence rate in 2006.

The 70-day anthropogenic line-of-sight displacement (Figure 34b, Table II) shows that the highest subsidence rate occurs below the eastern boundary of the CPGF production zone, with maximum subsidence rate of ~ 1 cm/month. This is similar to earlier estimates (*e.g.*

Sarychikhina *et al.*, 2007). The estimated anthropogenic component (assumed to be vertical and with constant rate in time over 2006) was removed from the leveling data, and it also was added to the final best fit model to compare it with DInSAR data.

Table XI: $B_{\perp}$ ***(m)/*** B_{temp} ***(days) for all possible combinations of cosesimic interferometric pairs from (a) ascending track (track 306, frame 639) and (b) descending (track 84, frame 2961) datasets. The gray color highlight indicates the interferometric pairs with optimal perpendicular baselines. Red numbers indicate the interferometric pairs presented in this thesis.***

Tabla XI: $B_{\perp}$ ***(m)/*** B_{temp} ***(días) para todas las posibles combinaciones de pares interferométricos de pasos (a) ascendiente (paso 306, toma 639) y descendiente (paso 84, toma 2961). El fondo de color gris indica los pares interferométricos con línea de base perpendicular óptima. Los números rojos indican los pares interferométricos que están presentados en este trabajo de tesis.***

a.

Master Image	*Slave Image*		
	2006/09/26	***2006/10/31***	***2006/12/05***
2006/04/04	-162/175	152/210	241/245
2006/05/09	307/140	622/175	707/210

b.

Master Image	*Slave Image*		
	2006/10/15	***2006/11/19***	***2006/12/24***
2005/12/04	-138/315	-478/350	
2006/02/12	171/245	-178/280	
2006/03/19	-545/210	-892/245	124/280

V.3 Groundwater responses to earthquakes

The sensitiveness of the groundwater level to tectonic deformation has been observed in many cases in the form of e.g. pre-, co- and post-seismic well-level changes (e.g. Wakita, 1975; Quilty and Roeloffs, 1997; Roeloffs, 1998; Sil, 2006), spring and streamflow discharges (e.g. Muir-Wood and King, 1993; Koizumi *et al.*, 1996), and changes in radon concentration and temperature of groundwater (e.g. Wakita *et al.*, 1991; Kitagawa *et al.*, 1996). Comprehensive overviews are given in Roeloffs (1988, 1996). Some of the groundwater changes can be explained by poroelastic response to the earthquake's strain field. Within a few source dimensions from the epicenter, an earthquake imposes strain changes that can be viewed as an instantaneous strain step. This coseismic strain is expected to result in a step-like groundwater level change. In a simple linear model, groundwater levels fall or rise depending on whether the connected aquifer expands or contracts due to the seismogenic redistribution of the regional strain field (Wakita, 1975; Grecksch *et al.*, 1999), which has been observed in confined and non-confined aquifers. However, there are others hydrological effects that do not correlate with elastic processes, such as seismic oscillations of water levels due to the effect of surface waves, and long-term changes in water table levels that persist for days or weeks, due to changes in the aquifer properties (Roeloffs, 1998). Hydrologic responses to earthquakes are influenced by such factors as the magnitude and depth of the earthquake, distance from the epicenter, and the hydrogeologic environment. The depth of the well, whether the aquifer is confined or unconfined, and well construction also influence the degree of groundwater level fluctuations in wells in response to seismic waves. Generally, in wells that are far from earthquake sources and where the aquifers are unconsolidated or filled with fractures, non-elastic changes in groundwater level dominate over poroelastic changes. Given that our groundwater level data show the relatively rapid step-like coseismic changes, and because the wells are located within few source dimensions from the epicenter I attributed these changes to poroelastic response.

Assuming that the elastic behavior of the affected aquifer can be described by the linear theory of poroelasticity, the expected size of water-level steps at the individual well locations can be estimated. The theory was developed by Biot (1941) to describe 3-D consolidation and was reformulated by Rice and Cleary (1976). A comprehensive review was given by Kumpel (1991) and Roeloffs (1996), and geophysical applications were discussed by Wang (1993). Under undrained conditions (i.e., where there is no fluid flow) the ratio of water-level change, Δh, to static volumetric strain change, $\Delta\varepsilon_{kk}$, is:

$$\frac{\Delta h}{\Delta \varepsilon_{kk}} = -\frac{1}{\rho_f g}\frac{2\mu B}{3}\frac{1+\nu_u}{1-2\nu_u}, \tag{24}$$

where g is the gravitational acceleration, ρ_f is the fluid density, μ is shear modulus, B is Skempton's pore pressure coefficient, and ν_u is the undrained Poisson's ratio (Roeloffs, 1996). Equation (24) will be referred to as the *static volume strain efficiency*. Because the coseismic volume strain changes occur on a timescale too short to allow the loss or gain of pore fluid by diffusive transport (fluid flow), on that timescale the water level change appearing in (24) is associated with the undrained response of the medium. Therefore, the amplitudes of the step-like groundwater level changes produced by the coseismic strain are proportional to the volumetric strain field.

In the next section, the static volume strain at the well locations is calculated and compared with both sign and amplitude of the observed groundwater level changes to constrain the forward model.

The postseismic response of the water level is also an important factor for understanding the responses of aquifers to earthquakes. Postseismic changes are attributed to the pressure diffusion caused by a pressure gradient in the aquifer. The standard one-dimensional diffusion equation in an unbounded, homogeneous aquifer could be written as (Crank, 1975):

$$\frac{\partial p}{\partial t} = D\frac{\partial^2 p}{\partial z^2}, \tag{25}$$

where D is a hydrological parameter known as the hydraulic diffusivity.

The solution of this equation involves a fairy common mathematical function called the complementary error function:

$$\Delta p(z,t) = P\,erfc(\sqrt{z^2/4Dt}), \tag{26}$$

where $\Delta p(z,t)$ is the change in pore pressure, P is the amplitude of the change, z is the distance to the source of the pore pressure change or diffusion. Based on this equation I can define

$$\tau = z^2/4D \tag{27}$$

as the characteristic decay time of the groundwater level.

V.4 Forward modeling of the source fault

I conducted forward modeling to estimate the earthquake fault parameters (location, dimensions, orientation, and average slip) that best fit the observations. The model consisted of a finite rectangular fault with uniform slip, embedded in an isotropic elastic medium. The solution to this problem was found numerically using the EDCMP software (Wang *et al.*, 2003). Both surface displacement and volume strain changes were calculated during the modeling. Forward modeling based on a set of pre-defined limits was preferred to inversion due to the incomplete data.

Both half-space and layered models were tested. Initially, I used an elastic half-space with shear modulus (rigidity) μ = 10 GPa and Poisson's ratio υ = 0.25. A shear modulus of 30-32 GPa is commonly used in crustal deformation modeling, but this value would not be appropriate for this study given the low elastic modulus of the shallow sedimentary layers in the Cerro Prieto basin. I adopted the shear modulus value of 10 GPa since it is the average value of the uppermost 10 layers in our layered model (Table XII). Initial parameters were based on the observed surface rupture, empirical relationships (Wells and Coppersmith, 1994), and the focal mechanism (Table VI). The top of the fault was set at the surface (based on surface observations) and the rake was defined to be -89° based on the CMT solution and surface observations.

The strike, dip, length, width and slip of the fault were allowed to range within the values 40º - 60º, 30º - 60º, 4km - 6km, 5km - 7 km and 20cm – 40cm, respectively. The modeled vertical surface displacement (Figure 34d) was compared with the leveling data. The volume strain change was compared with the sign and amplitude of groundwater level changes. In addition, I compared simulated and observed wrapped phase interferograms. Before wrapping, the modeled surface displacement vector was converted into line-of-sight displacement (i.e. range change) and the corresponding anthropogenic component was added. The parameters of the best-fit model are presented in Table VI.

A single-fault model explains the observed interferometric fringe pattern (Figure 34a and c) and the coseismic groundwater level changes, and matches the leveling data fairly well (Figure 36). For the leveling data, residuals are larger close to the fault trace (Figure 36).

The largest residual for precise leveling data amounts to 6 cm. One explanation of these residuals is that they are due to the instability of the leveling benchmarks near the surface rupture, where intense surface cracking and deformation were observed in the field.

The distribution of coseismic static volume strain calculated by the best-fit model is shown in Figure 37. Negative values indicate compressional strain, which would cause a rise in water level. The locations of wells showing either a coseismic water-level drop (empty circles) or a rise (filled circles) are displayed. For the model, the signs of the recorded coseismic steps are in agreement with the earthquake-induced static volume strain.

In order to estimate the amplitude of the water-level offsets, it is necessary to calculate the theoretical volume strain efficiency using equation (24). As several of the constants are poorly constrained, I used maximum and minimum values rather than a precise magnitude.

Most of the wells cut through Quaternary alluvium deposits, which consist mainly of water-saturated sands, gravels and clays. For such sediments, Skempton's parameter is assumed to be $0.5 \le B \le 0.99$. For the first layer of the layered elastic space (Table XII) I obtained the shear modulus value of $\mu = 1.3 \times 10^9$ Pa, and a drained Poisson's ratio value of $\nu = 0.4$. Because the undrained Poisson's ratio is $\nu \le \nu_u \le \frac{1}{2}$, the $0.4 \le \nu_u \le 0.49$ may be adopted. The range of the shear modulus lies between 1 and 10 GPa, where the bottom value is the shear modulus of the upper layer in the layered crust model, and the upper value is the shear modulus used in the homogeneous model. As a result, the theoretical volume strain efficiency value is estimated to be between 0.2 and $50\, mm/n\varepsilon$ ($1 n\varepsilon = 10^{-9}$).

Figure 38 displays expected well-level steps Δh as derived from the volume strain $\Delta\varepsilon_{kk}$ for two values of the theoretical volume strain efficiency (in $mm/n\varepsilon$). The observed step amplitudes are also displayed versus the calculated volume strains at the well locations. The best least-squares fit for our model results in a static volume strain efficiency of 0.45 $mm/n\varepsilon$ with coefficient of determination, R^2, of 0.994, which falls close to the lower bound of the predicted range of values. This result suggests that the amplitudes of the observed steps are well explained by earthquake-induced volume strain. However, the amplitude of the coseismic step in PZ-7 well is smaller than predicted by the model. This might be due to a strain field more complex than the simple model assumed here or to site effects due to local heterogeneity in the geological structure (Koizumi *et al.*, 1996). The error in coseismic groundwater level value determinations could also influence the results, because in this particular well record it is difficult to distinguish between the coseismic and postseismic groundwater level drops.

The value of the static volume strain efficiency calculated for each individual well is illustrated in Table X. It varies from 0.04 (PZ-7) to 0.93 (G-1-17) $mm/n\varepsilon$, with an average value of 0.39 $mm/n\varepsilon$. The standard deviation of the estimated values of the static volume strain efficiency is $\pm 0.28\, mm/n\varepsilon$, and all values, except for two extreme values (PZ-7 and G-1-17), are within 1 standard deviation from the average value. The relatively small static volume strain value for PZ-7 is due to amplitude of groundwater level change smaller than expected from the model and it possible reasons are explained above. The relatively big value of static volume strain for G-1-17 are due to amplitude of groundwater level change bigger than expected from the model and it could be due to the well location near the Saltillo Fault where the motion was triggered by the mainshock event. The nonelastic response of groundwater level could influence as well.

I repeated the modeling procedure using an elastic layered medium and the same fault parameters. A layered model with velocities based on Wong *et al.* (1997) and densities calculated using Gardner's relationship (Gardner *et al.*, 1974) was used (Table XII). The vertical displacement pattern that resulted from the layered model was within 0.7 cm of the values from the half-space model. Figure 39 shows the differences between the vertical displacements predicted by the layered and the homogeneous models; it can be seen that the largest differences are concentrated in a ~1 km-thick zone surrounding the surface rupture. For the calculated volume strains, the best least-squares fit results in a static volume strain efficiency of 0.6 $mm/n\varepsilon$ with a coefficient of determination, R^2= 0.995.

Using a shear modulus value of 10 GPa and the best-fit model fault parameters, I found a geodetic moment equal 1.18×10^{17} Nm, similar to teleseismic estimates of 1.07×10^{17} Nm (*Global Centroid Moment Tensor* (CMT) moment).

Using the preferred model, the North and East tilt components were estimated and are presented in the Table VIII. Strong discrepancies between coseismic tilt variation and predicted surface displacement confirm the initial supposition about a different source of influence to the coseismic tiltmeters records. The simplicity of the model could be attributed as well.

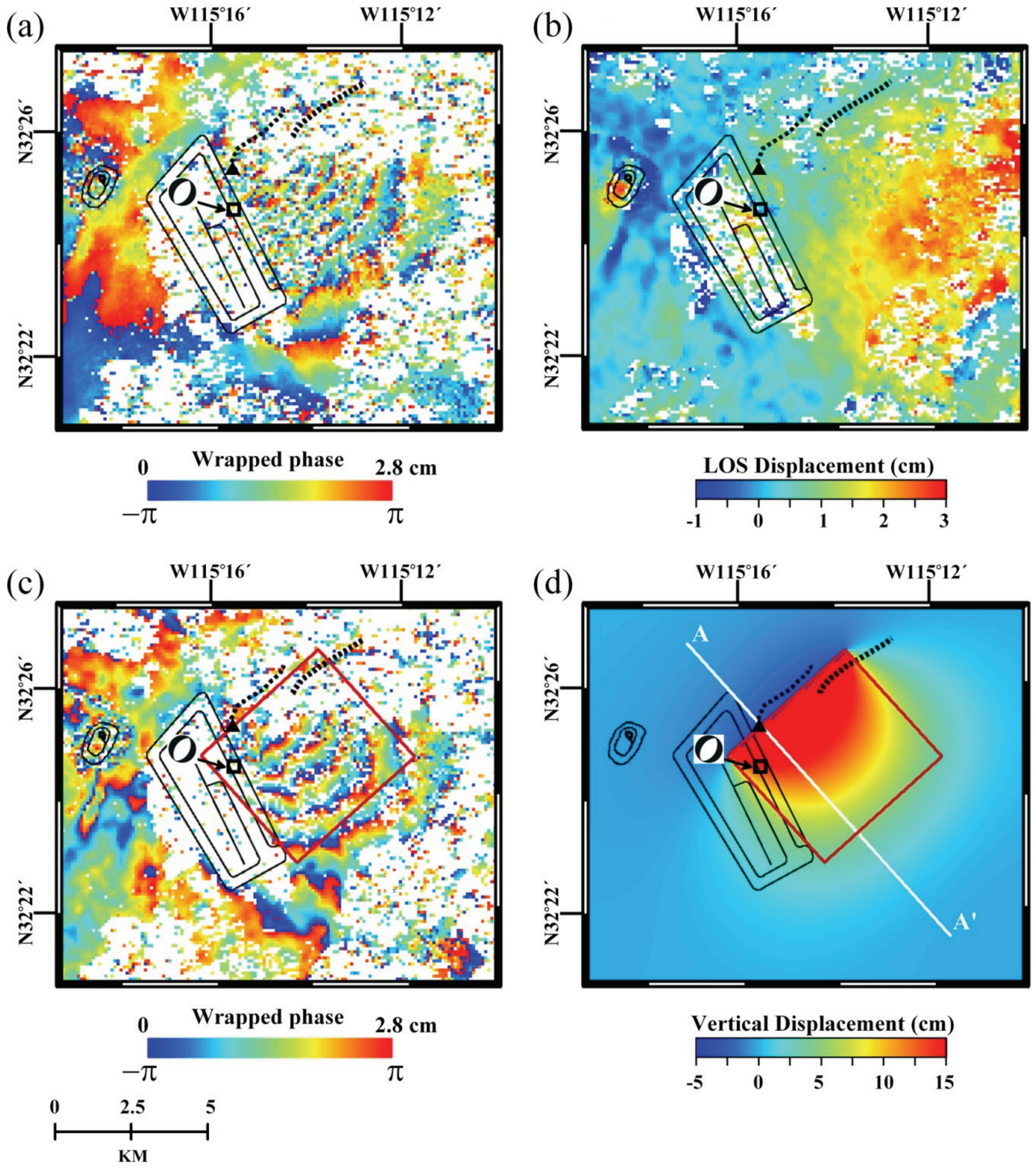

Figure 34: (a) Wrapped interferogram spanning the 24 May 2006 earthquake (Envisat ascending, 140 days, 2006/05/09 – 2006/09/26, 307 m perpendicular baseline). Areas of low coherence (<0.1) are masked. (b) Unwrapped interferogram showing LOS displacement for presumed anthropogenic subsidence (Envisat descending, 70 days, 2005/12/04 - 2006/02/12, 300 m perpendicular baseline). Apparent displacement near Cerro Prieto volcano at far left due to errors in DEM. (c) Simulated interferogram created by first summing the modeled

surface displacement and the anthropogenic component and then wrapping the result. The anthropogenic component is a scaled version of the unwrapped interferogram in Figure 32b to produce an equivalent 140 days of subsidence. Therefore, the simulated interferogram also contains artifacts in addition to the modeled signal. The areas which have low coherence in the original interferogram are masked. (d) Vertical displacement map predicted by the best fit model. Positive values correspond to the ground subsidence. The red rectangle is the model fault projected on the surface. The white line corresponds to the profile AA' illustrated in Figure 36. The borders of the evaporation pond and the Cerro Prieto volcano are superposed on the images for reference. The dotted lines indicate the location where the surface faulting was observed. The small black square denotes the epicenter of the May 24, 2006 earthquake. The focal mechanism (Global CMT) is also shown.

Figura 34: (a) Interferograma de fase empacada que abarca el tiempo de ocurrencia del sismo de 24 de Mayo de 2006 (Envisat, paso ascendiente, 2006/05/09 – 2006/09/26, 140 días, línea de base perpendicular es 307 m). Las áreas de baja coherencia (<0.1) están enmascaradas. (b) Interferograma desempacado que muestra el desplazamiento LOS por presunta subsidencia antropogénica (Envisat, paso descendiente, 70 días, 2005/12/04 - 2006/02/12, línea de base perpendicular es 300 m). El desplazamiento aparente en el área del Volcán Cerro Prieto en la extrema izquierda del mapa se debe a los errores del Modelo Digital de Elevación. (c) Interferograma simulado creado, primero, sumando el desplazamiento de la superficie modelado y la componente antropogénica, y, después, empacando el resultado. La componente antropogénica es la versión normalizada para 140 días del interferograma desempacado presentado en la Figura 32b. Por lo tanto, el interferograma simulado además de la señal modelada contiene algunos artefactos. Las áreas que presentan baja coherencia en el interferograma original están enmascaradas. (d) Mapa del desplazamiento vertical predicho por el modelo de mejor ajuste. Los valores positivos corresponden a la subsidencia del terreno. El rectángulo rojo es la proyección de la falla del modelo en la superficie. La línea blanca corresponde al perfil AA' mostrado en la Figura 36. Los contornos de la laguna de evaporación y del volcán Cerro Prieto están sobrepuestos a las imágenes como referencia. La línea punteada indica la localización donde fue observada la ruptura superficial. El cuadrado negro pequeño indica el epicentro del sismo del 24 de Mayo de 2006. El mecanismo focal (Global CMT) también es mostrado.

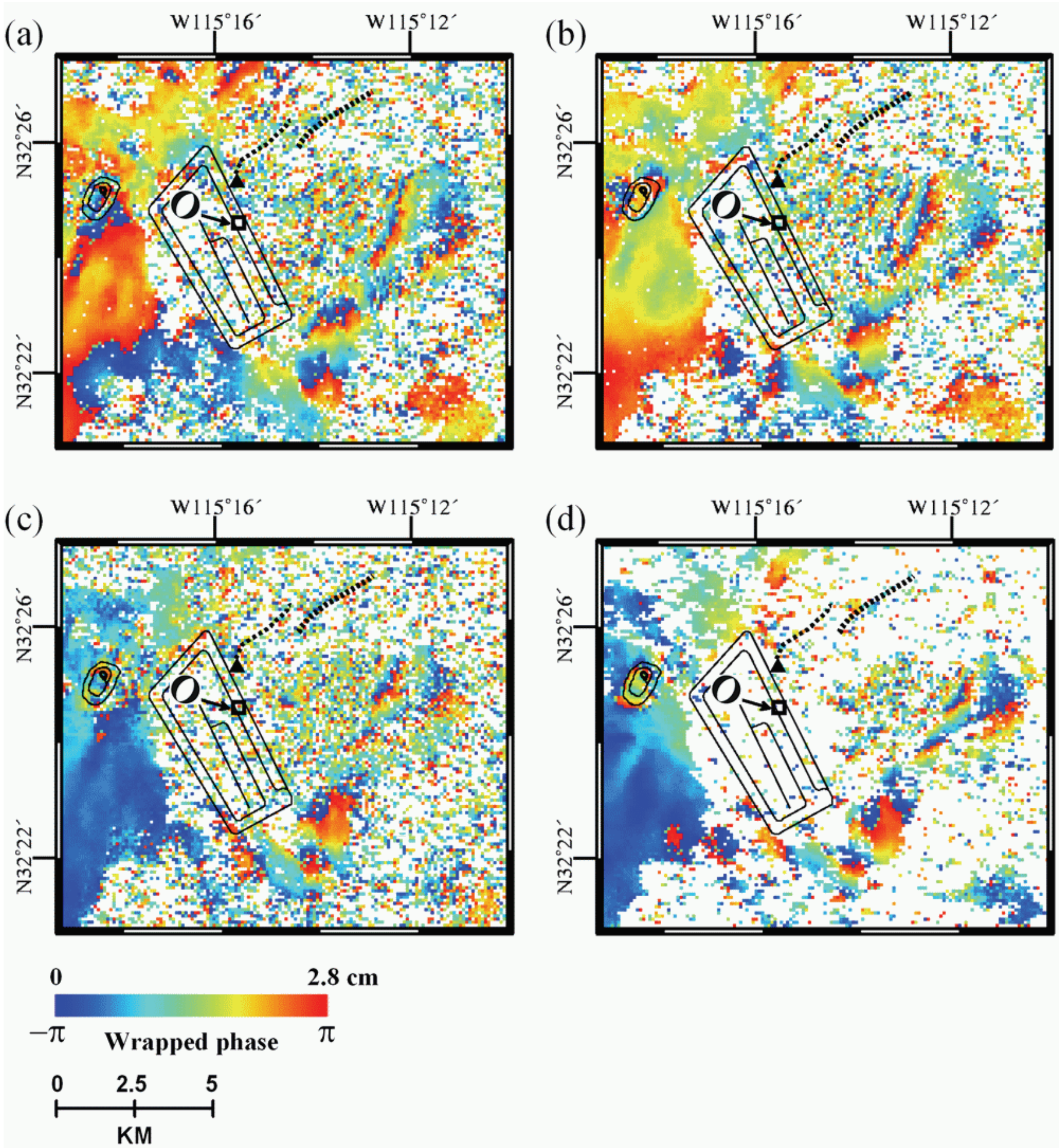

Figure 35: Interferogram generated from SAR data acquired on: (a) Envisat ascending, 2006/04/04 – 2006/09/26, 175 days, -162 m perpendicular baseline, (b) Envisat ascending, 2006/04/04 – 2006/10/31, 210 days, 152 m perpendicular baseline, (c) Envisat descending, 2006/02/12 – 2006/11/19, 280 days, 178 m perpendicular baseline, (d) Envisat descending, 2006/03/19 – 2006/12/24, 280 days, 124 m perpendicular baseline. Areas of low coherence (<0.1) are masked. The contours of the evaporation pond and the Cerro Prieto volcano are superposed on the images for reference. The dotted lines indicate the location where the surface faulting was observed. The small black square denotes the epicenter of the May 24, 2006 earthquake. The focal mechanism (Global CMT) is also shown.

Figura 35: Interferogramas generados a partir de imágenes SAR de: (a) Envisat, paso ascendente, 2006/04/04 – 2006/09/26, 175 días, línea de base perpendicular es -162 m, (b) Envisat, paso ascendente, 2006/04/04 – 2006/10/31, 210 días, línea de base perpendicular es 152 m, (c) Envisat, paso descendente, 2006/02/12 – 2006/11/19, 280 días, línea de base perpendicular es 178 m, (d) Envisat, paso descendente, 2006/03/19 – 2006/12/24, 280 días, línea de base perpendicular es 124 m. Las áreas de baja coherencia (<0.1) están enmascaradas. Los contornos de la Laguna de evaporación y el volcán Cerro Prieto están sobrepuestos a las imágenes como referencia. La línea punteada indica la localización donde la ruptura superficial se ha observado. El cuadrado negro pequeño indica el epicentro del sismo del 24 de Mayo de 2006. El mecanismo focal (Global CMT) también es mostrado.

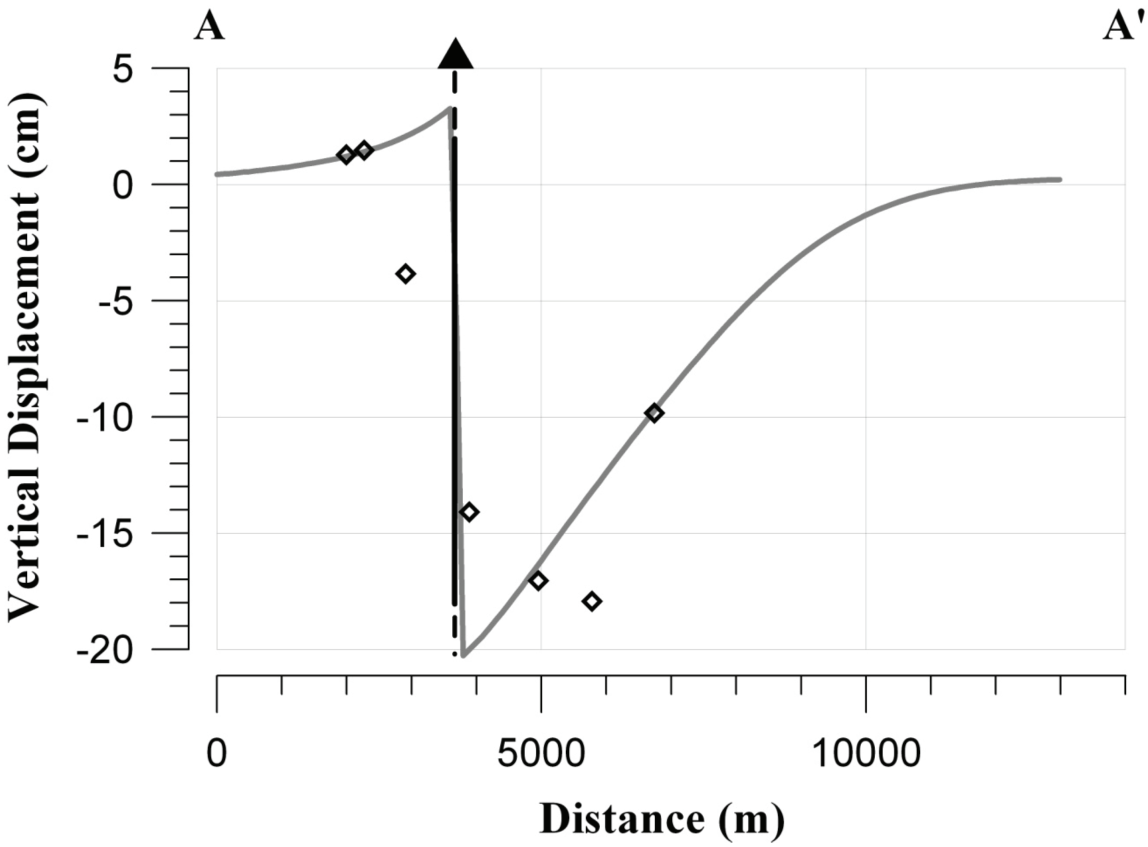

Figure 36: Displacement along AA' profile of Figure 34d. Black diamonds are leveling data. The solid gray line indicates simulated vertical displacements. The leveling data was corrected for the anthropogenic component. The black triangle indicates the location of the FM crackmeter, and the black line represents the 22.5±2.5 cm of relative coseismic displacement recorded by this instrument.

Figura 36: Desplazamiento a lo largo del perfil AA' mostrado en la Figura 34d. Los diamantes negros son los datos de nivelación. La línea gris continua indica el desplazamiento simulado. Los datos de nivelación fueron corregidos por la deformación antropogénica. El triángulo negro indica la localización del grietómetro FM, y la línea negra representa los 22.5±2.5 cm de desplazamiento cosísmico relativo registrados por el instrumento.

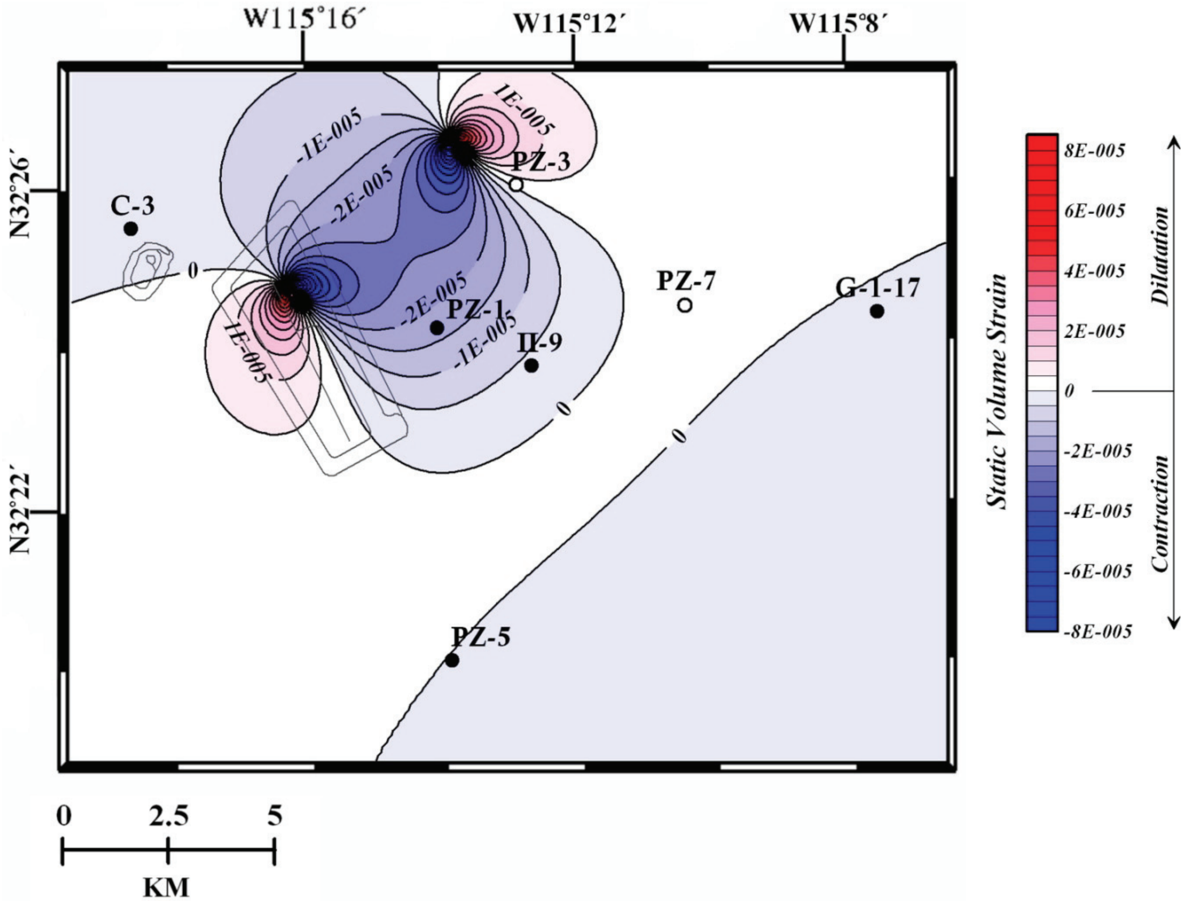

Figure 37: Contour plots of the static volume strain field at the depth of 150 m, induced by the 24 May 2006 earthquake, as calculated for the preferred fault model. Wells showing a groundwater level rise or drop are indicated by filled and empty circles, respectively.

Figura 37: Mapa de contornos del campo de deformación volumétrica estática a la profundidad de 150 m, inducido por el sismo del 24 de Mayo de 2006, calculado usando el modelo final de la falla. Los pozos en los cuales se observó subida o bajada del nivel de agua subterránea son indicados con círculos llenos y vacios, respectivamente.

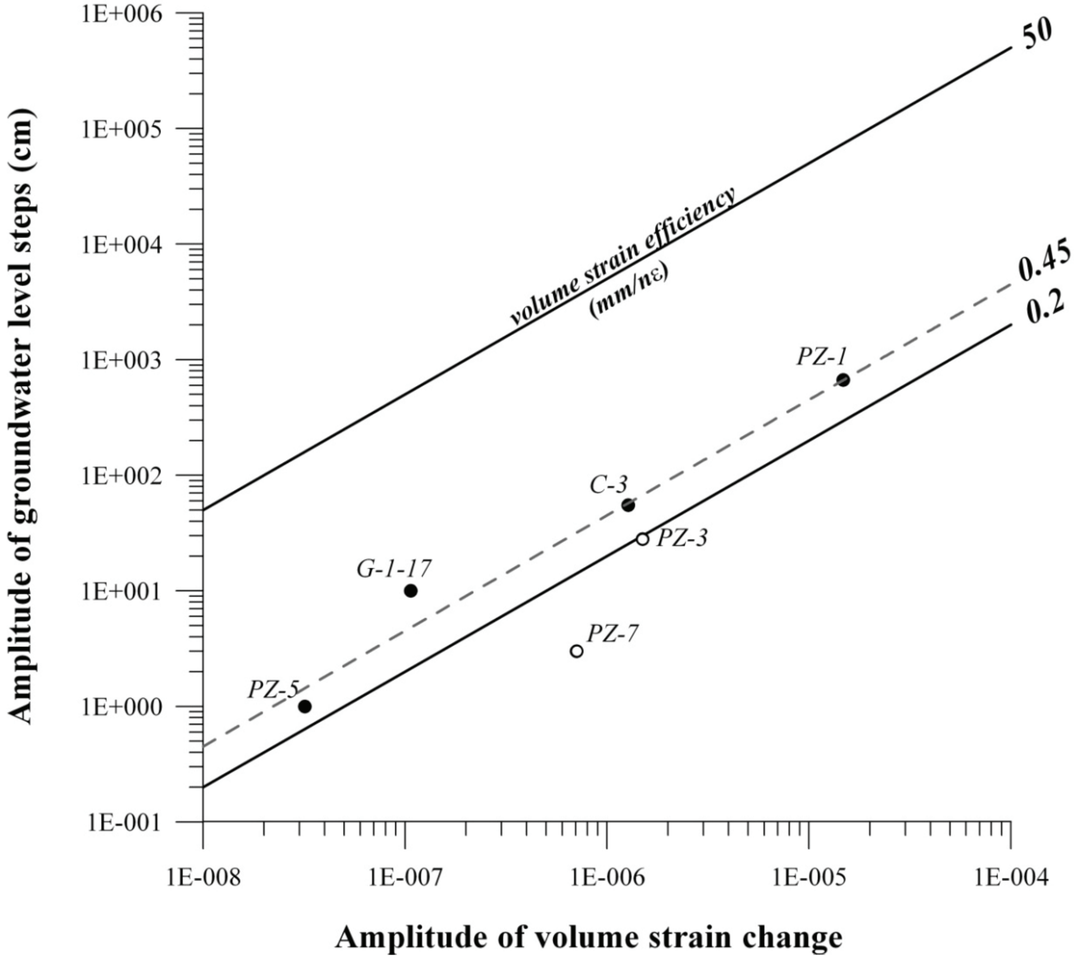

Figure 38: Theoretical and observed groundwater level changes, Δh, versus predicted volume strain, $\Delta\varepsilon_{kk}$. Note that both axes show absolute values of the respective amplitudes. The black lines show the expected amplitude groundwater level changes for static volume strain efficiencies of 0.2 and 50 $mm/n\varepsilon$. The circles show the observed co-seismic change in water level and using the preferred model volume strain at the well locations and depths. Filled symbol: groundwater level rise; empty symbol: groundwater level drop. The gray dashed line is the best linear fit for the model result.

Figura 38: Cambios de nivel de agua subterránea teórico y observado, Δh, versus deformación volumétrica predicha, $\Delta\varepsilon_{kk}$. Nótese que ambos ejes muestran valores absolutos de las respectivas amplitudes. Las líneas negras muestran la amplitud esperada del cambio de nivel de agua subterránea para la eficiencia de la deformación volumétrica estática de 0.2 y 50 $mm/n\varepsilon$. Los círculos muestran el observado cambio cosísmico de nivel de agua subterránea y deformación volumétrica predicha por el modelo final en la localización y profundidad de los pozos. Símbolos llenos indican subida del nivel de agua subterránea; símbolos vacios indican bajada. La línea punteada gris es el mejor ajuste lineal de los resultados modelados.

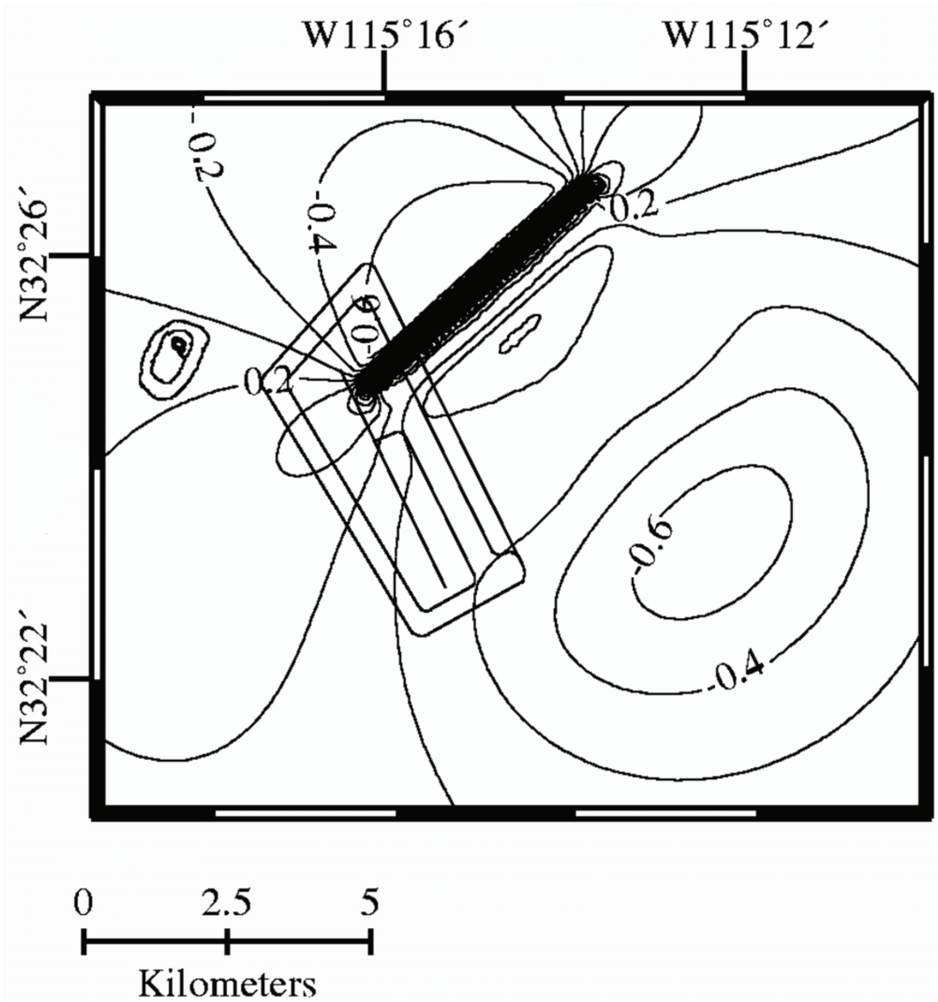

Figure 39: Differences (cm) between the vertical displacements predicted by the layered and the homogeneous model.

Figura 39: Diferencias (cm) entre los desplazamientos verticales predichos por los modelos estratificado y homogéneo.

Table XII: Parameters of layered elastic space.

Tabla XII: Parámetros del medio elástico estratificado.

Layer	P-wave velocity* (km/s)	S-wave velocity** (km/s)	Depth to the top of the layer (km)	Density*** (g/cm3)	μ (Pa)
1	2.000	0.800	0.000	2.073	1.33E+09
2	2.533	1.055	0.500	2.199	2.45E+09
3	2.900	1.261	1.250	2.275	3.62E+09
4	3.267	1.485	1.750	2.344	5.17E+09
5	3.633	1.730	2.250	2.407	7.20E+09
6	4.000	1.905	2.750	2.465	8.95E+09
7	4.367	2.184	3.250	2.520	1.20E+10
8	4.773	2.367	3.750	2.577	1.44E+10
9	5.100	2.684	4.250	2.620	1.89E+10
10	5.375	2.986	4.750	2.654	2.37E+10
11	5.650	3.139	5.250	2.688	2.65E+10
12	5.750	3.194	5.750	2.699	2.75E+10
13	5.800	3.222	6.750	2.705	2.81E+10
14	5.850	3.250	7.600	2.711	2.86E+10
15	6.600	3.708	7.900	2.794	3.84E+10
16	6.800	3.820	8.200	2.815	4.11E+10
17	7.000	3.933	8.500	2.836	4.39E+10
18	7.200	4.045	12.500	2.856	4.67E+10
19	7.500	4.289	17.000	2.885	5.31E+10
20	7.800	4.457	20.000	2.913	5.79E+10

* Based on Fuis *et al.,* (1982).

** Based on González *et al.*, (1983).

*** Calculated using Gardner's relationship (Gardner *et al.*, 1974).

V.5 Modeling of groundwater level changes

As discussed earlier, the six piezometric wells recorded step-like coseismic water level changes followed by gradual postseismic changes. I fit the groundwater time series using a combination of a linear trend (for preseismic), a step function (for coseismic) and an error function (for postseismic) of the form:

$$w(t) = I + St + CH(t - t_0) - Perfc(\sqrt{\tau/(t - t_0)}) \quad (28)$$

Where I (intercept) and S (slope) are constants that describe the linear pre-earthquake trend, H is the Heaviside function, C is a constant (magnitude of the coseismic step), *erfc* is the complementary error function and P is a constant (magnitude of the postseismic changes). The time of the earthquake is $t_0 = 0$ and $w(t)$ is the observed level at any time t of the time series. I used least-squares to fit the groundwater level data from the May 24, 2006 earthquake, and to simultaneously estimate all parameters before and after the earthquake.

The PZ-5 and PZ-7 wells were excluded from this analysis because in the case of PZ-5 well the coseismic groundwater level changes were very small (1 cm), whereas in the case of PZ-7 well there was no recovering of the groundwater level after the earthquake (see chapter V.2.4 and Figure 33).

The results of the modeling and the residuals are shown in the Figures 40; the estimated parameters are presented in the Table XIII. Large residuals (observed records minus fit) occur over the period close to the earthquake occurrence and are directly related to the "wellbore storage" effect discussed above.

Assuming that the source of the pore pressure changes is located around the coseismic fault plane, the minimum distances to the fault plane from the well locations were obtained and the hydraulic diffusivities were estimated using Equation (27). The results are shown in Table XIII. The values of estimated hydraulic diffusivity range from 3.4×10^4 to 7×10^4 cm^2/s, with an average value of 5.1×10^4 cm^2/s. The estimated hydraulic diffusivity values are close to those determined for the same area by Glowacka and Nava (1996), 3×10^4 - 3×10^5 cm^2/s for seismicity related to the fluid extraction (pressure decrease) in the CPGF, and by Glowacka *et al.* (2009), ~10^4 cm^2/s for creep rate related to the fluid extraction location.

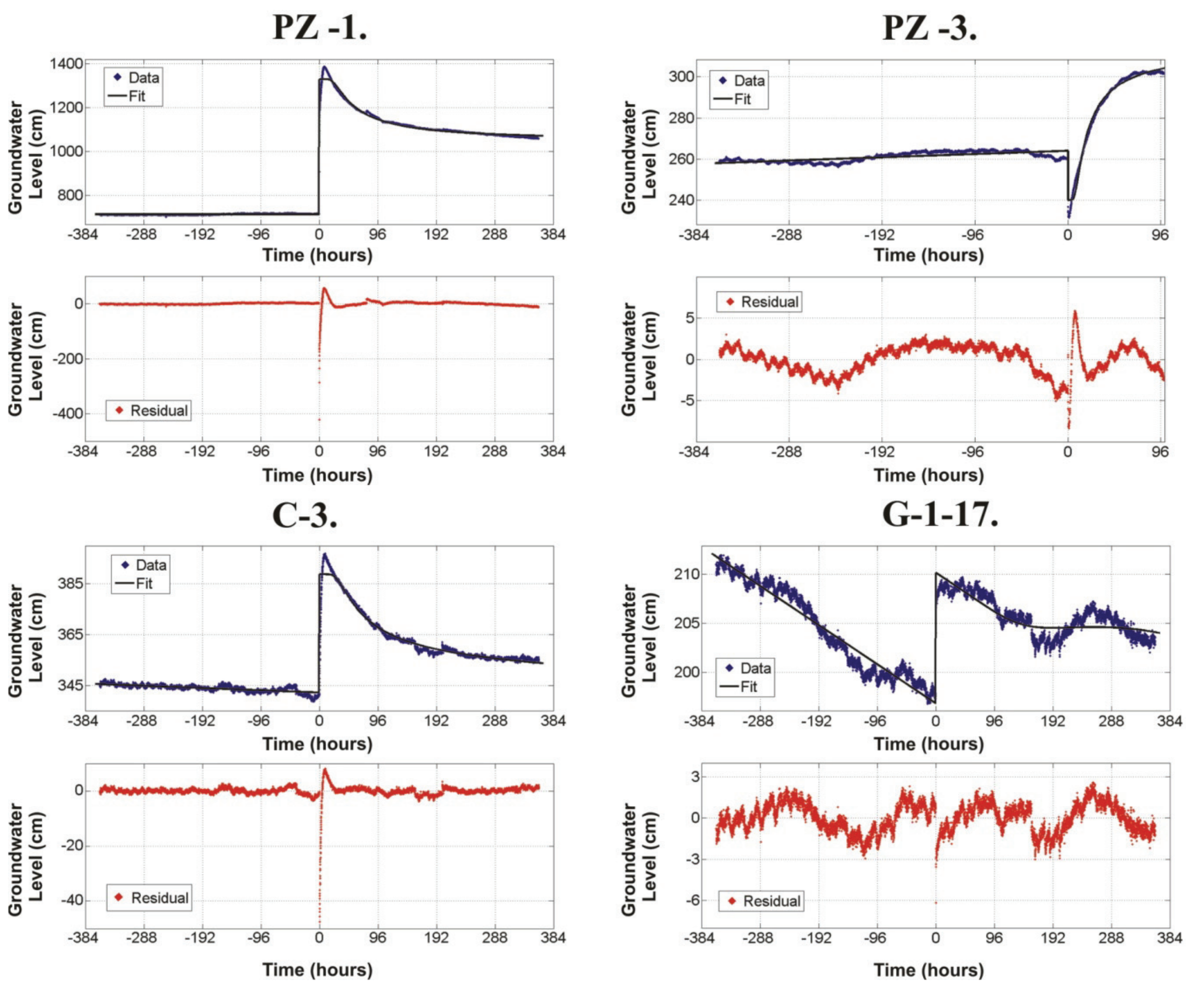

Figure 40: Fit of groundwater level changes following the May 24, 2006 earthquake. $t_0 = 0$ ***is the earthquake occurrence time.***

Figura 40: Ajuste de los cambios de nivel de agua subterránea tras el sismo del 24 de Mayo de 2006. $t_0 = 0$ **es el tiempo de ocurrencia del sismo.**

Table XIII: Coseismic (C) and postseismic (P) groundwater level changes and decay constants (τ) obtained by fitting the piezometric records. Z (m) is the minimum distance from well location to the coseismic fault plane. The observed values of coseismic groundwater level changes are shown in parentheses.

Tabla XIII: Cambio cosísmico (C) y postsísmico (P) del nivel de agua subterránea y constante de decaimiento (τ) obtenidos del ajuste de registros piezométricos. Z (m) es la mínima distancia entre el pozo y el plano de falla cosísmica. Los valores del cambio cosísmico del nivel de agua subterránea se muestran entre paréntesis.

Well	C (cm)	P (cm)	τ (hours)	R-square	RMS	Z (m)	D - Hydraulic Diffusivity (cm^2/s)
PZ-1	615 (670)	287	64	0.997	11.6	1780	3.4E+04
PZ-3	-24 (-28)	-71	21	0.985	1.7	1130	4.2E+04
C-3	47 (55)	36	80	0.971	2.2	2600	5.9E+04
G-1-17	13 (10)	23	446	0.912	1.0	6700	7.0E+04

V.6 Results and discussion

Clear deformation signals caused by the May 24, 2006 earthquake were detected by DInSAR, leveling surveys, field observations and geotechnical instruments (crackmeters and tiltmeters). The earthquake also produced groundwater level changes in the shallow aquifer and triggered motion in the Saltillo fault.

Source parameters for the earthquake were estimated using forward modeling of both surface deformation data (DInSAR, leveling survey and FM vertical crackmeter data) and static volume strain changes inferred from co-seismic changes in groundwater level. The observations can be best explained by a 45º SE dipping normal fault rupturing an area of about 5.2 by 6.7 km^2 to the north-northeast of the CPGF. The rupture strikes N48ºW and has uniform slip of 34 cm. I found that the changes in groundwater level were useful in the constraining of the fault parameters.

The geodetic moment calculated using the preferred model parameters is in good agreement with estimates based on seismic data (*e.g.* CMT).

As no ground deformation was observed by DInSAR or field observations west of the epicenter, a strong northeast directivity effect associated to the propagation of the earthquake rupture is suggested. The strong directivity together with the shallow depth may explain why the intensity of shaking was exceptionally strong for an earthquake of this size, especially because the rupture propagated towards the east and the more populated regions.

A comparison of the observed and modeled surface displacements shows a reasonable agreement. The discrepancies between the model and the leveling data are between 0 and 6 cm, mostly near the fault itself. These discrepancies may be due to fault complexity and/or benchmarks instability, effects not considered in the model.

The modeling results suggest that a relatively simple model can explain the observed deformation signal as well the hydrological signals caused by the 24 May 2006 earthquake. While a more complex model combined with inversion might yield a better fit to the observed data, I feel that it is unjustified (and poorly constrained) due to the high decorrelation in the DInSAR data and spatial coverage of the leveling and piezometric data.

These results confirm the shallow depth of the earthquake and explain in part why the earthquake was so strongly felt in the area. The area is highly seismic and the details provided by this study provide additional constraints on the nature of faulting in this area which will be useful for future studies on the seismic hazard.

The groundwater level changes analysis leads to believe that poroelastic phenomena area the cause of the observed changes. This analysis and modeling of source fault allow to obtain the value of static volumetric strain efficiency in wells locations and depths which are within ±1 standard deviation from its best fit value, except for PZ-7 and G-1-17 where groundwater level record are probably influenced by other processes. The obtained values of static volumetric strain efficiency could be used in future studies of groundwater level changes due to crustal deformation in the study area caused by both seismic events and aseismic creep and anthropogenic activity.

The postseismic pattern of the groundwater level in four analyzed piezometric wells suggests the gradual diffusion of pore pressure. The characteristic decay is lower for the well located closer to coseismic rupture (see Figure 40 and Table XIII). Assuming the coseismic fault plane as the source of pore pressure changes and using the characteristic decay time obtained by the theoretical postseismic fluid-flow modeling, the hydraulic diffusivity was estimated. The range of estimated values is in good agreement with values obtained by the other works for the same area (Glowacka and Nava, 1996; Glowacka *et al.*, 2010). These results suggest the coseismic changes of the fault plane zone structure could be the source of pore pressure changes.

In the PZ-3 well, a sudden coseismic groundwater level drop followed by the rapid gradual recovery and even an increase of groundwater level is observed. This well is located ~1 km to the North from the EH borehole tiltmeter, close to the eastern surface rupture end, and in area where four aftershocks of Mw≥4 occurred. The groundwater level records from the PZ-3 piezometric well were compared with the north-component tilt records from the EH borehole tiltmeter. A high degree of similitude between the records was observed at all times, i.e., in pre-, co- and postseismic parts (Figure 41). The preliminary analysis of observed phenomena suggests that this case can be described by the dilatancy-diffusion theory.

The dilatancy-diffusion theory was developed in the 1970's by Nur (1972); Scholz *et al.* (1973); Whitcomb *et al.* (1973). Dilatancy is a term for the increase in the volume of a rock during deformation. Dilatancy can occur due to an increase in pore volume, a change in the crack and pore distribution or microfracturing. Dilatancy is important in earthquake prediction because it explains changes in the ratio of P wave to S wave velocity, ground tilting and groundwater level changes. The dilatancy-diffusion theory states that an external or internal elastic strain causes rocks to dilate (stage I and II in Scholz *et al.* (1973)) and decrease the pore pressure. In the next stage (stage III in Scholz *et al.* (1973)) the reestablishing of pore pressure occurs by fluid diffusion. Microcracks form and increase in number, allowing more water to saturate the rock and forming even more microcracks. This lowers the rock strength and eventually leads to failure: rupture occurs (stage IV in Scholz *et al.*, 1973). Following the earthquake the dilatancy recovers, at time constant determined by the hydraulic diffusivity of the system (stage V in Scholz *et al.* (1973)).

Two cycles can be identified in the tiltmeter and piezometers records: I-V and Ia-Va (Figure 41). The first cycle starts before the mainshock occurrence and manifests itself by means of an increase in the groundwater level, caused probably by water influx, and tilt increase in the fault rupture direction (stage I-III). The earthquake produces the groundwater drop and tilt decrease (stage IV). The mainshock makes the rocks dilate in the region of the instruments location, which give rise to a rapid gradual recovery (stage V) and an increase of groundwater level and ground tilt regarding the pre-earthquake levels (stage Ia-IIIa) followed by aftershocks activity (stage IVa). The observed phenomena seem to be important for earthquake prediction and more detailed analysis of all instruments data is needed.

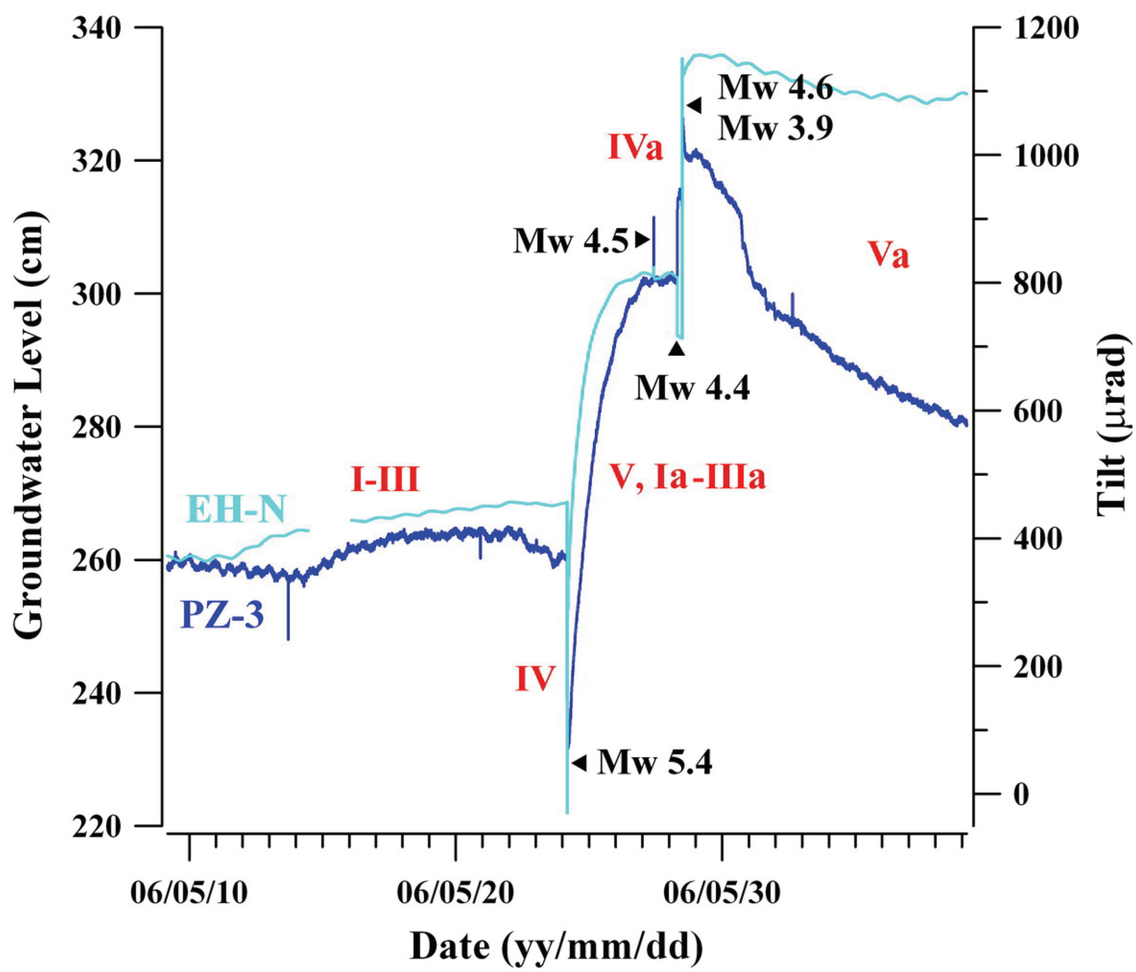

Figure 41: Comparison of ground and groundwater level records from borehole tiltmeter EH and piezometers PZ-3. Roman number indicates the corresponding stage of dilatancy-diffusion theory (as in Shtolz et al. (1973)). "a" denotes the second cycle.

Figura 41: Comparación de registros de nivel de superficie y agua subterránea del inclinómetro de pozo EH y piezómetro PZ-3. Numero romano indica la etapa correspondiente de la teoría de dilatación-difusión (como en *Sholz et al. (1973)).* "a" denota el segundo ciclo.

Chapter VI

SUMMARY CONCLUSIONS AND FUTURE STUDIES RECOMMENDATION

Satellite observations (DInSAR method), ground-based geological, geodetic, and geotechnical measurements were analyzed in this thesis in order to improve the understanding of temporal and spatial distributions of surface deformation in the Mexicali Valley. This work focused on examining the anthropogenic surface deformation related to extraction of geothermal fluids in the CPGF and deformation caused by the moderate magnitude (Mw=5.4) Morelia Fault Earthquake that occurred in the Mexicali Valley on May 24, 2006.

For the detection and analysis of anthropogenic ground deformation 22 Envisat ASAR images from descending and ascending tracks, spanning October 2003 and February 2006 were used. The analysis of DInSAR data showed that, despite several limitations associated with the application of this method, as geometric and temporal decorrelation and atmospheric noise, the C-Band radar data provided a detailed mapping of both the amplitude and spatial extent of anthropogenic ground deformation in the Mexicali Valley. The limitation of temporal and perpendicular baselines of analyzed interferometric pairs reduced the number of data, however considerably improved its reliability (quality). Atmospheric noise was reduced using stacking method of successive single short temporal baseline (maximum three months) interferograms. The stacking results span December 2004 to December 2005 period. DInSAR data (single interferograms and stacking map) revealed the strong ground deformation signal in the study area. Comparison of data from ascending and descending tracks, and data from ground-based measurements allowed to attribute the major part of observed ground deformation to subsidence. The observed by

DInSAR ground subsidence show a northeast-southwest aligned elliptical pattern, largely coincident with the shape of the Cerro Prieto pull-apart basin, as it was noticed by Glowacka *et al.* (1999, 2005). The highest deformation rate area has two subsidence basins. The first centre of subsidence is located in the CPGF production zone, and the second is located in the area between the eastern limits of the CPGF and the Saltillo fault, which was proposed as recharge zone in the previous studies (Glowacka *et al*., 1999; Sarychikhina, 2003). DInSAR stacking data reports that the maximum LOS deformation occurs in the recharge zone at a rate of ~16±1.5 cm/yr, and the maximum LOS deformation rate in the CPGF production zone is ~10±1.5 cm/yr. The integration of the observed by DInSAR subsidence pattern with mapped geological data allowed to identify the tectonic faults which control the spatial extent of the observed subsidence. DInSAR stacking data are well explained by model which consists of seven rectangular tensional fractures: four corresponding to two geothermal reservoirs and three representing two recharge aquifers. The comparison of DInSAR stacking data with 1994-1997 and 1997-2006 leveling surveys reveals the increase of subsidence rate in the recharge zone and migration to the northeast of maximum deformation in the CPGF production zone, both related to the changes in the geothermal fluid extraction. These results suggest that the land subsidence in the study area is a dynamical process.

For the study of coseismic deformation caused by moderate size (Mw=5.4) Morelia Fault Earthquake 11 Envisat ASAR images, from descending and ascending tracks, spanning December 2005 and December 2006, were used. Despite the decorrelation, a clear deformation signal roughly parallel to the known surface fault and consistent with normal faulting was observed in the wrapped phase image. Besides satellite coseismic observations, clear deformation signals caused by the May 24, 2006 earthquake were detected by leveling surveys, field observations and geotechnical instruments (crackmeters, tiltmeters and piezometers). Source parameters for the earthquake were estimated using forward modeling of both surface deformation data (DInSAR, leveling survey and FM vertical crackmeter data) and static volume strain changes inferred from co-seismic changes in groundwater level. The modeling results confirm the shallow depth of the earthquake and explain in part why the earthquake was so strongly felt in the area. The value of static volumetric strain efficiency was obtained and could be used in future studies of groundwater level changes due to crustal deformation in the study area. Based on results of the theoretical postseismic fluid-flow modeling the hydraulic diffusivity was estimated. The range of estimated values is in good agreement with values obtained in the other studies for the same area (Glowacka and Nava, 1996; Glowacka *et al.*, 2009) and is within diffusivity range for seismogenic faults specified by Talwani and Acree (1984/1985).

During this thesis elaboration several problems were found. Due to the lack of time and/or other circumstances these problems were not properly resolved and I suggest that they need be taken into account for the future studies. These problems are:

1. Range change signal to the south of evaporation pound and west of the Cerro Prieto fault was observed in several interferograms. Despite the same location, the sign of this signal change. The same signal of range change was previously reported by Carnec and Fabriol (1999) and was attributed to the injection activity in the CPGF. However Hannsen (2001) suggested that this signal is due to atmospheric distortion. Analysis of more differential interferograms is critical to determine the origin of this signal. The use of advanced DInSAR methods (as Permanents Scatters (Ferretti *et al.*, 2001), e.g.) can improve the accuracy of analysis and can also eliminate the atmospheric artifacts.
2. The observed subsidence pattern as the best-fit model suggest the existence of some linear, parallel to the principal faults, buried structures within and below the aquifer-bearing sedimentary basin fill between the eastern edge of CPGF and recharge zone (Figure 29). The more detailed study in this zone (probably geophysical survey will be more appropriate) will be very useful to determine the nature and origin of this limiting/separating structure.
3. In this thesis an attempt to analyze the correlation between the geothermal production changes and seismicity pattern changes was performed. However the high thereshold magnitude of used catalog did not allow to include the majority of seismicity triggered by geothermal production. The high error of epicenters localization was also a limiting factor of this analysis. This microseismic monitoring with precise epicenter localization is necessary to provide some information about correlation of changes in patterns of

seismicity and changes in the geothermal production. Such information might be useful for seismic hazard assessment and studies of reservoirs dynamics.

4. The anthropogenic subsidence in the study area causes the aseismic mainly vertical slip (creep) of the tectonic faults. In larger scale this process is observed along the Saltillo fault where the vertical annual slip rate is around 6 cm/yr. The vertical slip in this fault occurs in two ways: as continuous slip and as slip events with displacements ranfing from 1 to 3 cm. The frequency of slip events is about 3 per year. An attempt to detect the slip events which occurred in 2005 in the interferograms was performed. However it did not give positive results. The resolution of the interferograms (pixel size of $100 \times 100 m^2$) and the noise presented in the interferograms probably caused this. The use of smaller pixels and application of Advanced DInSAR techniques could produce better results.

5. During the analysis of tiltmeter and piezometric coseismic and postseismic data the large similitude of the records was observed in preseismic, coseismic and postseismic parts for two instruments (PZ-3 and EH) located very close to coseismic rupture. The preliminary analysis of observed phenomena can suggest that this case can be described by the dilatancy-diffusion theory. However, the detailed analysis of more pre-, co-, and postseismic signal data from more instruments and statistic analysis are needed to obtain more credible conclusion.

Reference

Agnew, D. C. 1986. Strainmeters and tiltmeters. *Rev. Geophys.* 24: 579-624.

Albores, A., A. Reyes, J. N. Brune, J. Gonzalez, L. Garcilazo, and F. Suarez. 1980. Seismicity studies in the region of the Cerro Prieto geothermal field. *Geothermics* 9: 65-77.

Alipour, S., M. Motgah, M. A. Sharifi, and T. R. Walter. 2008. InSAR time series investigation of land subsidence due to groundwater overexploitation in Tehran, Iran. *In: Proc. USEReST 2008*, 1-5.

Allen, R. V. 1978. Tiltmeter observations near a large earthquake. *Bull. Seismol. Soc. Am.* 68 (3): 855-857.

Allis, R. G., X. Zhan, and A. Clotworthy. 1998. Predicting Future Subsidence at Wairakei Field, New Zealand. *Geotherm. Res. Counc. Trans.* 22: 43 – 47.

Amelung, F., S. Jonson, H. A. Zebker, and P. Segall. 2000. Widespread uplift and 'trapdoor' faulting on Galapagos volcanoes observed with radar interferometry. *Nature* 407: 993-996.

Aydin, A., and A. Nur. 1982. Evolution of pull-apart basin and their scale independence. *Tectonics* 1: 91-105.

Bamler, R. 2000. Principles of Synthetic Aperture Radar. *Surv. Geophys.* 21: 147-157.

Bamler, R., and P. Hartl. 1998. Synthetic aperture radar interferometry. *Inverse Prob.* 14: R1-R54.

Belabbes, S. 2008. Caractérisation de la déformation active par l'Interférométrie Radar (InSAR): Failles sismiques aveugles et cachées de l'Atlas Tellien (Algérie) et du Rif (Maroc) le long de la limite des plaques Afrique-Eurasie. Ph.D. Thesis, l'Université de Strasbourg, Strasbourg, France, 201 pp.

Bennett, R. A., W. Rodi, and R. E. Reilinger. 1996. Global Positioning System constraints on fault slip rates in southern California and northern Baja, Mexico. *J. Geophys. Res.* 101 (B10): 21943-21960.

Biot, M. A. 1941. General theory of three-dimensional consolidation. *J. Appl. Phys.* 12 (2): 155-164.

Bürgmann, R., P. A. Rosen, and E. J. Fielding. 2000. Synthetic aperture radar interferometry to measure Earth's surface topography and its deformation. *Annu. Rev. Earth Env.* 28 (1): 169-209.

Cabral-Cano, E., T. H. Dixon, F. Miralles-Wilhelm, O. Diaz-Molina, O. Sanchez-Zamora, and R. E. Carande. 2008. Space geodetic imaging of rapid ground subsidence in Mexico City. *Geol. Soc. Am. Bull.* 120 (11-12): 1556.

Camacho Ibarra, E. 2006. Análisis de la deformación vertical del terreno en la región de confluencia del sistema de fallas Cerro Prieto - Imperial en el periodo 1962-2001. M.Sc. Thesis, Department of Geophysics Centro de Investigación Científica y Educación Superior de Ensenada, Ensenada, B.C., Mexico, 135 pp.

Carnec, C., and C. Delacourt. 2000. Three years of mining subsidence monitored by SAR interferometry, near Gardanne, France. *J. Appl. Geophys.* 43 (1): 43-54.

Carnec, C., and H. Fabriol. 1999. Monitoring and modeling land subsidence at the Cerro Prieto geothermal field, Baja California, Mexico, using SAR interferometry. *Geophys. Res. Lett.* 26 (9): 1211-1214.

Carnec, C., D. Massonnet, and C. King. 1996. Two examples of the application of SAR interferometry to sites of small extent. *Geophys. Res. Lett.* 23 (24): 3579-3582.

CFE. 1995. Cerro Prieto Geothermal Field. CFE, Residencia General de Cerro Prieto, 28 pp.

CFE. 2006. Cerro Prieto Geothermal Field. CFE, Residencia General de Cerro Prieto, 36 pp.

Chen, C. W., and H. A. Zebker. 2000. Network approaches to two-dimensional phase unwrapping: intractability and two new algorithms. *J. Opt. Soc. Am.* 17 (3): 401-414.

Chen, C. W., and H. A. Zebker. 2001. Two-dimensional phase unwrapping with use of statistical models for cost functions in nonlinear optimization. *J. Opt. Soc. Am.* 18 (2): 338-351.

Crank, J., 1975. The mathematics of diffusion. Clarendon Press., Oxford, UK, 414 pp.

Curlander, J. C., and R. N. McDonough, 1991. Synthetic Aperture Radar: Systems and Signal Processing. John Wiley and Sons, Inc., New York, USA, 647 pp.

Darby, D., J. González, and P. Lesage. 1984. Geodetic studies in Baja California, Mexico, and the evaluation of short-range data from 1974 to 1982. *J. Geophys. Res.* 89 (B4): 2478-2490.

Darby, D., E. Nyland, F. Suárez-Vidal, D. Chavez, and J. González. 1981. Strain and displacement measurements for the June 9, 1980 Victoria , Mexico, Earthquake. *Geophys. Res. Lett.* 8. (6): 549-551.

Davis, P. M. 1986. Surface deformation due to inflation of an arbitrary oriented triaxial ellipsoidal cavity in an elastic half-space, with references to Kilauea Volcano, Hawaii. *J. Geophys. Res.* 91 (B7): 7429-7438.

de la Peña, L., A. 1981. Results from the first order leveling surveys carried out i n the Mexicali Valley and at the Cerro Prieto field, Baja California. *In: Proc. of the Third Symposium on the Cerro Prieto Geothermal Field, Baja California, Mexico*, Lawrence Berkeley Laboratory, Berkeley, California, 281-291.

de la Peña, L. A., and C. I. Puente. 1979. The geothermal field of Cerro Prieto. In: W. A. Elders (ed.). Geology and Geothermics of the Salton Trough. Campus Museum Contribution, University of California, Riverside, CA, USA, 20-35.

Dixon, T. H., F. Amelung, A. Ferretti, F. Novali, F. Rocca, R. Dokka, G. Sella, S. W. Kim, S. Wdowinski, and D. Whitman. 2006. Space geodesy: Subsidence and flooding in New Orleans. *Nature* 441: 587-588.

Dominguez, T., C. J. Rebollar, and H. Fabriol. 1997. Attenuation of coda waves at the Cerro Prieto geothermal field, Baja California, Mexico. *Bull. Seismol. Soc. Am.* 87 (5): 1368-1374

Dzurisin, D., M. P. Poland, and R. Burgmann. 2002. Steady subsidence of Medicine Lake volcano, northern California, revealed by repeated leveling surveys. *J. Geophys. Res.* 107 (B12): 2372.

Dzurisin, D., C. Wicks, and W. Thatcher. 1999. Renewed uplift at the Yellowstone caldera measured by leveling surveys and satellite radar interferometry. *Bull. Volcanol.* 61 (6): 349-355.

Elachi, C., 1988. Spaceborne radar remote sensing, aplications and techniques. IEEE Press, NY, USA, 254 pp.

Elders, W. A., D. K. Bird, A. E. Williams, and P. Schiffman. 1984. Hydrothermal-flow regime and magmatic heat source of the Cerro Prieto geothermal system, Baja California, Mexico. *Geothermics* 13: 27-47.

Fabriol, H., and L. Munguía. 1997. Seismic activity at the Cerro Prieto geothermal area (Mexico) from August 1994 to December 1995, and its relationship with tectonics and fluid exploitation. *Geophys. Res. Lett.* 24 (14): 1807-1810.

Feng, Q. Y., G. J. Liu, L. Meng, E. J. Fu, H. R. Zhang, and K. F. Zhang. 2008. Land subsidence induced by groundwater extraction and building damage level assessment—a case study of Datun, China. *J. China Univ. Min. Technol.* 18 (4): 556-560.

Ferretti, A., C. Prati, and F. Rocca. 2001. Permanent Scatters in SAR Interferometry. *IEEE Trans. Geosci. Remote Sens.* 39: 8–20.

Ferronato, M., G. Gambolati, C. Janna, and P. Teatini. 2007. Numerical modelling of regional faults in land subsidence prediction above gas/oil reservoirs. *International Journal for Numerical and Analytical Methods in Geomechanics* 32: 633-657.

Fialko, Y., and M. Simons. 2000. Deformation and seismicity in the Coso geothermal area, Inyo County, California: Observations and modeling using satellite radar interferometry. *J. Geophys. Res.* 105 (B9): 21,781-21,794.

Fialko, Y., M. Simons, and D. Agnew. 2001. The complete (3-D) surface displacement field in the epicentral area of the 1999 Mw 7.1 Hector Mine Earthquake, California, from space geodetic observations. *Geophys. Res. Lett.* 28: 3063–3066.

Fielding, E. J., M. Talebian, P. A. Rosen, H. Nazari, J. A. Jackson, M. Ghorashi, and R. Walker. 2005. Surface ruptures and building damage of the 2003 Bam, Iran, earthquake mapped by satellite synthetic aperture radar interferometric correlation. *J. Geophys. Res.* 110 (B3): BO3302.

Frez, J., and J. J. González. 1991. Crustal structure and seismotectonics of northern Baja California. In: J. P. Dauphin and B. R. T. Simoneit (eds.). The Gulf and Peninsular Province of the Californias. American Association of Petroleum Geologists, 261–283.

Fruneau, B., J. Achache, and C. Delacourt. 1996. Observation and modeling of the Saint-Etienne-de-Tinee landslide using SAR interferometry. *Tectonophysics* 265 (3-4): 181-190.

Fuis, S. G., W. D. Mooney, J. H. Healey, G. A. McMechan, and W. J. Lutter. 1982. Crustal structure of the Imperial Valley region. The Imperial Valley, California, Earthquake of October 15, 1979. US Geological Survey Professional Paper 1254, Washington, D.C., 25-49.

Gabriel, A. G., R. M. Goldstein, and H. A. Zebker. 1989. Mapping small elevation changes over large areas: Differential radar interferometry. *J. Geophys. Res.* 94: 9183-9191.

García, J. R. 1978. Estudios de nivelación de primer orden en Cerro Prieto. *In: Proc. of the First Symposium on the Cerro Prieto Geothermal Field*, Baja California, México, 148-150.

Gardner, G. H. F., L. W. Gardner, and A. R. Gregory. 1974. Formation velocity and density-the diagnostic basics for stratigraphic traps. *Geophysics.* 39 (6): 770-780.

Gens, R., and J. L. Van Genderen. 1996. SAR interferometry: Issues, techniques, applications. *Int. J. Remote Sens.* 17 (10): 1803-1836.

Glowacka, E. 1996. Vertical Creepment in the Southern Part of Imperial Fault (Mexico). *In: Proc. of AGU Fall Meeting*, San Francisco, CA, USA.

Glowacka, E., H. Fabriol, L. Munguía, and J. J. Gonzalez. 1997. Seismicity and surface deformation around the Cerro Prieto Geothermal Field. *In: Proc. of Rockbursts and Seismicity in mine*, Balkema, Rotterdam, Poland, 397 – 401.

Glowacka, E., J. González, and H. Fabriol. 1999. Recent vertical deformation in Mexicali Valley and its relationship with tectonics, seismicity, and the exploitation of the Cerro Prieto geothermal field, Mexico. *Pure Appl. Geophys.* 156 (4): 591-614.

Glowacka, E., and F. A. Nava. 1996. Major earthquake in Mexicali valley, Mexico, and Fluid Extraction at Cerro Prieto Geothermal Field. *Bull. Seismol. Soc. Am.* 86: 93-105

Glowacka, E., O. Sarychikhina, and F. A. Nava. 2005. Subsidence and stress change in the Cerro Prieto geothermal field, B.C., México. *Pure Appl. Geophys.* 162: 2095-2110.

Glowacka, E., O. Sarychikhina, F. Suárez-Vidal, F. A. Nava, F. Farfan, G. D. Cossio Battani, and M. Guzmán. 2007. Aseismic slip observed on the faults in Mexicali Valley, Baja California, Mexico. *In: Proc. of AGU, Spring Meeting.*

Glowacka, E., O. Sarychikhina, F. Suárez, R. Mendoza, and F. A. Nava. 2006. Estudio geológico para definir la zona de hundimiento con el fin de relocalización del canal Nuevo Delta en el Valle de Mexicali. Reporte Técnico. CICESE. México, 505 pp.

Glowacka, E., O. Sarychikhina, R. Vázquez González, F. A. Nava, L. Munguía, F. Farfan, G. Diaz De Cossio, and M. A. Garcia Arthur. 2008. Slow aseismic slip in the pull-apart center of Cerro Prieto (Baja California, Mexico), from geotechnical instruments and InSAR observations. *In: Proc. of SSA 2008 Annual Meeting, Seismological Society of America*, Santa Fe, New Mexico, USA, 79, 282.

Glowacka, E., O. Sarychikhina, F. Suárez, F. A. Nava, and R. Mellors. 2010. Anthropogenic subsidence in the Mexicali Valley, Baja California, Mexico, and slip on the Saltillo fault. *Environ. Earth Sci.* 59 (7): 1515-1524.

Gobierno Federal. 1985. Normas técnicas para levantamientos geodésicos. Diario Oficial de la Federación. Secretaría de Programación y Presupuesto. Distrito Federal, México, 13-43.

Gobierno Federal. 1998. Reformas y adiciones a las normas técnicas para levantamientos geodésico. Diario Oficial de la Federación. INEGI. Distrito Federal, México.

Goldstein, R. 1995. Atmospheric limitations to repeat-track radar interferometry. *Geophys. Res. Lett.* 22: 2517–2520.

Goldstein, R. M., H. Engelhardt, B. Kamb, and R. M. Frolich. 1993. Satellite radar interferometry for monitoring ice-sheet motion: Application to an Antarctic ice stream. *Science* 262: 1525-1530.

Goldstein, R. M., and C. L. Werner. 1998. Radar interferogram filtering for geophysical applications. *Geophys. Res. Lett.* 25 (21): 4035-4038.

González, J., J. Frez, and V. Wong. 1983. Mapeo de Vp/Vs en la zona sísmica del Valle de Mexicali. *In: Proc. of Memorias VI Congreso Nacional de Ingeniería Sísmica*, D.F., Mexico, 133-149.

González, J., E. Glowacka, F. Suárez, J. G. Quiñones, M. Guzmán, J. M. Castro, F. Rivera, and M. G. Félix. 1998. Movimiento reciente de la Falla Imperial, Mexicali, B. C. *Ciencia para todos Divulgare, Universidad Autónoma de Baja California* 6 (22): 4-15.

González, M. 1999. Actualización del modelo del basamento en el campo geotérmico de Cerro Prieto, BC, México. *Geotermia* 15 (1): 19–23.

Gonzalez, M., L. Munguia, A. Vidal, V. Wong, and F. Suarez. 2001. Two Mw 4.8 Cerro Prieto, Baja California, Mexico, Earthquakes on 1 June and 10 September 1999: Strong-Motion Observations. *Bull. Seismol. Soc. Am.* 91 (6): 1456-1470.

Grannell, R. B., D. W. Tarnman, R. C. Clover, R. M. Leggewie, P. S. Aronstam, R. C. Kroll, and J. Eppink. 1979. Precision gravity studies at Cerro Prieto - the second year. *In: Proc. of the Second Symposium on the Cerro Prieto Geothermal Field, Baja California, Mexico*, Lawrence Berkeley Laboratory, Berkeley, California, 329-331.

Grecksch, G., F. Roth, and H. J. Kumpel. 1999. Coseismic well-level changes due to the 1992 Roermond earthquake compared to static deformation of half-space solutions. *Geophys. J. Int.* 138 (2): 470-478.

Hadj Sahraoui, O., B. Hassaine, and C. Serief. 2006. Radar Interferometry with Sarscape Software. *In: Proc. of XXIII FIG Congress, Shaping the Change*, Munich, Germany.

Halfman, S. E., M. J. Lippmann, R. Zelwer, and J. H. Howard. 1984. Geologic interpretation of geothermal fluid movement in Cerro Prieto field, Baja California, México. *Am. Assoc. Petrol Geol. Bull.* 68: 18–30.

Hanssen, R. F. 1998. Atmospheric heterogeneities in ERS tandem SAR interferometry. DEOS Report No.98.1. Delft, Delft University press. Netherlands, 136 pp.

Hanssen, R. F. 2001. Radar Interferometry: Data Interpretation and Error Analysis. Kluwer Academic Publishers, Dordrecht, The Netherlands, 328 pp.

Henderson, F. M., and A. J. Lewis (eds.). 1998. Principles and applications of imaging radar. Manual of remote sensing. Third edition, volume 2. John Wiley and Sons, Inc., New York, USA, 896 pp.

Herzig, C. T., and D. C. Jacobs. 1994. Cenozoic volcanism and two-stage extension in the Salton trough, southern California and northern Baja California. *Geology* 22 (11): 991-994.

Hole, J. K., C. J. Bromley, N. F. Stevens, and G. Wadge. 2007. Subsidence in the geothermal fields of the Taupo Volcanic Zone, New Zealand from 1996 to 2005 measured by InSAR. *J. Volcanol. Geotherm. Res.* 166 (3-4): 125-146.

Hung, W.-C., C. Hwang, C.-P. Chang, J.-Y. Yen, C.-H. Liu, and W.-H. Yang. 2010. Monitoring severe aquifer-system compaction and land subsidence in Taiwan using multiple sensors: Yunlin, the southern Choushui River Alluvial Fan. *Environ. Earth Sci.* 59 (7): 1866-6280.

Kampes, B. 2005. Delft Object-oriented Radar Interferometric Software User's manual and technical documentation. The Netherlands: Delft University of Technology.

Kampes, B., R. Hanssen, and Z. Perski. 2003. Radar interferometry with public domain tools. *In: Proc. of FRINGE 2003*, Frascati, Italy.

Kampes, B., and S. Usai. 1999. Doris: The Delft object-oriented radar interferometric software. *In: Proc. of the Second International Symposium on Operationalization of Remote Sensing*, Enschede, Netherlands.

Kenyi, L. W., and V. Kaufmann. 2001. Estimation of alpine permafrost surface deformation using InSAR data. *In: Proc. of IEEE International Geoscience and Remote Sensing Symposium*, Sydney, Australia, 3, 1107 – 1109.

King, C. Y., S. Azuma, G. Igarashi, M. Ohno, H. Saito, and H. Wakita. 1999. Earthquake-related water-level changes at 16 closely clustered wells in Tono, central Japan. *J. Geophys. Res.* 104 (B6): 13,073-13,082.

Kitagawa, Y., N. Koizumi, and T. Tsukuda. 1996. Comparison of postseismic groundwater temperature changes with earthquake-induced volumetric strain release: Yudani hot spring, Japan. *Geophys. Res. Lett.* 23 (22): 3147–3150.

Koizumi, N., Y. Kano, Y. Kitagawa, T. Sato, M. Takahashi, S. Nishimura, and R. Nishida. 1996. Groundwater anomalies associated with the 1995 Hyogo-ken Nanbu earthquake. *J. Phys. Earth* 44 (4): 373-380.

Kümpel, H. J. 1991. Poroelasticity: parameters reviewed. *Geophys. J. Int.* 105: 783–799.

Kwok, R., and M. A. Fahnestock. 1996. Ice sheet motion and topography from radar interferometry. *IEEE Trans. Geosci. Remote Sens.* 34 (1): 189-200.

Lippmann, M. J., and G. S. Bodvarsson. 1983. Numerical studies of the heat and mass transport in the Cerro Prieto geothermal field, Mexico. *Water Resour. Res.* 19 (3): 753-767.

Lippmann, M. J., N. E. Goldstein, S. E. Halfman, and P. A. Witherspoon. 1984. Exploration and development of the Cerro Prieto geothermal field. *J. Pet. Technol.* 36 (9): 1579-1591.

Lippmann, M. J., A. H. Truesdell, A. M. Mañón, and S. E. Halfman. 1991. A review of the hydrogeologic-geochemical model for Cerro Prieto. *Geothermics* 20: 39-52.

Lira, H. 1996. Resultados del monitoreo de desplazamiento de la falla Cerro Prieto en 1996. Informe técnico RE 21/96. Comisión Federal de Electricidad, Residencia de Estudios. México.

Lira, H. 1998. Resultados del monitoreo de desplazamiento de la falla Cerro Prieto en 1998 Informe Técnico RE05/99. Comisión Federal de Electricidad, Residencia de Estudios. México.

Lira, H. 1999. Monitoreo de la Subsidencia en el Campo Geotérmico de Cerro Prieto, B.C., México. *Geotermia, Revista Mexicana de Geoenergia* 15 (1): 31-38.

Lira, H. 2005. Actualización del modelo geológico conceptual del yacimiento Geotérmico de Cerro Prieto. *Geotermia, Revista Mexicana de Geoenergia* 18 (1): 37-46.

Lira, H. 2006. Características del sismo del 23 de Mayo de 2006. Informe RE-023/2006. Comisión Federal de Electricidad, Residencia de Estudios. México.

Lira, H., and J. F. Arellano. 1997. Resultados de la nivelación de precisión realizada en 1997, en el campo geotérmico Cerro Prieto. Informe técnico RE 07/97. Comisión Federal de Electricidad, Residencia de Estudios. México, 25 pp.

Majer, E. L., and T. V. McEvilly. 1982. Seismological studies at the Cerro Prieto Field: 1978-1982. *In: Proc. of the Fourth Symposium on the Cerro Prieto Geothermal Field, Baja California, Mexico*, Lawrence Berkeley Laboratory, Berkeley, CA, USA, 145-151.

Majer, E. L., T. V. McEvilly, A. Albores, and C. Diaz. 1980. Seismological Studies at Cerro Prieto. *Geothermics* 9 (1): 79-88.

Martz, P. 2009. Asymmetrical subsidence resulting from material and fluid extraction. BSc Thesis, Faculty of Applied Science, University of British Columbia, Vancouver, Canada, 81 pp.

Massonnet, D., P. Briole, and A. Arnaud. 1995. Deflation of Mount Etna monitored by spaceborne radar interferometry. *Nature* 375: 567–570.

Massonnet, D., and K. L. Feigl. 1998. Radar interferometry and its application to changes in the Earth's surface. *Rev. Geophys.* 36 (4): 441–500.

Massonnet, D., T. Holzer, and H. Vadon. 1997. Land subsidence by the East Mesa Geothermal Field, California, observed using Sar interferometry. *Geophys. Res. Lett.* 22: 1537 – 1540.

Massonnet, D., and T. Rabaute. 1993. Radar interferometry: limits and potential. *IEEE Trans. Geosci. Remote Sens.* 31 (2): 455-464.

McHugh, S., and M. J. S. Johnston. 1977. An analysis of coseismic tilt changes from an array in Central California. *J. Geophys. Res.* 82: 5692-5698.

Mogi, K. 1958. Relations between the eruptions of various volcanoes and the deformation of the ground surface around them. *Bull. Earthquake Res. Inst. Univ. Tokyo* 36: 99 - 134.

Mossop, A., and P. Segall. 1997. Subsidence at The Geysers geothermal field, N. California from a comparison of GPS and leveling surveys. *Geophys. Res. Lett.* 24 (14): 1839–1842.

Muller, J. P., and D. Backes. 2003. Quality assessment of X-and C-SRTM with ERS-tandem DEMs over 4 European CEOS WGCV test sites. *In: Proc. of FRINGE 2003*, Frascati, Italy.

Munguía, L., E. Glowacka, F. Suárez-Vidal, H. Lira-Herrera, and O. Sarychikhina. 2009. Near-Fault Strong Ground Motions Recorded during the Morelia Normal-Fault Earthquakes of May 2006 in Mexicali Valley, BC, Mexico. *Bull. Seismol. Soc. Am.* 99 (3): 1538-1551.

Nava, F. A., and E. Glowacka. 1999. Fault-slip Triggering, Healing, and Viscoelastic Afterworking in Sediments in the Mexicali-Imperial Valley. *Pure Appl. Geophys.* 156 (4): 615-629.

Nicholson, C., and R. L. Wesson. 1992. Triggered earthquakes and deep well activities. *Pure Appl. Geophys.* 139 (3): 561-578.

Nilsen, T. H., and A. G. Sylvester. 1995. Strike-slip basins. In: C. J. Busby and R. V. Ingersoll (eds.). Tectonic and sedimentary basins. Blackwell Scientific, Oxford, UK, 425–457.

Nishimura, T., S. Fujiwara, M. Murakami, H. Suito, M. Tobita, and H. Yarai. 2006. Fault model of the 2005 Fukuoka-ken Seiho-oki earthquake estimated from coseismic deformation observed by GPS and InSAR. *Earth Planets Space* 58: 51–56.

Nur, A. 1972. Dilatancy pore fluids, and premonitory variations of tp/ts travel time. *Bull. Seismol. Soc. Am.* 62: 1217-1222.

Papanikolaou, I. D., M. Foumelis, I. Parcharidis, E. L. Lekkas, and I. G. Fountoulis. 2010. Deformation pattern of the 6 and 7 April 2009, MW=6.3 and MW=5.6 earthquakes in L'Aquila (Central Italy) revealed by ground and space based observations. *Nat. Hazards Earth Syst. Sci.* 10: 73–87.

Potok, A. J. 1991. A Study of the Relationship between Subsidence and Flooding. *In: Proc. of the Fourth International Symposium on Land Subsidence*, Houston, TX, USA, 389-395.

Price, E. J., and D. T. Sandwell. 1998. Small-scale deformations associated with the 1992 Landers, California, earthquake mapped by synthetic aperture radar interferometry phase gradients. *J. Geophys. Res.* 103 (B11): 27,001-27,016.

Quilty, E. G., and E. A. Roeloffs. 1997. Water-level changes in response to the 20 December 1994 earthquake near Parkfield, California. *Bull. Seismol. Soc. Am.* 87 (2): 310-317.

Roeloffs, E. A. 1988. Hydrologic precursors to earthquakes: A review. *Pure Appl. Geophys.* 126 (2): 177-209.

Roeloffs, E. A. 1996. Poroelastic techniques in the study of earthquake-related hydrologic phenomena. *Adv. Geophys.* 37: 135-195.

Roeloffs, E. A. 1998. Persistent water level changes in a well near Parkfield, California, due to local and distant earthquakes. *J. Geophys. Res.* 103: 869-889.

Rosen, P. A., S. Hensley, I. R. Joughin, F. K. Li, S. N. Madsen, E. Rodriguez, and R. M. Goldstein. 2000. Synthetic aperture radar interferometry. *In: Proc. of the IEEE*, 88, 333-382.

Rosen, P. A., S. Hensley, G. Peltzer, and M. Simons. 2004. Updated repeat orbit interferometry package released. *Eos Trans. AGU* 85 (5): 47.

Sarychikhina, O., E. Glowacka, R. Mellors, R. Vazquez, L. Munguia, and M. Guzman. 2009. Surface Displacement and Groundwater Level Changes Associated with the 24 May 2006 Mw 5.4 Morelia Fault Earthquake, Mexicali Valley, Baja California, Mexico. *Bull. Seismol. Soc. Am.* 99 (4): 2180-2189.

Scharroo, R., and P. Visser. 1998. Precise orbit determination and gravity field improvement for the ERS satellites. *J. Geophys. Res.* 103 (C4): 8113-8127.

Scholz, C. H., L. R. Sykes, and Y. P. Aggarwal. 1973. Earthquake prediction: a physical basis. *Science* 181 (4102): 803-810.

Schumann, H. H., L. S. Cripe, and R. L. Laney. 1986. Land subsidence and earth fissures caused by groundwater depletion in southern AZ, USA. *In: Proc. of the Third International Symposium on Land Subsidence*, Venice, Italy, 151, 841-852.

Segall, P. 1989. Earthquakes triggered by fluid extraction. *Geology* 17 (10): 942.

Sheng, Z., and D. C. Helm. 1998. Multiple steps of earth fissuring caused by ground-water withdrawal. In: J. W. Borchers (ed.). Tectonic controls of geomorphic processes in land subsidence area. Land subsidence. Star Publishing Company, 149–154.

Sigmundsson, F., P. Durand, and D. Massonnet. 1999. Opening of an eruptive fissure and seaward displacement at Piton de la Fournaise volcano measured by RADARSAT satellite radar interferometry. *Geophys. Res. Lett.* 26: 533–536.

Sil, S. 2006. Response of Alaskan wells to near and distant large earthquakes. M.Sc. Thesis, University of Alaska, Fairbanks, Alaska, USA, 83 pp.

Spreckels, V., U. Wegmüller, T. Strozzi, J. Musiedlak, and H. C. Wichlacz. 2001. Detection and observation of underground coal mining-induced surface deformation with differential SAR interferometry. *In: Proc. of ISPRS Workshop "High Resolution Mapping from Space 2001"*, Hannover, Germany, 227-234.

Stramondo, S., M. Tesauro, P. Briole, E. Sansosti, S. Salvi, R. Lanari, M. Anzidei, P. Baldi, G. Fornaro, and A. Avallone. 1999. The September 26, 1997 Colfiorito, Italy, earthquakes: modeled coseismic surface displacement from SAR interferometry and GPS. *Geophys. Res. Lett.* 26 (7): 883-886.

Strozzi, T., U. Wegmüller, L. Tosi, G. Bitelli, and V. Spreckels. 2001. Land subsidence monitoring with differential SAR interferometry. *Photogramm. Eng. Remote Sens.* 67 (11): 1261-1270.

Strozzi, T., U. Wegmuller, C. L. Werner, A. Wiesmann, V. Spreckels, G. R. Sensing, and S. Muri. 2003. JERS SAR interferometry for land subsidence monitoring. *IEEE Trans. Geosci. Remote Sens.* 41 (7): 1702-1707.

Suárez-Vidal, F., L. Munguia-Orozco, M. Gonzalez-Escobar, J. Gonzalez-Garcia, and E. Glowacka. 2007. Surface Rupture of the Morelia Fault Near the Cerro Prieto Geothermal Field, Mexicali, Baja California, Mexico, during the Mw 5.4 Earthquake of 24 May 2006. *Seismol. Res. Lett.* 78 (3): 394-399.

Suárez-Vidal, F., R. Mendoza-Borunda, L. Nafarrete-Zamarripa, J. Rámirez, and E. Glowacka. 2008. Shape and dimensions of the Cerro Prieto pull-apart basin, Mexicali, Baja California, México, based on the regional seismic record and surface structures. *Int. Geol. Rev.* 50 (7): 636-649.

Takemoto, S. 1995. Recent results obtained from continuous monitoring of crustal deformation. *J. Phys. Earth* 43: 407-420.

Talwani, P., and C. Acree. 1984/1985. Pore pressure diffusion and the mechanism of reservoir-induced seismicity. *Pure Appl. Geophys.* 122: 947-965.

Truesdell, A., M. Lippman, H. Gutierrez Puente, and J. De Leon-Vivar. 1998. The importance of natural fluid recharge to the sustainability of the Cerro Prieto resource. *Geotherm. Res. Counc. Trans.* 22: 529-536.

Twiss, R. J., and M. E. Moores, 1992. Structural Geology. W. H. Greeman and Company, New York, USA, 532 pp.

Vasco, D. W., C. Wicks, K. Karasaki, and O. Marques. 2002. Geodetic imaging: reservoir monitoring using satellite interferometry. *Geophys. J. Int.* 149 (3): 555-571.

Vázquez González, R. 1999. Condiciones geohidrológicas del acuífero somero en la zona del campo geotérmico de Cerro Prieto. *Geotermia* 15 (1): 11-18.

Vázquez González, R., E. Glowacka, and A. Díaz Fernández. 2005. Monitoreo continuo del nivel piezométrico en la zona geotérmica de Cerro Prieto. *In: Proc. of IV Reunión Nacional de Ciencias de la Tierra*, Juriquilla, Querétaro, Mexico, 33.

Vázquez González, R., J. Ramírez Hernández, A. Martín Barajas, C. Carreón Diazconti, O. R. García Cueto, F. Miranda Reyes, S. Vázquez Hernández, H. S. Benítez Pérez, and S. Espinoza García. 1998. Estudio Geohidrológico del Campo Geotérmico de Cerro Prieto. Contrato CFE-CICESE RGCP-CLS-002/97.

Velasco, J. 1963. Levantamiento Gravimétrico, Zona Geotérmica de Mexicali, Baja California. Reporte Interno. Consejo de Recursos Naturales no Renovables, 55 pp.

Wakita, H. 1975. Water wells as possible indicators of tectonic strain. *Science* 189: 553–555.

Wakita, H., G. Igarashi, and K. Notsu. 1991. An anomalous radon decrease in groundwater prior to an M6. 0 earthquake: A possible precursor? *Geophys. Res. Lett.* 18 (4): 629-632.

Walsh, J. B. 2002. Subsidence above a planar reservoir. *J. Geophys. Res.* 107 (B9): ETG 6-1.

Wang, G. Y., G. You, B. Shi, J. Yu, H. Y. Li, and K. H. Zong. 2009. Earth fissures triggered by groundwater withdrawal and coupled by geological structures in Jiangsu Province, China. *Environ. Geol.* 57: 1047-1054.

Wang, H. F. 1993. Quasi-static poroelastic parameters in rock and their geophysical applications. *Pure Appl. Geophys.* 141 (2): 269-286.

Wang, R., F. L. Mart n, and F. Roth. 2003. Computation of deformation induced by earthquakes in a multi-layered elastic crust—FORTRAN programs EDGRN/EDCMP. *Comput. Geosci.* 29 (2): 195-207.

Wegmüller, U., C. Werner, T. Strozzi, and A. Wiesmann. 2004. Monitoring mining induced surface deformation. *In: Proc. of IEEE International Geoscience and Remote Sensing Symposium*, Anchorage, Alaska, 3, 1933-1935.

Wells, D. L., and K. J. Coppersmith. 1994. New empirical relationships among magnitude, rupture length, rupture width, rupture area, and surface displacement. *Bull. Seismol. Soc. Am.* 84 (4): 974-1002.

Wessel, P., and W. H. F. Smith. 1998. New, improved version of Generic Mapping Tools released. *Eos Trans., AGU* 79 (47): 579.

Whitcomb, J. H., J. D. Garmany, and D. L. Anderson. 1973. Earthquake prediction: variation of seismic velocities before the San Francisco earthquake. *Science* 180: 632-635.

Whittaker, B. N., and D. J. Reddish. 1989. Subsidence: Occurence, Prediction and Control. Elsevier, Amsterdam, Netherlands, 528 pp.

Wicks, C. W., W. Thatcher, F. C. Monastero, and M. A. Hasting. 2001. Steady state deformation of the Coso Range, east central California, inferred from satellite radar interferometry. *J. Geophys. Res.* 106 (B7): 13769-13780.

Wong, V., J. Frez, and F. Suárez. 1997. The Victoria, Mexico, earthquake of June 9, 1980. *Geofísica Internacional* 36: 139-160.

Wyatt, F. K. 1988. Measurements of coseismic deformation in Southern California: 1972-1982. *J. Geophys. Res.* 93: 7923-7942.

Wyman, R. M. 1983. Potential Modeling of Gravity and Leveling Data over Cerro Prieto Geothermal Field. M.Sc. Thesis, Department of Geology, California State University, Long Beach, CA, USA, 79 pp.

Yang, X., and P. M. Davis. 1986. Deformation due to a rectangular tensional crack in an elastic half-space. *Bull. Seismol. Soc. Am.* 76 (3): 865-881.

Yong, R. N., P. Nutalaya, A. M. O. Mohamed, and D. M. Xu. 1991. Land subsidence and flooding in Bangkok. *In: Proc. of the Fourth International Symposium on Land Subsidence*, Houston, TX, USA, 407-416.

Zebker, H., and J. Villasenor. 1992. Decorrelation in interferometric radar echoes. *IEEE Trans. Geosci. Remote Sens.* 30 (5): 950-959.

Zebker, H. A., P. Rosen, and J. Earth. 1997. Atmospheric artifacts in interferometric SAR surface deformation and topographic maps. *J. Geophys. Res.* 102 (B4): 7547–7563.

APPENDIX I

LIST OF THE SAR IMAGES ACQUIRED FOR THIS STUDY

MISSION	SCENE ACQUISITION	ORBIT	TRACK	FRAME	PASS
ENVISAT	2003/10/26	8655	84	2961	D
ENVISAT	2004/05/23	11661	84	2961	D
ENVISAT	2004/09/05	13164	84	2961	D
ENVISAT	2004/10/10	13665	84	2961	D
ENVISAT	2004/12/19	14667	84	2961	D
ENVISAT	2005/01/23	15168	84	2961	D
ENVISAT	2005/02/27	15669	84	2961	D
ENVISAT	2005/04/03	16170	84	2961	D
ENVISAT	2005/05/08	16671	84	2961	D
ENVISAT	2005/06/12	17172	84	2961	D
ENVISAT	2005/07/17	17673	84	2961	D
ENVISAT	2005/08/21	18174	84	2961	D
ENVISAT	2005/09/25	18675	84	2961	D
ENVISAT	2005/10/30	19176	84	2961	D
ENVISAT	2005/12/04	19677	84	2961	D
ENVISAT	2006/02/12	20679	84	2961	D
ENVISAT	2006/03/19	21180	84	2961	D
ENVISAT	2006/10/15	24186	84	2961	D
ENVISAT	2006/11/19	24687	84	2961	D
ENVISAT	2006/12/24	25188	84	2961	D
ENVISAT	2003/12/16	9378	306	639	A
ENVISAT	2004/02/24	10380	306	639	A
ENVISAT	2004/05/04	11382	306	639	A
ENVISAT	2006/04/04	21402	306	639	A
ENVISAT	2006/05/09	21903	306	639	A
ENVISAT	2006/09/26	23907	306	639	A
ENVISAT	2006/10/31	24408	306	639	A
ENVISAT	2006/12/05	24909	306	639	A